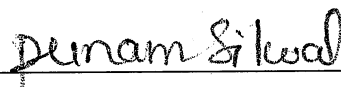


METAL-INSULATOR TRANSITION AND CROSSOVER FROM COHERENT BAND-LIKE  
TRANSPORT TO INCOHERENT TRANSPORT IN FERRIMAGNETIC EPITAXIAL SPINEL  
 $\text{NiCo}_2\text{O}_4$  THIN FILMS

AN ABSTRACT  
SUBMITTED ON THE TWELFTH DAY OF MAY, 2014  
TO THE DEPARTMENT OF PHYSICS  
OF THE GRADUATE SCHOOL OF  
TULANE UNIVERSITY  
IN PARTIAL FULFILLMENT OF THE REQUIREMENTS  
FOR THE DEGREE OF  
DOCTOR OF PHILOSOPHY  
BY

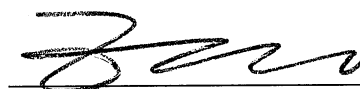


PUNAM SILWAL

APPROVED:



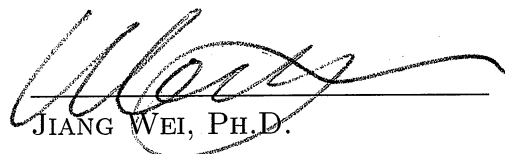
DIYAR TALBAYEV, PH.D.  
CHAIRMAN



ZHIQIANG MAO, PH.D.



LEV KAPLAN, PH.D.



JIANG WEI, PH.D.

METAL-INSULATOR TRANSITION AND CROSSOVER FROM COHERENT BAND-LIKE  
TRANSPORT TO INCOHERENT TRANSPORT IN FERRIMAGNETIC EPITAXIAL SPINEL  
 $\text{NiCo}_2\text{O}_4$  THIN FILMS

A DISSERTATION  
SUBMITTED ON THE TWELFTH DAY OF MAY, 2014  
TO THE DEPARTMENT OF PHYSICS  
OF THE GRADUATE SCHOOL OF  
TULANE UNIVERSITY  
IN PARTIAL FULFILLMENT OF THE REQUIREMENTS  
FOR THE DEGREE OF  
DOCTOR OF PHILOSOPHY  
BY

Punam Silwal.

PUNAM SILWAL

APPROVED: \_\_\_\_\_

Talbayev  
DIYAR TALBAYEV, PH.D.  
CHAIRMAN

Zhiqiang Mao  
ZHIQIANG MAO, PH.D.

Lev Kaplan  
LEV KAPLAN, PH.D.

Jiang Wei  
JIANG WEI, PH.D.

METAL-INSULATOR TRANSITION AND CROSSOVER FROM COHERENT BAND-LIKE  
TRANSPORT TO INCOHERENT TRANSPORT IN FERRIMAGNETIC EPITAXIAL SPINEL  
 $\text{NiCo}_2\text{O}_4$  THIN FILMS

AN ABSTRACT  
SUBMITTED ON THE TWELFTH DAY OF MAY, 2014  
TO THE DEPARTMENT OF PHYSICS  
OF THE GRADUATE SCHOOL OF  
TULANE UNIVERSITY  
IN PARTIAL FULFILLMENT OF THE REQUIREMENTS  
FOR THE DEGREE OF  
DOCTOR OF PHILOSOPHY  
BY

---

PUNAM SILWAL

APPROVED: \_\_\_\_\_

DIYAR TALBAYEV, PH.D.  
CHAIRMAN

---

ZHIQIANG MAO, PH.D.

---

LEV KAPLAN, PH.D.

---

JIANG WEI, PH.D.

# Abstract

$\text{NiCo}_2\text{O}_4$  (NCO) is less studied than the well known isostructural magnetic spinel compounds  $\text{NiFe}_2\text{O}_4$ ,  $\text{CoFe}_2\text{O}_4$ ,  $\text{Fe}_3\text{O}_4$ , or  $\text{Co}_3\text{O}_4$ . This is partly due to the unavailability of  $\text{NiCo}_2\text{O}_4$  single crystals or epitaxial films and the low thermal stability of polycrystalline  $\text{NiCo}_2\text{O}_4$ , which for powder samples is reported to start decomposing at temperatures above  $400^\circ\text{C}$ . Nevertheless, the properties of  $\text{NiCo}_2\text{O}_4$  and their dependence on growth conditions are of considerable interest since  $\text{NiCo}_2\text{O}_4$  is attractive for various technological applications, including fuel cell electrodes, oxygen catalysis, reduction in alkaline media, and water electrolysis. The most common synthesis routes for the spinel rely on sol-gel and thermal decomposition methods that produce polycrystalline particulate samples with a rather low packing density and a low degree of sintering. Hence, the reported electrical properties are severely influenced by crystalline disorders. The major goal of our research is to synthesize the epitaxial  $\text{NiCo}_2\text{O}_4$  thin films and investigate the intrinsic properties.

We have successfully grown epitaxial thin films of spinel  $\text{NiCo}_2\text{O}_4$  on single crystalline  $\text{MgAl}_2\text{O}_4$  (001) substrates by pulsed laser deposition (PLD). X-ray diffraction (XRD) measurement confirmed the epitaxial growth of  $\text{NiCo}_2\text{O}_4$  thin films. For the first time, we have observed metallic conduction with a robust ferrimagnetic order in these epitaxial films. The magnetic structure of  $\text{NiCo}_2\text{O}_4$  has long been known as ferrimagnetic with a Curie temperature  $T_C$   $400^\circ\text{C}$ . The Magnetization measurement revealed hysteresis loops consistent with the reported ferrimagnetic order. The electrical transport exhibits a metallic behavior with the lowest resistivity of  $0.8\text{ m}\Omega\text{ cm}$

and a metal insulator transition around the Neel temperature. The low-temperature grown films (200°C-450°C) are magnetic and metallic while the high temperature grown films (500°C-600°C) are insulating and non-magnetic. The systematic variation in the properties of the films grown at different growth temperatures indicates a close relationship between the magnetic order and electrical transport.

The magnetic properties of  $\text{NiCo}_2\text{O}_4$  have not been used in applications but have been investigated in the context of the mixed valencies of the Ni and Co cations in this inverse spinel. The transport and magnetic properties of thin films depend strongly on their thickness at the ultrathin level. As the thickness becomes smaller, such observables as the resistivity, saturation magnetization, and coercive field can be influenced to a high degree by the films geometrical boundaries, interfacial scattering, and pinning, and the crossover from three-dimensional to two dimensional physics. We investigated the thickness dependent structural, magnetic, and transport properties of  $\text{NiCo}_2\text{O}_4$  films. The structural examination of the films reveals that the epitaxial strain is independent of the film thickness. Electric and magnetic measurements show that the films are metallic with p-type conduction and ferrimagnetic down to 2 unit cells with an enhanced coercive field in the films thinner than 30 unit cells. The low-temperature resistivity data indicate that the observed resistivity minimum results from the disorder-induced quantum interference effects. Our results demonstrate that  $\text{NiCo}_2\text{O}_4$  may provide an alternative magnetic conducting medium for spintronics devices.

We have measured the terahertz-frequency optical conductivity of the  $\text{NiCo}_2\text{O}_4$  films grown at different temperatures. The measurement of real and imaginary parts of the dielectric function (optical conductivity) allowed us to elucidate the details of electronic conduction in  $\text{NiCo}_2\text{O}_4$ . The low-temperature grown film exhibits a metallic behavior with ferrimagnetic ordering, while the high-temperature-grown film

shows greatly suppressed magnetization and insulating behavior. Both films exhibit band-like coherent conduction at intermediate temperatures, albeit with very different carrier densities consistent with the proposed models of cation valencies in this mixed-valence material. Both films also display a crossover to incoherent transport at low temperatures, indicating a disorder-induced tendency toward localization.

METAL-INSULATOR TRANSITION AND CROSSOVER FROM COHERENT BAND-LIKE  
TRANSPORT TO INCOHERENT TRANSPORT IN FERRIMAGNETIC EPITAXIAL SPINEL  
 $\text{NiCo}_2\text{O}_4$  THIN FILMS

A DISSERTATION  
SUBMITTED ON THE TWELFTH DAY OF MAY, 2014  
TO THE DEPARTMENT OF PHYSICS  
OF THE GRADUATE SCHOOL OF  
TULANE UNIVERSITY  
IN PARTIAL FULFILLMENT OF THE REQUIREMENTS  
FOR THE DEGREE OF  
DOCTOR OF PHILOSOPHY  
BY

---

PUNAM SILWAL

APPROVED: \_\_\_\_\_

DIYAR TALBAYEV, PH.D.  
CHAIRMAN

---

ZHIQIANG MAO, PH.D.

---

LEV KAPLAN, PH.D.

---

JIANG WEI, PH.D.

© Copyright by Punam Silwal, 2014

*All Rights Reserved*



# Acknowledgments

I would like to express my sincere gratitude to my advisor, Prof. D. Talbayev for giving me the opportunity to work on this exciting project and for his faith, guidance and support throughout the course of my Ph.D. research. I have been working with Prof. Talbayev from May 2011. I benefited from his guidance in every aspect during my Ph.D study. I deeply appreciate all his invaluable help and support.

The same gratitude goes to Dr. Daeho Kim, who gave me an opportunity to be a part of his research team and advised me for the first four years of my Ph.D. I would like to acknowledge him as my mentor, for providing perspective, guidance and insight. His patience in training me in the operation of the many lab instruments and fielding my unending questions was very much appreciated and for that I acknowledge him.

I would like to thank the members of my Ph.D. committee Prof. Z. Mao, Prof. L. Kaplan, and Prof. J. Wei for taking time out of their busy schedules to evaluate my work. I would like to thank Prof. Z. Mao again for giving me the opportunity to use his lab facilities.

I would like to thank all the Professors in the Department of Physics and Engineering Physics; Prof. James McGuire, Prof. Zhiqiang Mao, Prof. John Perdew, Prof. Lev Kaplan, Prof. Dan Purrington, Prof. Fred Weitfeldt, Prof. George Rosensteel, Prof. Ulrike Diebold, Prof. Douglas Chrisey for their knowledge, inspiration and advice during the class.

I would like to thank Dr. Jibao He for his effort in teaching me the skills

necessary for TEM sample preparation.

I would like to thank Dr. Ludi Miao for teaching, discussing, sharing his ideas and supporting me all the time. I would like to thank all the helping hands from my friends Dr. Ilan Stern, Dr. Xiaolan Zhou, Skylar, Kate, for all the helpful discussion of my experiments, Dr. Jin Hu for helping me with the PPMS measurements and for discussing his ideas. My research has been so exciting because of all the talented and great team members. I want to thank all of my friends in Physics department and in the university.

I would like to thank the members of Department, Teresa Parker, Yu Zhang, Eleanor Berault, and many other administrative staffs for their help and support throughout my PhD study.

I would like to thank all my friends who made my life in the U.S. so colorful.

Finally, I want to thank my husband and family for their love, enthusiasm and support. I wouldn't have gone this far without their belief and support.

Funding for the work discussed in this dissertation was provided through the Louisiana Board of Regents.

# Foreword

This thesis is dedicated to my family.

# Contents

<b>1</b>	<b>Motivation and Objective of Research</b>	<b>2</b>
1.1	History of Research in Spinel $\text{NiCo}_2\text{O}_4$ . . . . .	2
1.2	Motivation . . . . .	4
1.3	Organization of Dissertation . . . . .	6
<b>2</b>	<b>Introduction and Theoretical Background</b>	<b>7</b>
2.1	Spinel Oxide . . . . .	7
2.2	Inverse Spinel $\text{NiCo}_2\text{O}_4$ . . . . .	8
2.3	Magnetism . . . . .	9
2.4	Conduction mechanism in $\text{NiCo}_2\text{O}_4$ . . . . .	13
2.5	Classical Transport . . . . .	13
2.6	Quantum Interference Effect . . . . .	15
2.7	Electron Dephasing Mechanism . . . . .	18
2.7.1	Electron-electron interaction . . . . .	18
2.7.2	Electron-phonon Scattering . . . . .	19
2.7.3	Weak Localization . . . . .	21
2.7.4	Scattering by Magnetic Impurities . . . . .	23
2.8	Optical Conductivity . . . . .	24
<b>3</b>	<b>Thin Film Deposition and Characterization</b>	<b>27</b>
3.1	Pulsed Laser Deposition . . . . .	27

3.1.1	Advantages of Pulsed Laser Deposition . . . . .	29
3.1.2	Drawbacks of Pulsed Laser Deposition . . . . .	29
3.2	Structural Analysis . . . . .	30
3.2.1	$2\theta$ - $\omega$ Scan . . . . .	31
3.2.2	The $\omega$ scan or Rocking Curve . . . . .	31
3.2.3	The $\Phi$ -Scan . . . . .	32
3.2.4	Reciprocal Space Map (RSM) . . . . .	33
3.2.5	X-Ray Reflectivity Scan (XRR) . . . . .	33
3.3	Magnetism Measurement . . . . .	34
3.4	Resistivity Measurement . . . . .	36
3.5	Hall Effect Measurement . . . . .	37
<b>4</b>	<b>Effect of Growth Temperature on the Physical Properties of <math>\text{NiCo}_2\text{O}_4</math></b>	<b>40</b>
4.1	Experimental Methods . . . . .	41
4.2	Structural Results . . . . .	42
4.3	Magnetic Results . . . . .	46
4.4	Transport Properties . . . . .	48
4.5	Discussion . . . . .	49
4.6	Summary and Conclusion . . . . .	51
<b>5</b>	<b>Effect of Thickness on the Physical Properties</b>	<b>52</b>
5.1	Introduction . . . . .	52
5.2	Experimental Methods . . . . .	54
5.3	Structural Properties . . . . .	55
5.4	Transport Properties . . . . .	56
5.5	Observation of QIE . . . . .	57
5.6	Magnetic Properties . . . . .	60

5.7	Conclusion . . . . .	61
<b>6</b>	<b>Terahertz Spectroscopy</b>	<b>63</b>
6.1	Introduction . . . . .	63
6.1.1	General Principle of Terahertz Time-Domain Spectroscopy . .	63
6.1.2	Optical rectification and second harmonic generation . . . . .	64
6.1.3	Electro-Optic Effect or Pockel's Effect . . . . .	68
6.2	THz Generation . . . . .	70
6.2.1	Optical Rectification in ZnTe Crystal . . . . .	70
6.2.2	Tilted Pulse Front . . . . .	72
6.2.3	Photo conductive THz Generation . . . . .	75
6.3	THz Detection . . . . .	77
6.3.1	Electro-optic Sampling . . . . .	77
6.3.2	Photo Conductive receiving antennas . . . . .	79
6.4	Development of Terahertz Time-Domain Spectrometer . . . . .	80
6.4.1	Laser . . . . .	80
6.4.2	THz Optics . . . . .	81
6.4.3	Delay Stage . . . . .	81
<b>7</b>	<b>THz time-domain spectroscopy (THz-TDS) study of NiCo<sub>2</sub>O<sub>4</sub></b>	<b>89</b>
7.1	Introduction . . . . .	89
7.2	Experimental Methods . . . . .	90
7.3	Spectroscopy of low-temperature-grown NiCo <sub>2</sub> O <sub>4</sub> . . . . .	92
7.4	Spectroscopy of high-temperature-grown NiCo <sub>2</sub> O <sub>4</sub> . . . . .	97
7.5	Summary . . . . .	102
	<b>References</b>	<b>103</b>

# List of Figures

2.1	Schematic of the one unit cell of the spinel structure (a) and the interstitial sites of the cations (b) . . . . .	8
2.2	(a) Schematic representation of the energy bands in the Battle model. The A-site Co $t_2$ band and the B-site Ni $e_g$ bands overlap and allow hole transport with a spin flip. (b) Schematic of the B-site energy bands in the Marco model. The Co $t_{2g}$ and the Ni $e_g$ bands overlap to allow hole transport with a spin flip. . . . .	12
2.3	The mechanism of weak localization. A pair of time reversal symmetric loop for electron path is shown in red and black respectively. . . . .	21
2.4	Real and imaginary parts of conductivity of a Drude metal. . . . .	26
3.1	A schematic diagram of Pulsed laser deposition system. . . . .	28
3.2	Schematic representation of X-ray diffraction . . . . .	30
3.3	HR-XRD $2\theta$ - $\omega$ scan of a 240nm thick $\text{NiCo}_2\text{O}_4$ film grown at $350^\circ\text{C}$ on $\text{MgAl}_2\text{O}_4$ (001) substrate. . . . .	31
3.4	(004) rocking curve of the $\text{NiCo}_2\text{O}_4$ film grown at $250^\circ\text{C}$ . . . . .	32
3.5	$\Phi$ scans of the $\text{NiCo}_2\text{O}_4$ (404) and $\text{MgAl}_2\text{O}_4$ (404) reflections . . . . .	33
3.6	(226) RSM scan of the $\text{NiCo}_2\text{O}_4 \parallel \text{MgAl}_2\text{O}_4$ (001) . . . . .	34
3.7	Thickness scan of 24 nm thick $\text{NiCo}_2\text{O}_4$ film . . . . .	35
3.8	The schematic of Josephson junction (a), SQUID (b) . . . . .	35

3.9	The schematics of resistance measurements with (a) two probe and (b) four probe method . . . . .	37
3.10	The mechanism of Hall effect (a), the Hall effect measurement with four terminal configuration (b) . . . . .	38
4.1	HR-XRD $2\theta - \theta$ scan of the films grown at temperature ranging from 200°C-600°C showing the decrease in film peak position increasing the growth temperature. . . . .	42
4.2	HR-XRD $2\theta - \theta$ scan of a 240nm thick $\text{NiCo}_2\text{O}_4$ film grown at 350°C on $\text{MgAl}_2\text{O}_4$ (001) substrate. The inset shows a detailed spectrum around the (004) reflections of the substrate and the film. . . . .	43
4.3	(004) rocking curve of the $\text{NiCo}_2\text{O}_4$ film grown at 350°C. The FWHM is 0.004° which is similar to the FWHM value of $\text{MgAl}_2\text{O}_4$ indicating the high crystalline quality of the $\text{NiCo}_2\text{O}_4$ film. . . . .	44
4.4	$\phi$ scans of the $\text{NiCo}_2\text{O}_4$ (404) and $\text{MgAl}_2\text{O}_4$ (404) reflections, respectively.	45
4.5	HR-XRD RSMs around the (226) reflections of the $\text{NiCo}_2\text{O}_4$ films on $\text{MgAl}_2\text{O}_4$ substrates grown at (a) 250, (b) 350, and (c) 450°C. . . . .	46
4.6	Magnetization $M$ vs. temperature $T$ for the $\text{NiCo}_2\text{O}_4$ films on $\text{MgAl}_2\text{O}_4$ (001) substrates grown at 250, 350, 450, and 550°C. (b) $M$ vs. magnetic field $H$ for the same set of films. . . . .	46
4.7	(a) In-plane resistivity $\rho$ vs. temperature $T$ for the $\text{NiCo}_2\text{O}_4$ films on $\text{MgAl}_2\text{O}_4$ (001) substrates grown at 500, 550, and 600°C, showing insulating behavior. (b) $\rho$ vs. $T$ for the $\text{NiCo}_2\text{O}_4$ films on $\text{MgAl}_2\text{O}_4$ (001) substrates grown at 250, 350, and 450°C, showing metallic behavior. (c) $\rho$ vs. $T$ for the 450 °C film measured under magnetic field of 0 and 1 T exhibiting a negative magnetoresistance of 2% with the application of magnetic field 1 T. . . . .	48



4.8	(a) Magnetization at 2 T vs. growth temperature $T_{\text{sub}}$ , (b) resistivity at the room-temperature $\rho_{300K}$ vs. $T_{\text{sub}}$ , and (c) out of plane lattice constants $c$ vs. $T_{\text{sub}}$ for all the $\text{NiCo}_2\text{O}_4$ films on $\text{MgAl}_2\text{O}_4$ (001) substrates. . . . .	50
5.1	HR-XRD $2\theta$ - $\theta$ scans of $\text{NiCo}_2\text{O}_4$ films on $\text{MgAl}_2\text{O}_4$ (001) substrate with the thicknesses of 11, 30, 77, and 224 unit cells. The film peak position remains at the same value of $2\theta$ , indicating the constant out-of-plane lattice value changing the film's thickness. . . . .	55
5.2	(a), (b), and (c) HR-XRD reciprocal space maps around the (226) reflections of the $\text{NiCo}_2\text{O}_4$ films on $\text{MgAl}_2\text{O}_4$ substrate with the thickness 11, 224, and 875 unit cells, respectively. The horizontal and vertical peak positions for all the films are the same, indicating identical lattice parameters and the strain state independent of the films thickness. . .	56
5.3	In-plane resistivity $\rho$ vs. temperature $T$ for $\text{NiCo}_2\text{O}_4$ with thicknesses of 3, 11, 30, 77, and 224 unit cells. The films maintain their metallic behavior below room temperature from 224 uc to 3 uc, with the lowest room temperature resistivity of $\sim 1.4 \text{ m}\Omega \text{ cm}$ for the 224 uc thick films.	57
5.4	Resistivity $\rho(T)$ for the 224 uc film and the fitted lines for Eqs. (5.1) to (5.3). The inset shows the magnified scale. The best fits of the measured data are achieved with Eq. (5.2) and Eq. (5.3) with $p=3/2$ , indicating the disorder-induced QIE in the 3D limit are responsible for the resistivity minimum in $\text{NiCo}_2\text{O}_4$ . . . . .	58

5.5	(a) Magnetization $m$ vs. temperature $T$ for the $\text{NiCo}_2\text{O}_4$ films with the thicknesses of 3, 11, 30, 77, and 224 unit cells. The inset is the coercive field $H_c$ vs. thickness $t$ . (b) $m$ vs. magnetic field $H$ for the same set of films. (c) Sheet conductance $G$ vs. thickness $t$ . (d) Saturation magnetic moment ( $M_s$ ) at 5 kOe vs. thickness $t$ . The inset shows saturation magnetization $m$ at 5 kOe vs. thickness $t$ (closed circles) and $(mt/(t-t_{dead}))$ vs. thickness $t$ (open triangles). $t_{dead} = 2$ uc is the thickness of the magnetic dead layer. . . . .	61
6.1	Spectrum of electromagnetic radiation. Using time-domain terahertz spectroscopy, we are able to access the terahertz (THz) gap. . . . .	64
6.2	Ordinary refractive index $n_o$ and extra-ordinary refractive index $n_e$ of a birefringent material as a function of $\omega$ . . . . .	68
6.3	A schematic diagram of THz generation in $\text{ZnTe}(110)$ crystal by optical rectification. . . . .	72
6.4	THz emission generated by an optical beam with a tilted wavefront in $\text{LiNbO}_3$ . THz beam (red arrows) is emitted perpendicular to the wavefront (green line). Phase matching condition is satisfied when the velocities of the THz and optical beam (red and blue arrows) and the wavefront form a right-angle triangle, which also determines the tilt angle $\gamma$ . . . . .	74
6.5	The layout of the tilted-wavefront THz emission setup. The diffraction grating tilts the wavefront of the optical excitation pulse. The green lines represent the wavefront tilt at different point along the beam path. The $\frac{\lambda}{2}$ waveplate rotates the polarization of the excitation beam from horizontal to vertical. . . . .	75

6.6	Schematic for the terahertz emitter. The incoming optical pulse excites electrons in the gold strips and creates a vertically polarized terahertz pulse that propagates out the other side of the LT GaAs wafer. The hyper-hemispherical lens helps collimate the terahertz pulse. . . . .	76
6.7	The setup for free-space electro-optic sampling and deconstructed into right- and left-handed components by the beam-splitting polarizer. This difference signal is proportional to the THz electric field. . . . .	79
6.8	The schematic representation of our home-built terahertz time domain spectroscopy (THz TDS) system . . . . .	82
6.9	The measured amplitude of the transmitted terahertz pulse through sample and reference for $\text{NiCo}_2\text{O}_4$ 300°C at 300K. In the time-domain spectra, the first transient is the primary pulse passed directly through the medium. The second transient is due to the reflections of the primary pulse from the back and the front surfaces of the sample. Since the main transmitted pulse is well separated from the first reflected pulse, for the analysis, the data were windowed around the main transmitted pulse. . . . .	84
6.10	The amplitude of the ratio of the sample and reference Fourier transforms of the time-domain data. The inset is the difference between the phases of the sample and reference Fourier transforms. . . . .	85
6.11	Schematic diagram of sample-reference measurement. Here film on substrate represents sample and bare substrate represents reference. .	86
7.1	The real ( $\epsilon_1$ ) and imaginary ( $\epsilon_2$ ) parts of the measured dielectric function of the NCO300 film. Solid lines represent Drude model fits using Eq. (7.3). . . . .	93

7.2	NCO300: (a) The temperature dependence of the DC conductivity $\sigma_0$ .	
	(b) The temperature dependence of the THz spectral weight. . . . .	94
7.3	The real part of the THz optical conductivity of the NCO300 film. The solid lines illustrate the extrapolation to find the DC conductivity $\sigma_0$ . The solid lines at 100-300 K follow the Drude model of Eq. (7.4). . .	95
7.4	The real ( $\epsilon_1$ ) and imaginary ( $\epsilon_2$ ) parts of the measured dielectric function of the NCO500 film. Solid lines represent Drude model fits using Eq. (7.3). . . . .	97
7.5	NCO500: (a) The temperature dependence of the DC conductivity $\sigma_0$ .	
	(b) The temperature dependence of the THz spectral weight. . . . .	99
7.6	The real part of the THz optical conductivity of the NCO500 film. The solid lines illustrate the extrapolation to find the DC conductivity $\sigma_0$ . The solid lines at 250 and 300 K follow the Drude model of Eq. (7.4).	100

# Chapter 1

## Motivation and Objective of Research

### 1.1 History of Research in Spinel $\text{NiCo}_2\text{O}_4$

Spinel oxides are a big group of materials and can be applied for different functionalities: catalysts for decomposition of gases[1, 2], magneto-optical storage media[3], flux guides and sensors in thin film recording heads[4], ferromagnetic semiconductors[5], magnetic fluids[6], multiferroic composites[7, 8], transformer cores and microwave magnetic devices.[9] More recently magnetic spinel ferrites  $\text{NiFe}_2\text{O}_4$  and  $\text{CoFe}_2\text{O}_4$  have been investigated for spin filtering applications in spintronics.[10, 11, 12, 13] The inverse spinel  $\text{NiCo}_2\text{O}_4$  is extensively used and studied as electrode material for oxygen reduction[14, 2], and as a conducting oxide with infrared transparency[15, 16, 17] for sensors and flat panel displays. The magnetic structure of  $\text{NiCo}_2\text{O}_4$  has long been known[18, 19] as ferrimagnetic with a Curie temperature  $T_C$  400°C. Several methods have been reported for the synthesis of spinel, such as sol-gel[20, 21, 22, 23], electro spinning[24], anodic oxidation of alloys[25], gel hydrothermal oxidation[26], electrodeposition technique[27, 28], precipitation[29, 30, 31], rheological phase reaction and pyrolysis[32, 33] and thermal decomposition methods[34,

35, 36], that produce polycrystalline particulate samples with a rather low packing density and a low degree of sintering.[2, 5] This makes it difficult to characterize the material's intrinsic transport properties.[19] It is less studied than the well known iso-structural magnetic compounds  $\text{NiFe}_2\text{O}_4$ ,  $\text{CoFe}_2\text{O}_4$ ,  $\text{Fe}_3\text{O}_4$ , and  $\text{Co}_3\text{O}_4$ , which is partly because of its unavailability in epitaxial thin film form or single crystal form.

Among the widest class of substances studied for electrolysis in transition metal oxides,  $\text{NiCo}_2\text{O}_4$  has received great interest in many industrial applications[37] for a wide range of electrochemical reactions. Interest in  $\text{NiCo}_2\text{O}_4$  stemmed from the early work on nickel oxide and cobalt oxide.  $\text{NiCo}_2\text{O}_4$  studies explored electrical properties with interest in its superior transmission (near 80%) in visible region and it has been attempted to exploit in electrochromic window applications[38], as p-type transparent conducting films[39], an antiferromagnetic material[40], a functional sensor layer for chemical sensors[41], or a photocathode for a solar cell.[42] Cubic spinel  $\text{NiCo}_2\text{O}_4$  has also been investigated for electrical properties[43], and its conduction mechanism.[44, 45, 46, 47] Studies of nickel oxide showed experimental results, but as mentioned previously, the poor conductivity of the p-type oxides has not encouraged interest in developing p-type transparent conducting oxides (TCOs) in general for applications beyond lab experimentation.

Spinel cobalt oxide has also been studied previously as a result of its magnetic spin states[48] and optical nonlinearity.[49] Doping single crystals of cobalt oxide with nickel produced a significant increase in electrical conductivity (up to  $10^5$ ) while maintaining the spinel structure. Nickel doped cobalt oxide shows p-type semiconducting behavior similar to intrinsic spinel cobalt oxide.[50] Investigators have worked to develop nickel cobalt oxide for applications intended originally for nickel oxide or cobalt oxide.[51] Other interests in nickel-cobalt oxide include uses as electrodes in batteries[52, 53, 54], electrodes in solar cells[55], electrodes in

molten carbonate fuel cells[56], or as a heterogeneous optical recording media.[57] These intended uses of nickel-cobalt oxide are not paramount to this study but show other research interests in the material have been pursued in the past to develop specific applications such as using  $\text{NiCo}_2\text{O}_4$  as an electrocatalyst for anodic oxygen evolution[58, 14], in organic or inorganic electrosynthesis[59], as a supercapacitor[60], or as an infrared-transparent conducting electrode for flat panel displays, sensors, or optical limiters and switches.[61, 15, 62, 17] Studies of nickel-cobalt spinel have included bulk crystals[14, 59, 50] and thin films.[58, 60, 63, 5, 64, 51]

## 1.2 Motivation

Transition metal oxides exhibit a variety of fascinating and useful magnetic, electronic, and optical properties. While the oxides with perovskite structure traditionally attract most attention, spinel structure oxides have a long history of research of their own, with the most prominent example being the Verwey transition in magnetite [65]. More recently, magnetic spinel ferrites  $\text{NiFe}_2\text{O}_4$  and  $\text{CoFe}_2\text{O}_4$  have been investigated for spin filtering applications in spintronics [10, 11, 12, 13].  $\text{NiCo}_2\text{O}_4$  (NCO) is less studied than the well known isostructural magnetic spinel compounds  $\text{NiFe}_2\text{O}_4$ ,  $\text{CoFe}_2\text{O}_4$ ,  $\text{Fe}_3\text{O}_4$ , or  $\text{Co}_3\text{O}_4$  because of the unavailability of  $\text{NiCo}_2\text{O}_4$  single crystals or epitaxial films. Also, the thermal stability of poly-crystalline  $\text{NiCo}_2\text{O}_4$  film is reported to be low, which makes it difficult to study the material’s intrinsic properties. Poor conductivity of  $\text{NiCo}_2\text{O}_4$  shown by previous studies has not encouraged interest in developing p-type transparent conducting oxides (TCOs) in general for applications beyond lab experimentation. Our goal of this research is to synthesize the epitaxial  $\text{NiCo}_2\text{O}_4$  thin films and investigate the intrinsic properties.

In this research, we report the growth of highly crystalline epitaxial  $\text{NiCo}_2\text{O}_4$  thin films on  $\text{MgAl}_2\text{O}_4$  (001) single crystal substrates, and the observation of the

metallic conduction.  $\text{NiCo}_2\text{O}_4$  is believed to exhibit an inverse spinel structure with Ni cations occupying the octahedral sites while Co cations are evenly distributed to both the octahedral and tetrahedral sites.[64, 66] However, Ni ions can diffuse into the tetrahedral sites substituting Co, which is reported to cause changes in lattice constants and magnetic moments.[2, 66, 17] The magnetic structure of  $\text{NiCo}_2\text{O}_4$  has long been known[64, 67] as ferrimagnetic with a Curie temperature  $T_C$  400°C. We studied the structural, magnetic, and transport properties of the films grown at various temperature and observed a strong correlation between these properties. Furthermore, high quality epitaxial  $\text{NiCo}_2\text{O}_4$  films with the ferrimagnetic order with improved conductivity can be very useful for spintronic application.

The transport and magnetic properties of thin films depend strongly on their thickness at the ultrathin level. As the thickness becomes smaller, such observables as the resistivity, saturation magnetization, and coercive field can be influenced to a high degree by the films' geometrical boundaries, interfacial scattering, and pinning, and the crossover from three-dimensional to two dimensional physics.[68, 69, 70] A thorough understanding of a material's behavior as the function of film thickness is indispensable before it can be integrated in technological applications. In this research, we have also investigated the evolution of the resistivity and the magnetic properties of  $\text{NiCo}_2\text{O}_4$  in films down to 1 uc in thickness and found enhanced coercivity in films below 30 uc.

To understand the microscopic details of carrier transport in these  $\text{NiCo}_2\text{O}_4$  films grown at different temperatures, we have studied the frequency-dependent optical properties. We carried out tera-hertz time domain spectroscopy (THz TDS) measurement to understand the optical properties of  $\text{NiCo}_2\text{O}_4$  films grown at different temperature in the 0.3–3 THz spectral region. The complex conductivities display a Drude-type frequency response. The extrapolated DC conductivity is consistent with



our result from DC transport measurement. The temperature- and growth-condition dependent Drude parameters provide further insight in the metal-insulator transition in these materials.

### 1.3 Organization of Dissertation

Chapter 2 discusses the introduction to spinel structure and inverse spinel  $\text{NiCo}_2\text{O}_4$  and the details of the current knowledge of its basic properties. Basic properties of the  $\text{NiCo}_2\text{O}_4$  include magnetism and transport properties, low temperature quantum interference phenomena observed in  $\text{NiCo}_2\text{O}_4$  and the optical conductivity. Chapter 3 discusses the experimental techniques including the synthesis of  $\text{NiCo}_2\text{O}_4$  thin films, structural characterizations, transport and magnetic properties measurements. Chapter 4 discusses the results and discussion of the effect of growth temperature on structural, magnetic and transport properties of  $\text{NiCo}_2\text{O}_4$  thin films including the observation of metallic properties with ferrimagnetic order. The results of thickness dependent structural, magnetic and transport properties of  $\text{NiCo}_2\text{O}_4$  thin films are discussed in chapter 5 and our highlights in this chapter will be the observation of magnetism and metallic behavior down to 2  $\mu\text{m}$  thickness film and the observation of the quantum interference phenomena at low temperature transport properties. Chapter 6 discusses the theoretical and experimental details of THz time-domain spectroscopy. Chapter 7 discusses the results of the growth temperature and temperature dependent spectroscopic measurement of  $\text{NiCo}_2\text{O}_4$  thin films. Our measurement of real and imaginary parts of the dielectric function (optical conductivity) allowed us to elucidate the details of electronic conduction in  $\text{NiCo}_2\text{O}_4$  is discussed in this chapter.

## Chapter 2

# Introduction and Theoretical Background

### 2.1 Spinel Oxide

The spinel oxides have general formula  $AB_2O_4$ , where A and B are typically transition metals, a wide group of materials with various physical properties.

The spinel structure can be described as a closed-packed face-centered cubic lattice of  $O^{2-}$  ions that allows 32 octahedral and 64 tetrahedral sites for transition metal cations. The unit cell contains 32 oxygen anions and 24 cations, 8 of these cations are distributed on the 64 available tetrahedral sites (A-sites) and 16 on the 32 available octahedral sites (B-sites). The cations are distributed in the way that B-site cations form a chain along the  $[111]$  direction of the lattice. Every B-site ion has six nearest neighbors, and every A-site ion has four nearest neighbors. The distance between the ions and their nearest neighbors is the smallest for B-B neighbors, then A-B neighbors and the largest separation is between the A-A neighbors.[71]

The lattice parameter of spinel oxides is usually larger than 0.8 nm. One of the smallest lattice parameter is for  $MgAl_2O_4$  ( $a = 0.808$  nm), while cobaltites and ferrites have larger lattice parameter of around 0.812 nm and 0.834 nm ( $NiCo_2O_4$ :  $a$

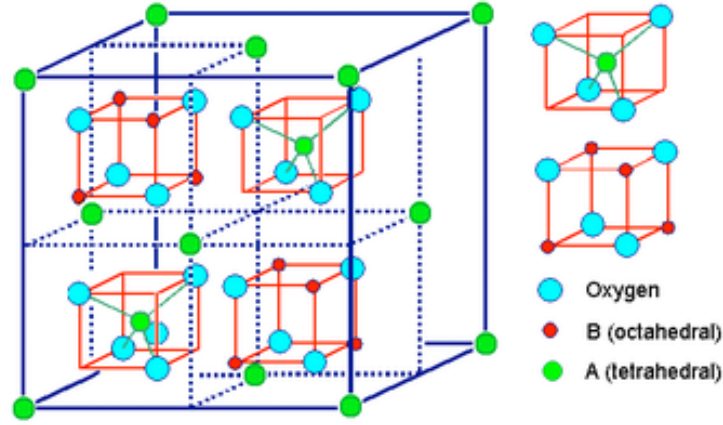


Figure 2.1: Schematic of the one unit cell of the spinel structure (a) and the interstitial sites of the cations (b).[72]

= 0.812 nm,  $\text{NiFe}_2\text{O}_4$ :  $a = 0.834$  nm).

Considering the possible cationic distributions over the two possible lattice sites, spinel has been divided into three different types; normal spinel, inverse spinel, and mixed spinel structure. In the normal spinel structure, trivalent cations are found only on B-sites, while the divalent cations occupy the A-sites (e.g.  $\text{MgAl}_2\text{O}_4$ ,  $\text{CoCr}_2\text{O}_4$ , and other chromites due to the strong A-site preference of  $\text{Cr}^{3+}$ ). In the inverse spinel structure, the divalent ions occupy half of the B-sites and the trivalent ions are distributed equally over half of the B- and over the A-sites (e.g.  $\text{NiCo}_2\text{O}_4$ ,  $\text{NiFe}_2\text{O}_4$ ,  $\text{Fe}_3\text{O}_4$ ).[2, 73, 74] The mixed structure is a mixture between the normal and inverse spinel (e.g.  $\text{CoFe}_2\text{O}_4$ ,  $(\text{Mn}, \text{Zn})\text{Fe}_2\text{O}_4$ ). [75, 76] The distribution of 3+ and 2+ cations over the A- and B-sites was addressed by theoreticians by calculating the site preference of different transition metal ions taking into account the crystal field splitting and geometric considerations. [77]

## 2.2 Inverse Spinel $\text{NiCo}_2\text{O}_4$

Inverse spinel structure are often represented by  $\text{B}[\text{AB}]\text{O}_4$ .  $\text{NiCo}_2\text{O}_4$  is known to have inverse spinel structure with structural formula  $\text{Co}[\text{NiCo}]\text{O}_4$ . Ni ion mostly

contained to the octahedral B sites and the Co ions are equally distributed between the octahedral B and tetrahedral A sites. The oxidation states of the cations have been the subject of much research and differing scenarios have been proposed[66, 19, 78, 5, 2] that cover the range  $0 \leq x \leq 1$  in the formula  $\text{Co}_{1-x}^{2+}\text{Co}_x^{3+}[\text{Co}^{3+}\text{Ni}_x^{2+}\text{Ni}_{1-x}^{3+}]\text{O}_4$ . In this notation, the cations in the square brackets reside in the B sites and the cations outside the brackets reside in the A sites. Both Marco *et al.*[2] and Battle *et al.*[19] reported a small occupation of A sites by Ni cations (up to 10%).

## 2.3 Magnetism

Spinel oxides are ferrimagnets involving two different sublattices. In order to understand the magnetic behavior of spinel oxides mainly three types of interactions are considered between the transition metal ions at A- and B- sites through intermediate oxygen ions  $\text{O}^{2-}$  i.e. superexchange interaction. Three exchange interactions  $J_{A-A}$ ,  $J_{A-B}$ , and  $J_{B-B}$  are present due to two lattice sites A and B.[79] The super exchange energy is dependent upon the distance among the magnetic ions to the oxygen ions and the spatial orientation between these ions. In spinel, the A-O-B bond angle is near  $180^\circ$ , the B-O-B and the A-O-A bond angle is near  $90^\circ$  and the A-A separation is about  $4\text{\AA}$ . These are A-A, A-B, and B-B interactions. Thus with predominating A-O-B interaction, the spins of A- and B-site ions magnetize oppositely to give a resultant magnetic moment equal to the difference between those of A- and B-site ions. Since cation-cation distances are large, direct interactions are negligible. It has been verified experimentally that these interaction energies are negative favoring antiferromagnetism when the d orbitals of the metal ions are half filled or more than half filled, while a positive interaction accompanied by ferrimagnetism results when d orbitals is less than half filled. This consists of nearest neighbor A-B interactions which align the magnetic moments of the two sub-lattice anti parallel.

$\text{NiCo}_2\text{O}_4$  shows ferrimagnetic ordering. The A and B sublattice are not structurally identical and ferrimagnetically ordered, one by the ions on the A-sites and one by those on B-sites. The intersublattice coupling between the ions on the A- and the B-sites is antiferromagnetic and relatively strong, due to the super-exchange between these ions. The intersublattice coupling between the different ions on B-sites is also antiferromagnetic but relatively weaker due to the large distance between the B-site ions. The distance between the A-site ions is also large, so the intersublattice coupling between A-site ions contribute weak to antiferromagnetic coupling.

Historically, the first experimental studies to determine the distribution and valence states of the cations in  $\text{NiCo}_2\text{O}_4$  relied on low-temperature magnetization measurements[80] that found the magnetization of  $1.5\mu_B$  per formula unit in the field of 0.8 T. To explain this observation, Blasse[81] proposed the formula  $\text{Co}^{2+}[\text{Co}^{3+}\text{Ni}^{3+}]\text{O}_4^{2-}$ , in which the magnetic moments of the high-spin A-site  $\text{Co}^{2+}$  cations couple antiferromagnetically with the low-spin B-site  $\text{Ni}^{3+}$  cations to produce the ferrimagnetic magnetization of  $2\mu_B/\text{fu}$ . The B-site  $\text{Co}^{3+}$  are diamagnetic in this model. Subsequent magnetization and neutron diffraction studies[66, 19, 2] confirmed the inverse cationic distribution and the ferrimagnetic coupling between the sublattices. The reported magnetization values fall in the  $1.25\text{-}1.52\mu_B/\text{fu}$  range in 0.8 T field, which also agrees with the magnetization measurements on epitaxial low-temperature-grown  $\text{NiCo}_2\text{O}_4$  films reported in our work[82]. Another intriguing feature of the  $\text{NiCo}_2\text{O}_4$  magnetic properties is the lack of magnetization saturation in fields up to 1.1 T[80, 66, 2, 82]. Together with the low measured spontaneous magnetization, this motivated the search for alternatives to Blasse's model.

The model proposed by Battle *et al.* based on their neutron diffraction study corresponds to the structural formula[19]

$$\text{Co}_{1-z}^{(3-\delta)+}\text{Ni}_z^{3+}[\text{Co}^{3+}\text{Ni}^{(2+\delta-z\delta)+}]\text{O}_4^{2-}, \quad (2.1)$$

with  $\delta \approx 0.35$  and  $z \approx 0.08$ . The model suggests the average A-site and B-site magnetic moments of  $\langle m_A \rangle \approx 2.4 \mu_B$  and  $\langle m_B \rangle \approx -0.8 \mu_B$  and the saturation magnetization  $\langle m_S \rangle \approx 0.8 \mu_B$ . The refinement of the magnetic structure from experimental neutron diffraction patterns yielded the mean values  $\langle m_A \rangle \approx 2.29(9) \mu_B$ ,  $\langle m_B \rangle \approx -0.97(13) \mu_B$ , and the saturation magnetization  $\langle m_S \rangle \approx 0.35(28) \mu_B$ . Battle *et al.* explain the difference between their value of  $\langle m_S \rangle$  deduced from neutron diffraction and the measured magnetization values[80, 66, 64] by the field dependence of the spontaneous magnetization. Application of the magnetic field in this model alters the parameter  $\delta$  in Eq. (2.1) and increases the spontaneous magnetization. The electronic energy bands corresponding to the cations in the Battle's model are shown in Fig. 2.2(a), where the energy of the  $e_g$  band of the B-site Ni overlaps with the energy of the A-site Co bands. The model assumes that the exchange splitting  $\Delta_{EX}$  on the A-site Co cation is less than the crystal field splitting  $\Delta_{CF}$ , so that the holes at the A-site Co are introduced in the majority spin  $t_{2\uparrow}^3$  band rather than the minority spin  $e_{\downarrow}^2$  band. Holes in the B-site Ni also belong in the majority spin band, which means that the hole transport from A-site Co to B-site Ni must involve the change of spin.

The Battle model provides a plausible explanation of the magnetization data. However, the study of  $\text{NiCo}_2\text{O}_4$  by neutron diffraction, X-ray absorption near edge structure, and by extended X-ray absorption fine structure carried out by Marco *et al.*[64] found evidence for the presence of  $\text{Ni}^{4+}$  ions in the material. Their magnetic structure refinement assigned an average magnetic moment of  $\langle m_A \rangle = 2.18(9) \mu_B$  to tetrahedral sites and the moment of  $\langle m_B \rangle = -1.49(8) \mu_B$  to octahedral sites. The A-site moment is consistent with their  $\text{Co}^{2+}$  occupancy, as Co adopts the high-spin  $d^7$  configuration in the tetrahedral oxygen coordination. The high magnetic moment on the B sites results from charge transfer between octahedral Ni and Co, which leads

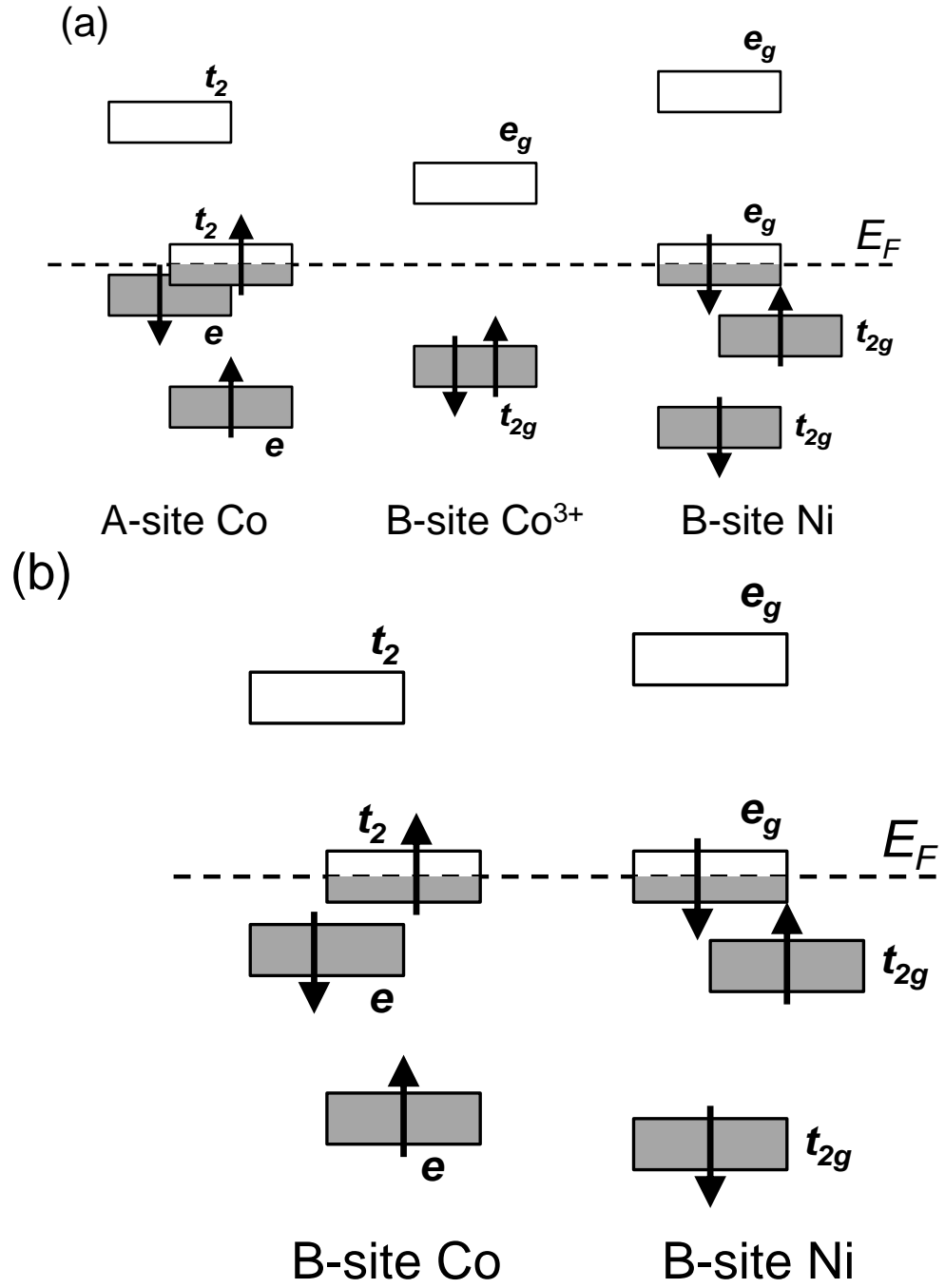


Figure 2.2: (a) Schematic representation of the energy bands in the Battle model (adapted from ref. [19]). The A-site Co  $t_2$  band and the B-site Ni  $e_g$  bands overlap and allow hole transport with a spin flip. (b) Schematic of the B-site energy bands in the Marco model (adapted from ref. [64]). The Co  $t_{2g}$  and the Ni  $e_g$  bands overlap to allow hole transport with a spin flip.

to the high spin  $\text{Co}^{2.5+}$  and low spin  $\text{Ni}^{3.5+}$  valencies. Marco *et al.* proposed the electronic configuration

$$\text{Ni}_{0.1}^{3+}\text{Co}_{0.9}^{2+}[\text{Co}_{1.1}^{2.5+}\text{Ni}_{0.9}^{3.5+}]\text{O}_4^{2-}, \quad (2.2)$$

which is also illustrated in Fig. 2.2(b). The minority spin Co  $t_{2g}$  states and the majority spin Ni  $e_g$  states overlap in energy and form a band, although the transport of charge between octahedral Co and Ni in the ferrimagnetic state must involve a spin flip. Marco *et al.* also observed the field dependent saturation magnetization, similar to earlier reports[80, 66], which they explained by the field-depedent charge distribution between the octahedral Ni and Co cations.

## 2.4 Conduction mechanism in $\text{NiCo}_2\text{O}_4$

The p-type thermally activated conductivity was observed in the recent work of Windish *et al.* on sputtered  $\text{NiCo}_2\text{O}_4$  films[15, 16, 17]. A polaron is a charge carrier electron or hole trapped into distorted neighbor lattice. So it is described as an entity including both the displaced neighboring atoms and the charge carrier.[83, 84] The descriptions of Battle and Marco suggest metallic band-like p-type transport in  $\text{NiCo}_2\text{O}_4$ . The metallic behavior, however, has not been reported until our recent work on epitaxial films grown by PLD[82]. The high conductivity and metallic behavior shown by our epitaxial  $\text{NiCo}_2\text{O}_4$  thin films is a characteristic of free carriers[82] and our spectroscopic study rule out a crossover to small polaron hopping reported in earlier works on  $\text{NiCo}_2\text{O}_4$ . [15, 16, 17]

## 2.5 Classical Transport

Ohm's law in terms of current density  $\vec{j}$  and electric field  $\vec{E}$  is can be written as,

$$\vec{j} = \sigma \vec{E} \quad (2.3)$$



where  $\sigma$  is the conductivity of the material. If the conduction electron density of a metal is  $n$  and these electrons move collectively with a velocity  $v$ , then the current density within the metal is,

$$\vec{j} = -ne\vec{v} \quad (2.4)$$

and

$$v = \frac{e\vec{E}t}{m} \quad (2.5)$$

Combining equations (2.4) and (2.5), the current density,

$$\vec{j} = \frac{ne^2\vec{E}t}{m} \quad (2.6)$$

Comparing equations (2.5), (2.6), and (2.7), the conductivity is  $\frac{ne^2t}{m}$ . However, all electrons inside metal do not move collectively. Electrons are moving randomly throughout the metal with an average velocity of zero in the absence of potential gradient. Once the electric field is applied, electrons accelerate in response to the applied electric field. Hence  $t$  can be replaced by the average time between collisions or relaxation time  $\tau$  in the expression,

$$\sigma = \frac{ne^2\tau}{m} \quad (2.7)$$

This is known as Drude conductivity.[85, 86] At low temperature, Drude theory predicts that the resistivity,  $\rho = \frac{1}{\sigma}$  reaches a constant value (residual resistivity ( $\rho_0$ )), determined only by the average impurity concentration in the sample. There exist a number of quantum effects which lead to deviations from this constant residual resistivity. The interference of electron waves scattered off impurities in a disordered metal gives rise to quantum corrections to the classical Drude resistance.

## Diffusive Motion

If an electron travels for longer than the relaxation time  $\tau$ , then the distance of the electron travel will not be the velocity multiplied by time. Because of the multiple collisions, the electron's path is quite complicated. This is known as diffusive motion. In this case the, the important quantity is not the velocity of the electron but the diffusion constant of the metal. If an electron travels for time  $t$  through a metal with diffusion constant  $D$ , then the distance  $L$  is;

$$L = \sqrt{Dt} \quad (2.8)$$

If the mean free path  $l$  and Fermi velocity of a metal are known, then  $D$  can be calculated as,

$$D = \frac{1}{d} v_f l \quad (2.9)$$

where  $d$  is the dimension of the metal for diffusive motion.

## 2.6 Quantum Interference Effect

The introduction of randomly distributed impurities changes the electrical characteristics of metal. An electron wave scattering off an impurity produces partial waves which can interfere coherently among themselves, and it is this interference that leads to corrections to the classically expected behavior.[87] The size of the corrections is strongly dependent on the length over which the waves can retain phase memory, i.e the shorter this length, the smaller the interference effect. Consider a free electron with partial wave function

$$\psi_j(\vec{x}) = A_j(\vec{x})e^{i\phi_j} \quad (2.10)$$

where  $j$  represents each possible path the electron can take through the metal and  $\vec{x} = 0$  is the initial position of the electron. Therefore the probability of the electron to

be at any point  $\vec{x}$  is,

$$P(\vec{x}) = \left| \sum_j A_j(\vec{x}) e^{i\phi_j} \right|^2 \quad (2.11)$$

For example if there are only two possible path 1 and path 2, then,

$$P(\vec{x}) = |A_1|^2 + |A_2|^2 + 2|A_1 * A_2| \cos(\phi_1 - \phi_2) \quad (2.12)$$

The cosine term is due to the interference and it adds to the probability for an electron to remain at a point. Since the probability of finding an electron at a point is increased, and its probability to be anywhere else is lowered. Hence the electron does not contribute to the conduction and the result is an increased resistance.

### Elastic Mean Free Path

Due to the irregularities in the lattice such as impurities or dislocations, elastic scattering occurs. In order to find the elastic length  $l_e$  one must calculate the average time between elastic scattering events,  $\tau_e$ , whose value can be extracted from the electron mobility  $\mu_e$ , given by

$$\mu_e = \frac{e\tau_e}{m^*} \quad (2.13)$$

where  $e$  is the electronic charge and  $m^*$  is the effective mass respectively. The electron mobility is determined from the electron concentration  $n_e$  and Drude conductivity  $\sigma_0$  as,

$$\mu_e = \frac{\sigma_0}{en_e} \quad (2.14)$$

Experimentally,  $n_e$  can be obtained from Hall measurement and  $\sigma_0$  can be deduced from resistance measurement. Since only the electrons close to the Fermi surface scatters, the elastic mean free path  $l_e$  can be calculated as,

$$l_e = \tau_e v_f \quad (2.15)$$

Where  $v_f$  is the Fermi velocity.

### **Inelastic Mean Free Path**

In addition to elastic scattering, electron scattering can also be connected to energy transfer. For example, an electron moving inside crystal will be scattered by lattice vibrations and can lose or gain energy depending upon either it excites or excited by the lattice vibrations. As energy transfer occurs, the scattering is considered as inelastic scattering. The inelastic mean free path  $l_{in}$  is the measure of the length between scattering events. Besides electron-phonon, electron-electron scattering is another possible process of energy transfer.

### **Electron Phase Coherence**

For quantum interference to occur, coherent wave propagation is the prerequisite. This condition is only fulfilled at low temperature, where inelastic scattering is suppressed. There are 3 different scattering process that cause dephasing of conduction electrons: electron-electron interactions, electron-phonon interactions, and spin-flip scattering by magnetic impurities.

### **Phase Coherence Length**

Phase coherence length  $l_\phi$  is the distance over which electron propagates coherently before its phase is randomized. At low temperatures,  $l_\phi$  can be larger than  $l_e$ . Thus, a number of elastic scattering events happen before phase randomization. During elastic scattering, the phase of the event is not randomized, only shifted by well-defined amount. Whereas in inelastic scattering, the scattering target changes with time. Hence the phase shift acquired by the electron each time, is different. Thus the inelastic scattering results in dephasing of the conduction electrons. As the temperature decreases, available phonons to absorb or emit, decreases, resulting in a decreased dephasing rate.

Spin-flip interactions take place in a system containing magnetic impurities.

Such impurities can create a local magnetic field. When the conduction electrons are near to a magnetic impurity, its spin can couple to the local magnetic moment causing the spin to flip sign. The higher the density of magnetic impurities in the system, its more likely to occur such spin-flip process.

At low temperature, a number of elastic scattering events occur until the phase is randomized. Which means that the dephasing time  $\tau_\phi$  is larger than the elastic scattering time  $\tau_e$ . Owing to the diffusive motion during  $\tau_\phi$ , the phase coherence length can be written as,

$$l_\phi = \sqrt{D\tau_\phi} \quad (2.16)$$

where  $D$  is the diffusion constant defined as,

$$D = \frac{1}{2}v_f^2\tau_e \quad (2.17)$$

with  $d$  the dimensionality of the system.

## 2.7 Electron Dephasing Mechanism

There are a large number of scattering mechanisms which can contribute to the dephasing rate. In this section we will discuss only those which are relevant to this study.

### 2.7.1 Electron-electron interaction

The Coulomb interaction between electrons leads to a finite decay rate for electrons in a particular energy state. For a metal without any disorder (clean limit), the inelastic electron-electron scattering rate can be derived from a simple phase argument and is found to be proportional to  $T^2$ [86]. This arises from the following phase space argument, at thermal equilibrium, the Pauli exclusion principle requires that only those electrons which lie within a thin shell of width  $K_B T$  of the Fermi energy

can participate in a scattering event. Likewise the only states which an electron can scatter into must also lie within a shell of width  $K_B T$  of  $E_F$ . Thus,  $\tau_{ee} \propto K_B T^2$ .

In the presence of impurities (dirty limit), the interaction between electrons is an indirect one and is modified due to the diffusive motion of electron, where an electron typically undergoes many elastic collisions with impurities before interacting with other electrons. The collisions occur not between free electrons but between electrons diffusing through impurities. The diffusive motion increases the interaction time between electrons, increasing the interaction rate which now goes as  $\tau_{ee} \propto T^{d/2}$ . [88, 89] Here  $d$  is the sample dimension.

## 2.7.2 Electron-phonon Scattering

Atoms in a solid are confined to a site in the lattice structure, and at 0 K, the motion of an electron through the lattice is unimpeded. At higher temperatures, however, the atoms vibrate around their equilibrium positions, resulting in scattering of free electrons moving through the solid. The quantum of energy of a lattice vibration is a phonon. Scattering of electrons by phonons at finite temperature is an unavoidable phenomenon, and this intrinsic resistivity is typically the dominant source of resistivity in metals at room temperature. The familiar result is that at high temperature the resistivity of a metal  $\rho$  is proportional to temperature  $T$ . This reflects the bosonic nature of the phonons that scatter the electrons: at temperatures greater than the Debye temperature  $\theta_D$ , the characteristic temperature at which all phonon modes of a crystal are excited, the phonon population in any given mode is proportional to  $T$ , hence the number of scatterers and the resistivity are proportional to  $T$ . Below the Debye temperature, the phonon modes begin to freeze out, and in a typical metal the resistivity drops much more rapidly.

The average number of phonons in a given mode is described by the Planck

distribution,

$$\langle n \rangle = \frac{1}{e^{\hbar\omega/k_B T} - 1} \quad (2.18)$$

In the Debye model, the density of these modes is given as,

$$D(\omega) = \frac{V\omega^2}{2\pi^2 C_s^3} \quad (2.19)$$

where  $V$  is the volume of the solid and  $C_s$  is the speed of sound.[85] The total average number of phonons in the lattice is given by,

$$\langle n_{tot} \rangle = \int D(\omega) \langle n \rangle d\omega \quad (2.20)$$

For a unit volume and counting for the three phonon polarizations, this results in,

$$\langle n_{tot} \rangle = \frac{3}{2\pi^2 C_s^3} \int_0^{\omega_D} \frac{\omega^2}{e^{\hbar\omega/k_B T} - 1} d\omega \quad (2.21)$$

where  $\omega_D$  is the maximum mode that can be supported by the solid. The Debye temperature is related to the maximum mode frequency by  $\theta_D = \hbar\omega_D/k_B$ . For  $T \ll \theta_D$ ,  $\langle n_{tot} \rangle$  goes as  $T^3$ , and for  $T \gg \theta_D$ ,  $\langle n_{tot} \rangle$  goes linearly with  $T$ . [86] Since more oscillations make it more difficult for an electron to move through a solid, hence the resistivity is proportional to  $\langle n_{tot} \rangle$ .

For  $T$  well below  $\theta_D$ , the net electron-phonon scattering can be shown [86] to decline as  $T^3$ . However, as the temperature lowers, the phonons have less energy and are less able to change the velocity of the electron, and scattering becomes more concentrated in a forward direction. At sufficiently low temperatures, phonon scattering is very nearly elastic, introducing a  $T^2$  dependent term.[86] The resulting dependence

is known as the Bloch  $T^5$  law,

$$\rho = T^5, T \ll \theta_D \quad (2.22)$$

### 2.7.3 Weak Localization

Interference effects of electron waves due to phase coherent transport can be seen in large samples, where the phase coherence length is much smaller than the dimensions of the sample. This effect is called "Weak Localization" and results in an increased resistance. Weak localization is observed at sufficiently low temperature when the phase coherence length  $l_\phi$  is larger than elastic scattering length  $l_e$ .

As in classical diffusion, an electron will propagate through a metal colliding elastically into defects that randomize its momentum and phase.

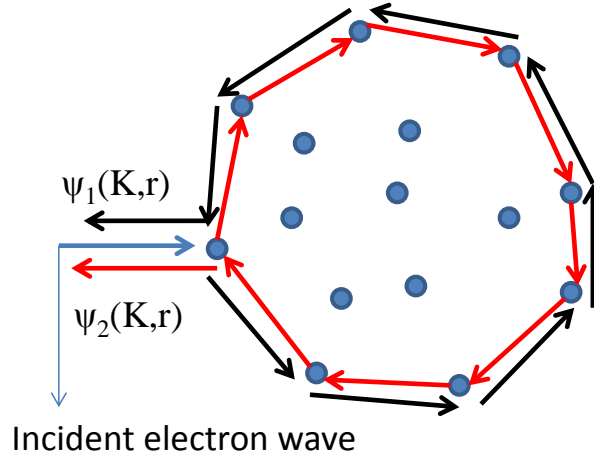


Figure 2.3: The mechanism of weak localization. A pair of time reversal symmetric loop for electron path is shown in red and black respectively.

The electron quantum interference effect involves the interference of electron waves in a disordered solid. Each possible path of the electron is associated with a probability amplitude  $\psi$ , whose modulus squared  $|\psi(\vec{r})|^2$  is the probability of finding an electron at point  $\vec{r}$ . Different electron trajectories originating from the same starting point can interfere constructively to some distance as long as they are



in phase. There are two kinds of interference paths which contribute quantum corrections to the low temperature resistance; time-reversed and non time-reversed. Weak localization occurs due to the time-reversed path. In time -reversed path, electron trajectories are identical except that they are traversed in precise time-reversed order. Clearly, the interference due to time-reversed path occurs at the the point of origin (O)[90, 91, 92] as shown in fig.2.3.

The total probability  $P(\vec{r})$  of finding an electron at point  $\vec{r}$  is given by by the square of the sum of the probability amplitudes associated with all the possible paths the electron can traverse. Thus,

$$P(\vec{r}) = \left| \sum_i \psi_i \right|^2 \quad (2.23)$$

From equation (2.14);

$$P(\vec{r}) = \sum_i |\psi_i|^2 + \sum_{i \neq j} \psi_i \psi_j^* \quad (2.24)$$

where  $\psi_j^*$  is the complex conjugate of  $\psi_j$ . For the two paths in fig. (2.3), the interference term can be very small. For many such paths, the fractional contribution of the interference term will be negligible compared to the classical contribution.

For the time-reversed path shown in fig. (2.3),

$$P(O) = |\psi_1|^2 + |\psi_2|^2 + \psi_1 \psi_2^* + \psi_1^* \psi_2 = |\psi_1|^2 + |\psi_2|^2 + 2\text{Re}(\psi_1^* \psi_2) = 4|\psi_1|^2 \quad (2.25)$$

where path 1 and 2 are exact time-reversed pair. Hence, the probability of finding an electron at point O is twice the classical probability. Because of this increased probability, the electron is said to be weakly localized at point O and the result is measured as an increase in resistance over the classical Drude resistance. Since the electron has returned to its initial point via elastic scattering, its momentum is equal

in magnitude but the net momentum direction compared to its initial momentum direction will be opposite. The assumption that the electron has returned to its initial position via elastic scattering is valid since  $l_{in} \gg l_e$  in most disordered metals at the temperature of interest. Hence, weak localization can be thought of as enhanced back scattering. The fact that electron has higher back scattering should decrease the conductivity of the metal.

#### 2.7.4 Scattering by Magnetic Impurities

When magnetic impurities are present in the sample, the spin of the electron may interact with the magnetic moment of the impurity. Magnetic scattering tends to suppress quantum interference, with the magnetic impurities either acting as sources of magnetic flux, which adds to the phases of the time-reversed trajectories so as to diminish the interference, or as centers of spin-flip scattering, which rotates the electron spins and destroys phase coherence. It is well known that coupling of magnetic impurities to the conduction electron gives rise to the well known Kondo effect.[93, 94] This gives rise to resistivity contribution as  $\log(T)$ , [90, 95] hence the total resistivity can be represented as,

$$\rho = aT^5 + c\rho_0 - c\rho_1 \log(T) \quad (2.26)$$

where,  $T^5$  is the functional temperature dependence of electron-phonon interaction,  $\rho_0$  is the residual resistivity,  $c$  is the concentration of magnetic impurities,  $\rho_1 = \frac{3zJ\rho_M}{E_F}$ ,  $J$  is the exchange energy,  $z$  is the number of nearest neighbors,  $\rho_M$  is a measure of the strength of the exchange scattering.[85]

## 2.8 Optical Conductivity

Optical conductivity also known as dynamic conductivity, or AC conductivity, is defined as the conductivity of a medium as a function of frequency. While the DC conductivity characterizes the overall electron transport behavior, the frequency dependence of AC conductivity contains important information on scattering events and interactions. These effects can influence the frequency and temperature dependence of the conductivity sometimes in a very specific way.

When a homogeneous medium is illuminated by an external electric field, a charge redistribution occurs and a current is produced. Such induced currents are proportional to inducing fields as,

$$J(\omega) = \sigma(\omega)E(\omega) \quad (2.27)$$

Where  $J$  and  $E$  are total current and electric field,  $\omega$  is interacting optical frequency,  $\sigma$  is the optical conductivity. The optical conductivity is complex and generally expressed as,

$$\sigma(\omega) = \sigma_1 + i\sigma_2 \quad (2.28)$$

The dielectric function  $\epsilon(\omega)$  is related to the electric displacement  $D$  and the electric field  $E$  as,

$$D(\omega) = \epsilon(\omega)E(\omega) \quad (2.29)$$

The dielectric function can be directly expressed in terms of optical conductivity as,

$$\epsilon(\omega) = 1 + \frac{4\pi\sigma(\omega)}{\omega} \quad (2.30)$$

The complex refractive index  $n(\omega)$  of the medium is related to the complex dielectric

function  $\epsilon(\omega)$  by

$$n(\omega) = \sqrt{\epsilon(\omega)} = n(\omega) + iK(\omega) \quad (2.31)$$

The directly accessible functions from optical measurements are transmittance  $T(\omega)$ , the reflectance  $R(\omega)$ , the refractive index  $n(\omega)$ , and the extinction coefficient  $K(\omega)$ . [85, 86] The dielectric function  $\epsilon(\omega)$ , and the optical conductivity  $\sigma(\omega)$  are then computed using the above relations.

### Dielectric properties of Metals: The Drude Model

The dynamical conductivity of electrons in a free electron metal is treated with the classical Drude model. The Drude model ignores all the interactions between electrons beyond the long range Coulomb forces, all effects due to the periodic potential imposed by the crystal structure and the Coulomb attraction of the positive ion cores. The main result of Drude theory, can be summarized in the form of optical conductivity as,

$$\sigma(\omega) = \frac{\sigma_0}{1 - i\omega\tau} \quad (2.32)$$

Where the DC conductivity is  $\sigma_0 = \frac{ne^2\tau}{m}$ ,  $n$  is the charge carrier density,  $m$  is the mass,  $e$  is the charge, and the  $\tau$  is the life-time of the charge carrier.

$$\sigma_1 = \frac{\sigma_{dc}}{1 + \omega^2\tau^2} \quad (2.33)$$

$$\sigma_2 = \frac{\omega\tau\sigma_{dc}}{1 + \omega^2\tau^2} \quad (2.34)$$

The real part,  $\sigma_1$ , is constant at low frequencies but, as frequency increases, it decreases as  $1/\omega^2$  at frequencies above  $1/\tau$ . The imaginary part starts off linear in  $\omega$  and has maximum at  $\omega = 1/\tau$  (where  $\sigma_1 = \sigma_2$ ) and falls as  $1/\omega$  at higher frequencies. [96]

The shape of the Drude conductivity curve is always same; a peak in  $\sigma_1(\omega)$  at

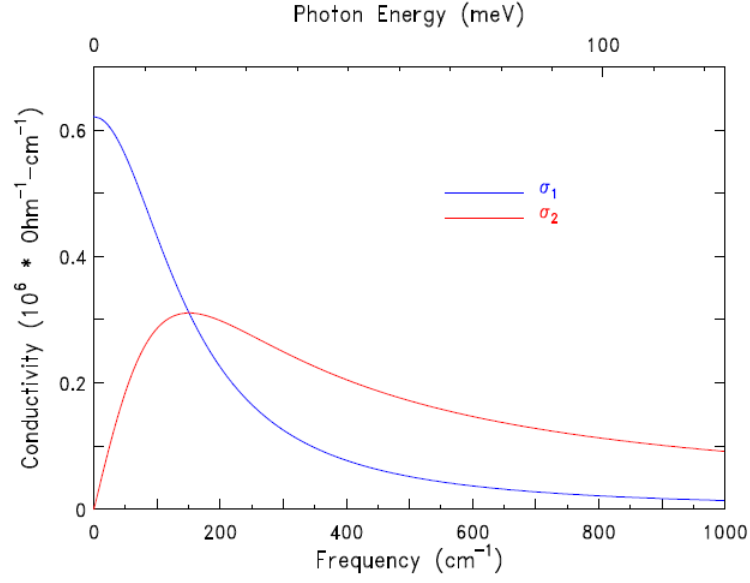


Figure 2.4: Real and imaginary parts of conductivity of a Drude metal.[96]

zero frequency and a hump-like feature in  $\sigma_2(\omega)$ . The parameter  $\omega_p^2$  represents the area under the  $\sigma_1(\omega)$  curve and  $1/\tau$  is the full width at half maximum.[96]

The generalized expressions for the dielectric function  $\epsilon$  is,

$$\epsilon(\omega) = \epsilon_\infty - \frac{\omega_p^2}{\omega^2 + i\omega/\tau} \quad (2.35)$$

The real and imaginary parts of  $\epsilon$  are,

$$\epsilon_1 = \epsilon_\infty - \frac{\omega_p^2}{\omega^2 + 1/\tau^2} \quad (2.36)$$

$$\epsilon_2 = \frac{\omega_p^2}{\omega\tau(\omega^2 + 1/\tau^2)} \quad (2.37)$$

## Chapter 3

# Thin Film Deposition and Characterization

### 3.1 Pulsed Laser Deposition

Pulsed laser deposition (PLD) is a physical vapor deposition process carried out in a vacuum system. The film is formed by atoms directly transported from source to substrate through gas phase. PLD is widely known for its precision in layer by layer growth, and the ability for the construction of superlattices[97, 98]. Our home built PLD system [99] consists of multi-port vacuum chamber, a mechanical pump, a turbo molecular pump and a UV KrF ( $\lambda = 248$  nm)excimer laser and optical lens to focus the laser onto the target . We have designed a cross-hatch, rotating target holder inside the chamber which gives additional flexibility and allows for the layer by layer growth. Aligned directly in front of the target holder, we have a substrate heater constructed with a seal-able flange at one end. The substrate is directly mounted on the heater with a silver paint. Our PLD system also allows use of apertures which can control the growth rate in another way. A schematic diagram is shown in figure(3.1).

The PLD process can be divided into the following process,

1. Laser and target surface interaction

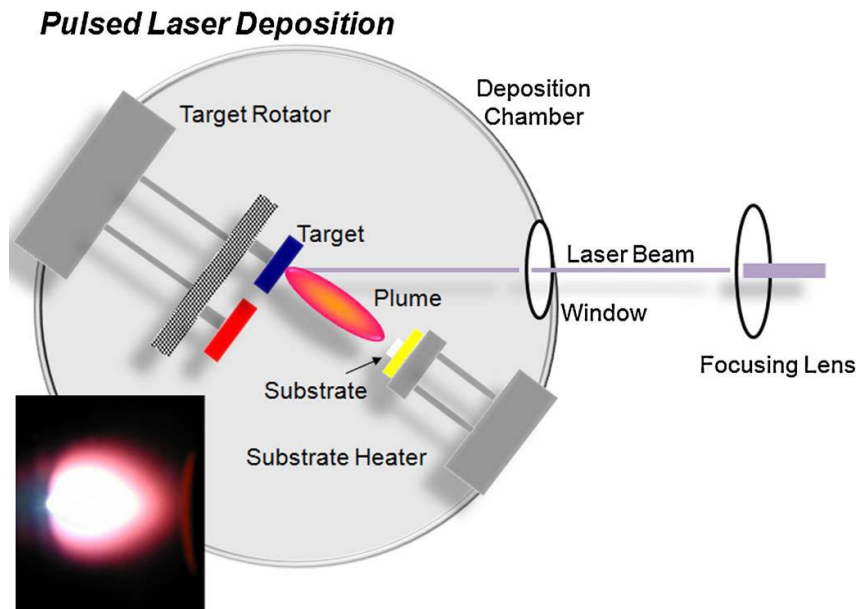


Figure 3.1: A schematic diagram of Pulsed laser deposition system.[100]

A pulsed laser beam is focused onto the surface of a ceramic target by an optical lens. The surface layer of the target material is evaporated when the laser beam strikes a small region of the target, forming a plasma plume with high energetic species.

## 2. Plume expansion

The material evaporated from the target is highly energized and consists of excited and ionized species forming the plasma. The plasma expands away from the target with a strongly forward-directed trajectory toward a heated substrate placed directly in the line of the plume.

## 3. Film deposition

The dissociated energetic species impinge onto the substrate surface which is mounted on the heater and placed 5 cm away from the target, allowing for uniform coverage of the substrate from the plume. An equilibrium is established between the incoming and re-evaporating species depending on the rate of the particles and substrate temperature, which in turn determines the film growth rate. The crystalline film growth depends on the surface diffusion of the atoms. Normally, the atom will dif-

fuse through several atomic distances before sticking to a stable position within the newly formed film. High temperature gives atoms high mobility resulting in rapid and defect free crystal growth, whereas a crystal grown at low temperatures may be dominated by the energetic particle impingement, resulting in disordered or even amorphous structures.

Each stage in PLD is critical to the formation of high quality thin film in terms of epitaxy, stoichiometry, and surface roughness. Several parameters need to be optimized for specific material growth, such as temperature, laser energy density and frequency, background pressure, and target to substrate distance.

### **3.1.1 Advantages of Pulsed Laser Deposition**

PLD is one of the more effective and efficient method of thin film growth. It produces a highly forward-directed and confined plume of materials which can be deposited with less contamination. In addition, PLD is incredibly precise. Other advantages of using PLD include the fact that the complex stoichiometry is preserved well during process. Making multilayer materials can also be done rather easily with PLD, because different targets can be positioned under the laser beam. Film growth rates may be controlled to any desired value. Almost any kind of condensed matter material can be ablated in PLD.

### **3.1.2 Drawbacks of Pulsed Laser Deposition**

There are some drawbacks on PLD. One of the major problems is the splashing or the deposition of particulates on the film. Two main causes for particle formation during laser evaporation are the breakaway of surface defects under thermal shock and splashing of liquid material due to super heating of subsurface layers. Some methods have been developed to reduce splashing. One is using a mechanical particle filter that consists of a velocity selector that acts as a high-velocity pass filter to remove



slow moving particulates. The second is using targets of high density and smooth surface, one effective improvement is to polish the target surface before each run. The third is using relatively low energy density or low deposition rate.

Another problem is the lack of uniformity over a large area of the plume, due to the narrow angular distribution of the plume that comes out from the target surface.

## 3.2 Structural Analysis

X-ray diffraction (XRD) is a versatile, non-destructive technique to identify the crystalline phases present in the solid material and analyze the structural properties. XRD provides the quantitative information about the crystal structure and crystalline quality of thin films and multilayer samples. The working principle of X-ray diffractometer is based on diffraction of X-ray waves which has the same order of wavelength with the lattice parameters in the crystal.  $K\alpha_1$  is generally used for diffraction which is produced from the copper target in X-ray generator. The wavelength of this radiation is  $1.54059 \text{ \AA}$ . We use Bruker D8 Discover four-circle high-resolution X-ray diffractometer (HR-XRD). The diffractometer has four axes, the  $\omega$  axis (sample rotation axis), the  $\Phi$  axis (in-plane rotation axis), the  $\chi$  axis (tilting axis), and the  $2\theta$  axis for scanning the detector.

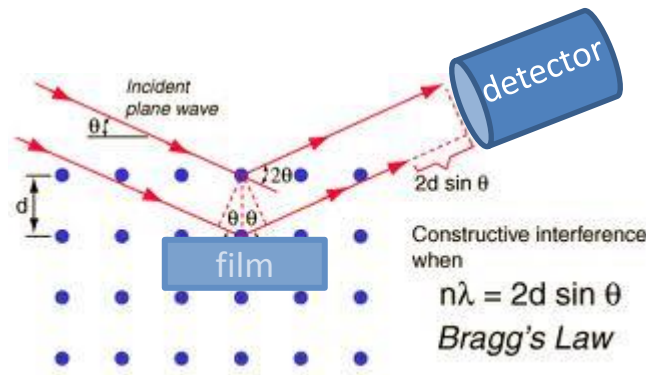


Figure 3.2: Schematic representation of X-ray diffraction

### 3.2.1 $2\theta$ - $\omega$ Scan

To obtain the out-of-plane lattice parameter of the film and substrate, a  $2\theta$ - $\omega$  Scan is performed. It is a coupled scan, in which the condition  $\theta=\omega$  must hold over the range of  $2\theta$  values measured. In practice, substrate miscut and sample mounting often cause small deviations from this condition decreasing the diffracted X-ray beam intensity. To resolve these experimental errors, a small offset,  $\delta$ , is calculated to re-establish the optimal diffraction condition such that  $2\theta = 2(\omega+\delta)$ .  $2\theta$ - $\omega$  Scan is used to measure the Bragg diffraction angle. In  $2\theta$ - $\omega$  scan, the source is fixed but the sample rotates  $\theta$  and the detector rotates  $2\theta$ .

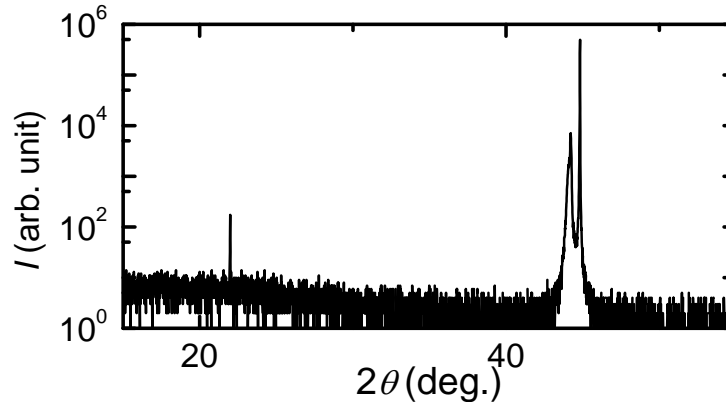


Figure 3.3: HR-XRD  $2\theta$ - $\omega$  scan of a 240nm thick  $\text{NiCo}_2\text{O}_4$  film grown at  $350^\circ\text{C}$  on  $\text{MgAl}_2\text{O}_4$  (001) substrate.

### 3.2.2 The $\omega$ scan or Rocking Curve

Rocking curves are primarily used to study defects such as dislocation density, mosaic spread, curvature, misorientation, and inhomogeneity. In the  $\omega$  scan, the source is fixed, the detector is fixed but the sample is rocked around the Bragg peak slightly. A perfect crystal has an intrinsic full width at half maximum (FWHM) for that material and defects cause the rocking curve to broaden beyond the intrinsic width for the Bragg peak. A rocking curve is a plot of x-ray intensity vs  $\omega$ . Figure (3.4) shows the rocking curve of  $\text{NiCo}_2\text{O}_4$  film on  $\text{MgAl}_2\text{O}_4$ (001) around (004) reflection

with FWHM value  $0.004^\circ$ , similar to substrate MAO ( $0.004^\circ$ ) indicating the high crystalline quality of the films.

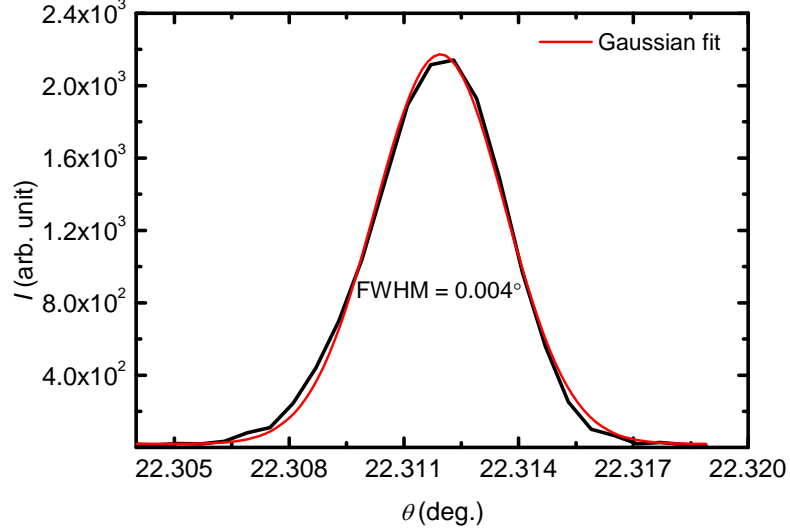


Figure 3.4: (004) rocking curve of the  $\text{NiCo}_2\text{O}_4$  film grown at  $250^\circ\text{C}$

### 3.2.3 The $\Phi$ -Scan

To determine the in-plane epitaxial relationship between the film and the substrate, a  $\Phi$ -scan is carried out. In the  $\Phi$ -scan,  $\omega$  and  $\theta$  are kept constant and the sample is rotated around the  $\Phi$  axis. For our sample, this corresponds to a rotation around the  $[001]$ -axis. Hence for asymmetric reflections  $hkl$ , by performing a  $\Phi$ -scan of  $360^\circ$ , four peaks with a separation of  $90^\circ$  can be observed in accordance to the four-fold symmetry. By conducting such  $\Phi$ -scan for the film on top of the substrate, the epitaxial relationship between the film and the substrate can be established. Figure (3.5) shows the  $\Phi$ -scan of (404)  $\text{NiCo}_2\text{O}_4$  on  $\text{MgAl}_2\text{O}_4$  (001). The 4-fold symmetry from  $\text{NiCo}_2\text{O}_4$  (404) confirms the epitaxial growth with  $\text{NiCo}_2\text{O}_4$   $[100] \parallel \text{MgAl}_2\text{O}_4$   $[100]$  and  $\text{NiCo}_2\text{O}_4$  (001)  $\parallel \text{MgAl}_2\text{O}_4$  (001).

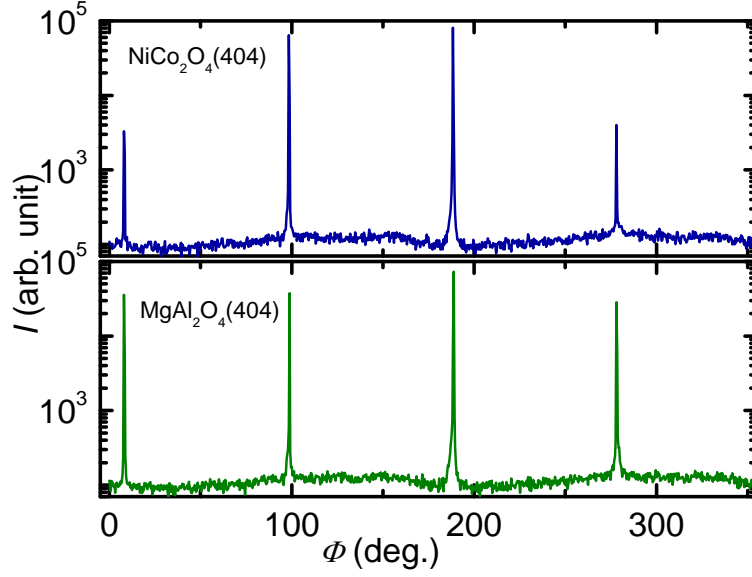


Figure 3.5:  $\Phi$  scans of the  $\text{NiCo}_2\text{O}_4$  (404) and  $\text{MgAl}_2\text{O}_4$  (404) reflections

### 3.2.4 Reciprocal Space Map (RSM)

Reciprocal space mapping (RSM) is a coupled  $2\theta$ - $\omega$  Scan at different  $\omega$  positions. The intensity will be represented by the color scheme and the peak shape refers the quality of the single crystal thin film, the peak broadens in the presence of defects. Both the in-plane and out-of-plane lattice constant can be calculated and the information regarding the lattice relaxation can be obtained with the RSM scan.

### 3.2.5 X-Ray Reflectivity Scan (XRR)

X-Ray reflectivity (XRR) scan is used to measure the thickness of an epitaxial film. At every interface, a portion of x-rays is reflected. Interference of these partially reflected x-ray beams creates a reflectometry pattern. X-ray reflectivity is a useful technique for structural characterization of thin films. Information about the thickness and the roughness of such samples can be obtained. Diffuse scattering of x-rays give also the information about the roughness. The fringe width ( $\Delta q$ ) in radian, is

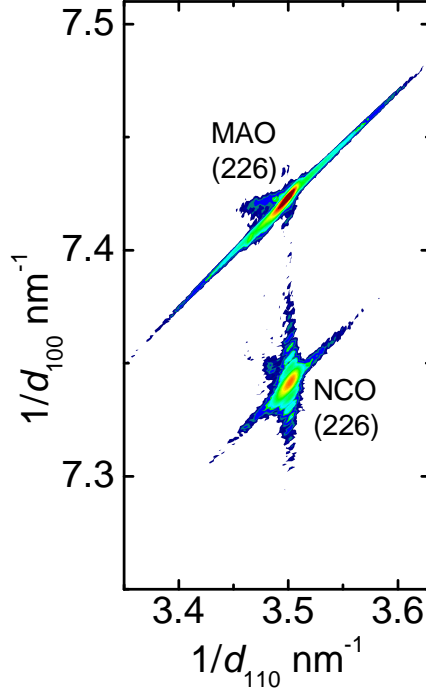


Figure 3.6: (226) RSM scan of the  $\text{NiCo}_2\text{O}_4 \parallel \text{MgAl}_2\text{O}_4$  (001)

calculated from the scan and used to compute thickness of the film  $t_F$  as,

$$t_F = \frac{2\pi}{\Delta q} \quad (3.1)$$

### 3.3 Magnetism Measurement

We measured the magnetic properties these films using commercial Superconducting Quantum Interference Device (SQUID), which has the sensitivity of  $10^{-8}$  emu. In principle, SQUID is basically two parallel connected Josephson junctions connected to form a ring as shown in figure. The Josephson junction consists of two superconductors separated by a thin insulating layer as shown in fig. 3.8(a). Cooper pairs can tunnel through the insulating barrier. If the voltage drop  $V$  across the

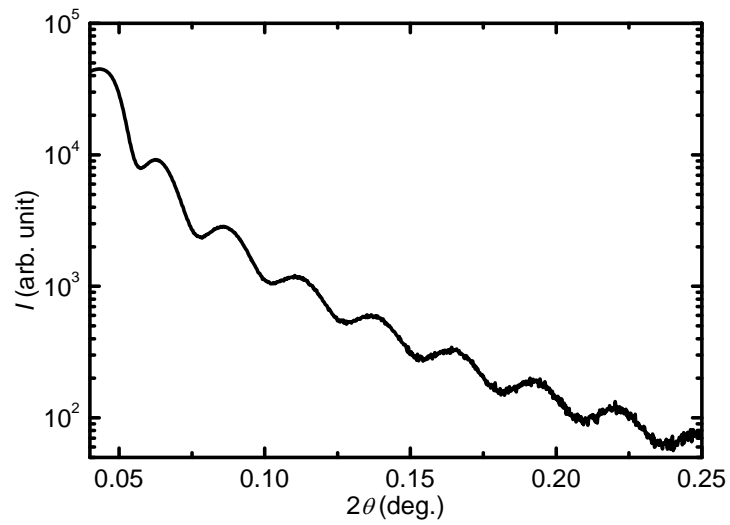


Figure 3.7: Thickness scan of 24 nm thick  $\text{NiCo}_2\text{O}_4$  film

junction is zero, the current density is given by,

$$J = J_0 \sin \delta \quad (3.2)$$

where  $\delta$  is the phase difference between cooper pairs on each side of the junction. Therefore a dc current through the junction is produced without any voltage drop. Such effect is known as the dc Josephson effect.

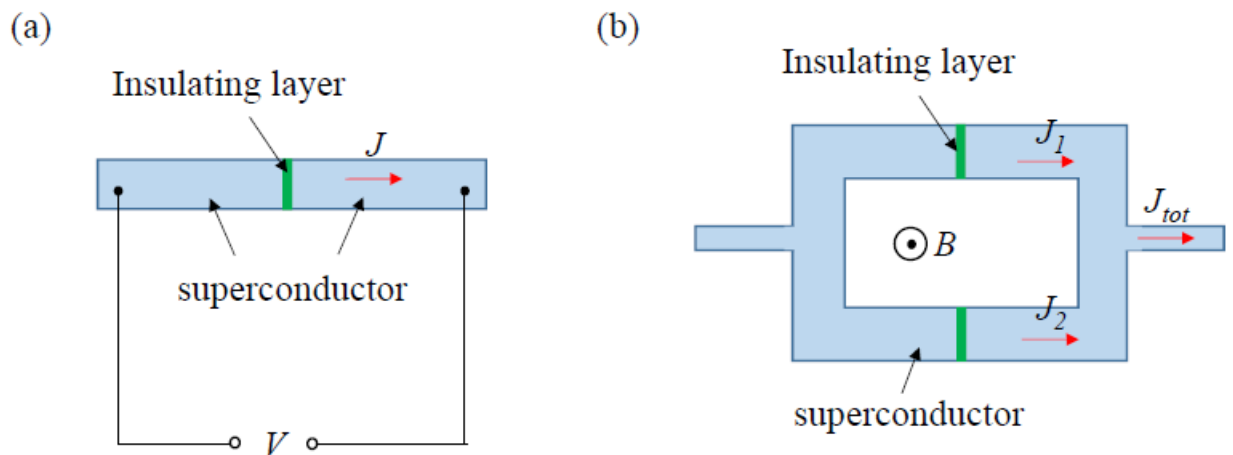


Figure 3.8: The schematic of Josephson junction (a), SQUID (b)

When the two Josephson junctions are connected in parallel to form a ring as shown in fig.(b), the current from each junction interferes with the current from each other junction, leading to a resultant current  $J_{Tot}$  varying with the phase difference of  $J_1$  and  $J_2$ . When an external magnetic flux is coupled into the Josephson loop, the voltage drop across the Josephson junction will change.  $J_{Tot}$  is then modulated by the given magnetic flux through the ring area,

$$J_{Tot} = \sin\delta_0 \cos\left(\frac{q}{h}\phi\right) \quad (3.3)$$

where  $\delta_0$  is constant the phase factor. Monitoring the change in voltage allows determination of the magnetic flux that has been coupled into the SQUID loop.

### 3.4 Resistivity Measurement

The resistance of the samples are measured using the standard four-probe method with a Physical Properties Measurement System (PPMS), which provides a constant current flow  $I$  and measures the voltage drop  $V$  across the sample. The resistance of the sample is given by Ohm's law:

$$R = \frac{V}{I} \quad (3.4)$$

As shown in fig. (3.9), two outer probes are used for sourcing current and the two inner probes are used to measure the voltage drop across the sample surface. The measurement of current through the sample is precise since only a negligible proportion of current flows through the voltmeter branch due to the high resistance of voltmeter. Whereas in two-probe method, both current and voltage meter, share common electrical leads and the measured resistance is affected by the contact resistance of the measuring leads. If the separation between voltage leads is  $L$ , and the

cross section of current flow  $S$ , the resistivity of the sample can be given by

$$\rho = \frac{RL}{S} \quad (3.5)$$

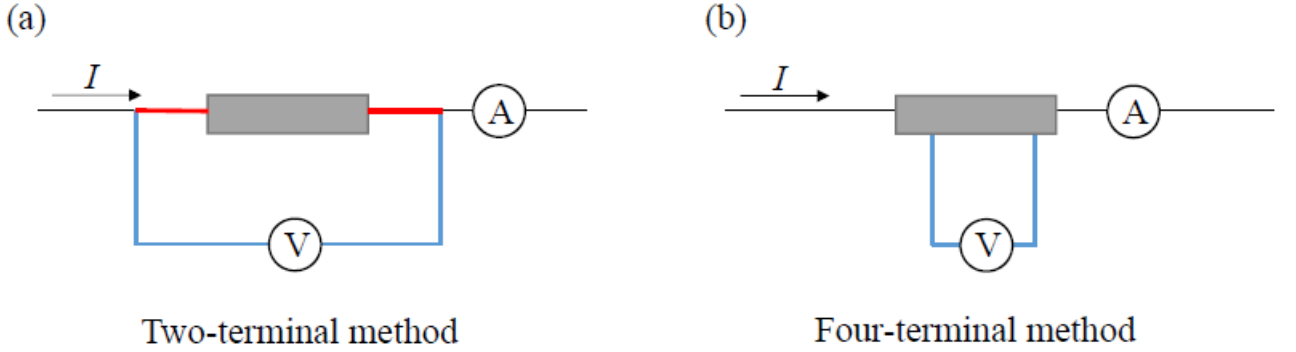


Figure 3.9: The schematics of resistance measurements with (a) two probe and (b) four probe method

### 3.5 Hall Effect Measurement

The basic physical principle underlying the Hall effect is the Lorentz force. When an electric current flows through a conductor in a magnetic field, the magnetic field exerts a transverse force on the moving charge carriers which tends to push them to one side of the conductor. The build up of charge at the sides of the conductors will balance this magnetic influence, producing a measurable voltage between the two sides of the conductor. This measurable transverse voltage is called Hall effect. The schematic representation of Hall effect on a conductor is shown in Fig. 3.10(a). A magnetic field  $B_z$  is applied perpendicular to the current direction  $J_{xx}$ , as a consequence, an electric field  $E_{xy}$  develops in  $y$  direction.

For a metal with only one type of charge carrier (electron or hole), the current density  $J_{xx}$  is

$$J_{xx} = nqv \quad (3.6)$$



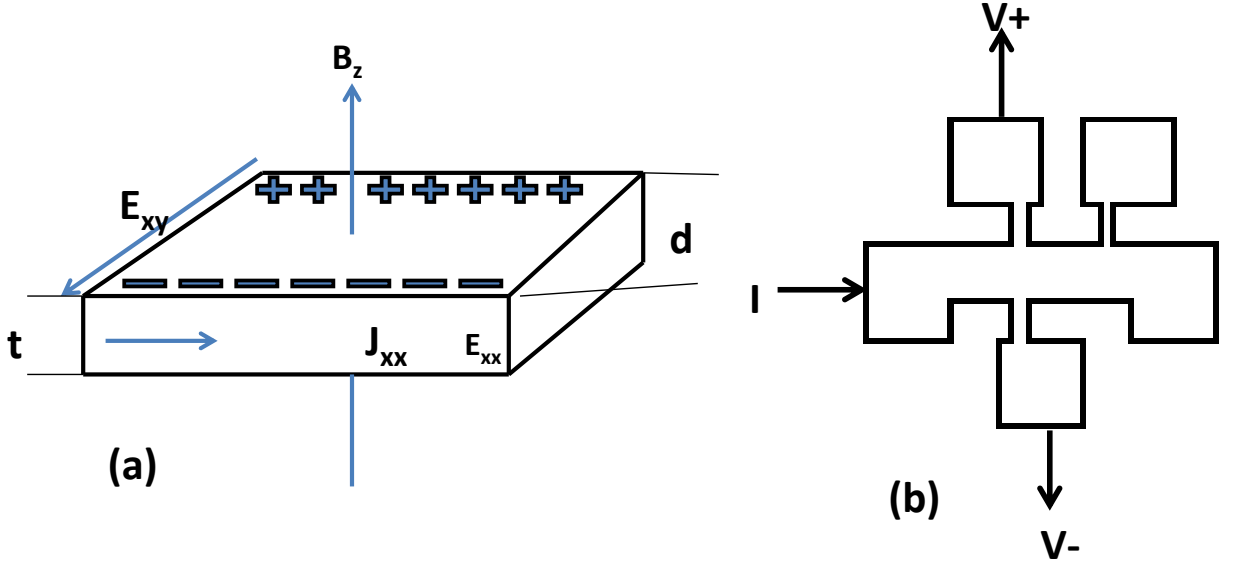


Figure 3.10: The mechanism of Hall effect (a), the Hall effect measurement with four terminal configuration (b)

where  $n$  is the charge carrier density and  $v$  is the velocity of charge.

In equilibrium condition, the Lorentz force and the force from the transverse electric field ( $E_{xy}$ ) must be equal and opposite. Hence

$$qB_z v = qE_{xy} \quad (3.7)$$

The Hall coefficient  $R_H$  is defined as,

$$R_H = \frac{E_{xy}}{J_{xx} B_z} \quad (3.8)$$

Therefore, for a simple metal,

$$R_H = \frac{1}{nq} \quad (3.9)$$

In practice, the directly measured physical quantity is transverse voltage or Hall

voltage ( $V_H$ ). For a sample of width  $d$  and thickness  $t$ ,  $V_H$  is

$$V_H = E_{xy}d = vB_zd \quad (3.10)$$

The Hall resistance  $\rho_H$  or  $\rho_{xy}$  is;

$$\rho_H = \frac{V_H}{I_{xx}} = \frac{V_H}{J_{xx}td} \quad (3.11)$$

Finally, the Hall coefficient is obtained by;

$$R_H = \frac{\rho_H}{B} = \frac{1}{nq} \quad (3.12)$$

Since the value of Hall coefficient  $R_H$  is obtained by measuring the transverse voltage  $V_H$ , the voltage lead must be precisely symmetric to avoid the possible longitudinal voltage component, which is very difficult in practice. Therefore we photo lithographically patterned the Hall bars as shown in Fig. 3.10(b) using contact photo lithography and etched away the excessive film outside the pattern using plasma etching.

## Chapter 4

# Effect of Growth Temperature on the Physical Properties of $\text{NiCo}_2\text{O}_4$

Since most of the studies done are focused on poly- or nano-crystalline samples of  $\text{NiCo}_2\text{O}_4$ , the reported electrical properties are severely influenced by crystalline disorders. To investigate the intrinsic electrical ground state of  $\text{NiCo}_2\text{O}_4$ , epitaxial thin films with high crystalline quality are required. Furthermore, high quality epitaxial  $\text{NiCo}_2\text{O}_4$  films with the ferrimagnetic order and low resistivity can be utilized for applications in spintronics.  $\text{NiCo}_2\text{O}_4$  is believed to exhibit an inverse spinel structure with Ni cations occupying the octahedral sites while Co cations are evenly distributed to both the octahedral and tetrahedral sites.[64, 66] However, Ni ions can diffuse into the tetrahedral sites substituting Co, which is reported to cause changes in lattice constants and magnetic moments.[2, 66, 17]  $\text{NiCo}_2\text{O}_4$  is also known to have ferrimagnetic order with magnetization of  $1.7\mu_B$  per formula unit under a field of 10 T at 4K.[2, 66] Marco *et al.* reported that the delocalized electron distribution in the octahedral sites with average oxidation states of +3.5 and +2.5 for Ni and Co, respectively, while the tetrahedral site is occupied with +2 Co cations. They also suggested a possible charge redistribution within the octahedral sites under applied magnetic field leading to spontaneous magnetic moments ranging from 0 to  $2\mu_B$ . [2]

However, the exact valence states are still unclear due to the structural disorders in the poly-crystalline films. In this research, we report the growth of highly crystalline spinel  $\text{NiCo}_2\text{O}_4$  thin films on  $\text{MgAl}_2\text{O}_4$  (001) single crystal substrates, and the observation of the metallic conduction.

We have grown epitaxial thin films of spinel  $\text{NiCo}_2\text{O}_4$  on single crystalline  $\text{MgAl}_2\text{O}_4$  (001) substrates by pulsed laser deposition. Magnetization measurement revealed hysteresis loops consistent with the reported ferrimagnetic order. The electrical transport exhibits a metallic behavior with the lowest resistivity of  $0.8 \text{ m}\Omega \text{ cm}$  and a metal insulator transition around the Neel temperature. The systematic variation in the properties of the films grown at different growth temperatures indicates a close relationship between the magnetic order and electrical transport.

## 4.1 Experimental Methods

We report the growth of highly crystalline spinel  $\text{NiCo}_2\text{O}_4$  thin films on  $\text{MgAl}_2\text{O}_4$  (001) single crystal substrates, and the observation of the metallic conduction. Epitaxial films of spinel  $\text{NiCo}_2\text{O}_4$  were grown on spinel  $\text{MgAl}_2\text{O}_4$  substrates by using a custom built pulsed laser deposition system.[99] The films were grown at growth temperature ( $T_{\text{sub}}$ ) ranging from  $200^\circ\text{C}$  to  $600^\circ\text{C}$  under 50 mTorr of  $\text{O}_2$ . A polycrystalline  $\text{NiCo}_2\text{O}_4$  target produced by solid state reaction was ablated by a KrF excimer laser ( $\lambda = 248\text{nm}$ ) at 10 Hz with a fluence of  $2.5 \text{ J/cm}^2$ . The thicknesses of the films were controlled to be about 240 nm. The structural and magnetic properties of the films were measured using a four-circle high-resolution X-ray diffraction (HR-XRD) system and a superconducting quantum interference device (SQUID) magnetometer, respectively. The resistivity of the samples was measured using a standard 4-probe method with a Physical Property Measurement System (PPMS).

## 4.2 Structural Results

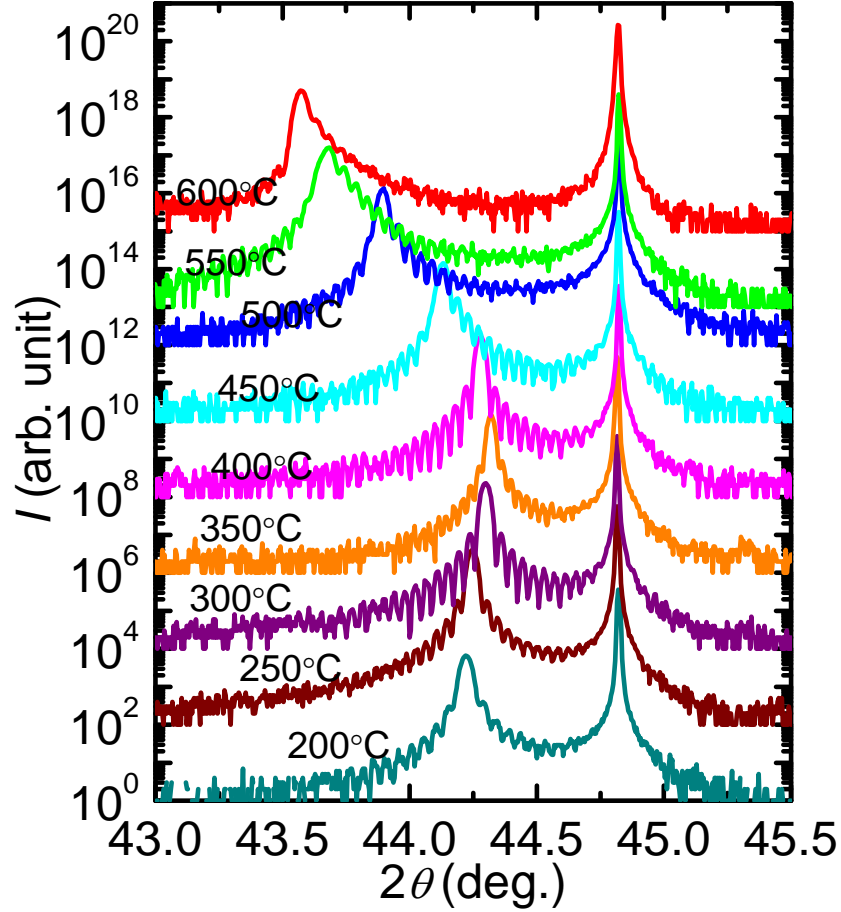


Figure 4.1: HR-XRD  $2\theta - \theta$  scan of the films grown at temperature ranging from 200°C-600°C showing the decrease in film peak position increasing the growth temperature.

The epitaxial growth of  $\text{NiCo}_2\text{O}_4$  films on  $\text{MgAl}_2\text{O}_4$  (001) substrates is demonstrated by HR-XRD measurements. Figure 4.1 shows the XRD  $2\theta - \theta$  scan of the films grown at temperature ranging from 200°C-600°C. The film peak shifts to lower angle increasing the growth temperature indicating the increase in out-of-plane lattice constant.

Figure 4.2 is for a representative  $\text{NiCo}_2\text{O}_4$  film grown at 350°C. The strong peaks of (001) reflections in the  $2\theta - \theta$  scan shown in Fig. 4.2 confirm the high

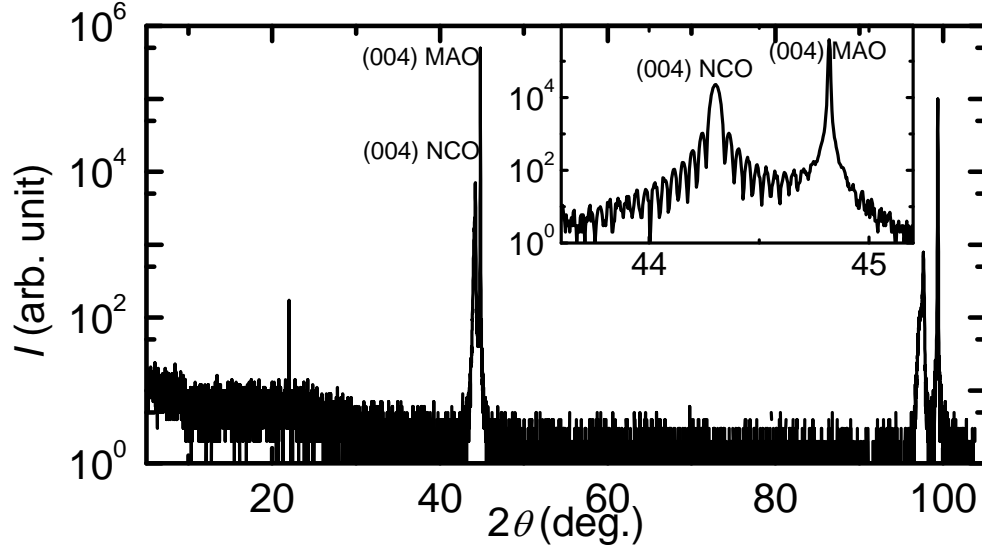


Figure 4.2: HR-XRD  $2\theta - \theta$  scan of a 240nm thick  $\text{NiCo}_2\text{O}_4$  film grown at  $350^\circ\text{C}$  on  $\text{MgAl}_2\text{O}_4$  (001) substrate. The inset shows a detailed spectrum around the (004) reflections of the substrate and the film.

crystallization quality of the films with c-orientation without any secondary phases. The clear interference pattern around the  $\text{NiCo}_2\text{O}_4$  (004) reflection seen in the inset of Fig. 4.2 indicates the presence of long range structural order and a smooth film surface. All the films grown at various  $T_{\text{sub}}$ 's show distinctive oscillations from which the thicknesses are calculated. The rocking curves of the  $\text{NiCo}_2\text{O}_4$  (004) peaks show full width at half maximums (FWHM's) ranging from 14.4 to 28.8 arc sec which are similar to that of the  $\text{MgAl}_2\text{O}_4$  substrate (13.68 arc sec). The extremely small mosaic spreads of the films are comparable to those of high quality  $\text{SrTiO}_3$  films grown on  $\text{DyScO}_3$  substrates.[101] The HR-XRD results suggest superb crystalline qualities of the  $\text{NiCo}_2\text{O}_4$  films with very low density of defects.

Figs. 4.4 shows the  $\phi$  scans of the  $\text{NiCo}_2\text{O}_4$  (404) and the  $\text{MgAl}_2\text{O}_4$  (404) reflections, respectively, from the film grown at  $350^\circ\text{C}$ . The 4-fold symmetry from  $\text{NiCo}_2\text{O}_4$  (404) confirms the epitaxial growth with  $\text{NiCo}_2\text{O}_4$  [100]  $\parallel$   $\text{MgAl}_2\text{O}_4$  [100] and  $\text{NiCo}_2\text{O}_4$  (001)  $\parallel$   $\text{MgAl}_2\text{O}_4$  (001). The same epitaxial relation was observed for all the films grown at different  $T_{\text{sub}}$ 's. It is noteworthy that even the film grown at

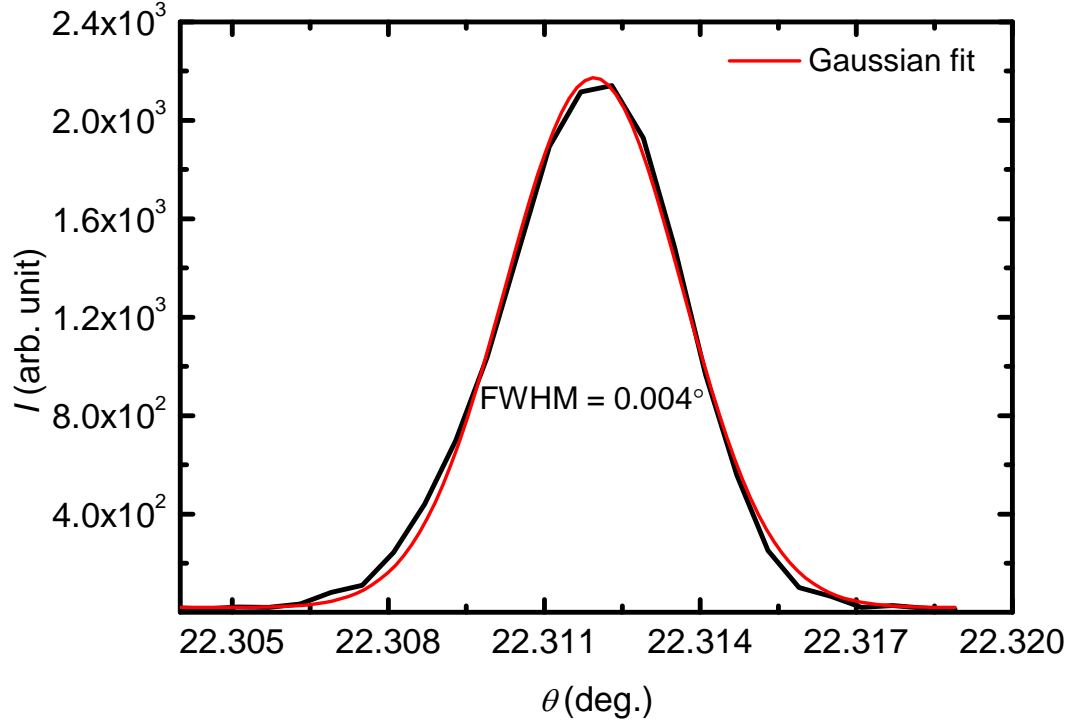


Figure 4.3: (004) rocking curve of the  $\text{NiCo}_2\text{O}_4$  film grown at  $350^\circ\text{C}$ . The FWHM is  $0.004^\circ$  which is similar to the FWHM value of  $\text{MgAl}_2\text{O}_4$  indicating the high crystalline quality of the  $\text{NiCo}_2\text{O}_4$  film.

$250^\circ\text{C}$  exhibits high quality epitaxy displaying sharp reflection peaks with significant oscillations.

Figs. 4.5(a), 4.5(b), and 4.5(c) show the HR-XRD reciprocal space maps (RSM's) around the  $\text{NiCo}_2\text{O}_4$  and  $\text{MgAl}_2\text{O}_4$  (226) reflections of the films grown at  $250$ ,  $350$ , and  $450^\circ\text{C}$ , respectively. The clear sharp single peak of the film directly below the substrate peak indicates high crystalline quality with a tetragonal symmetry. In all three films, the positions of the  $\text{NiCo}_2\text{O}_4$  (226) peaks exactly coincide with those of  $\text{MgAl}_2\text{O}_4$  (226) along the horizontal axis indicating the in-plane lattice constant of the films are identical to that of the substrate ( $a = 8.083 \text{ \AA}$ ). The out-of-plane lattice constants calculated from the vertical position of the peaks for the films grown at  $250$ ,  $350$ , and  $450^\circ\text{C}$  are  $8.178$ ,  $8.173$ , and  $8.200 \text{ \AA}$ , respectively. They are larger than the bulk value ( $a = 8.116 \text{ \AA}$ ) due to the compressive in-plane strain from the substrate.

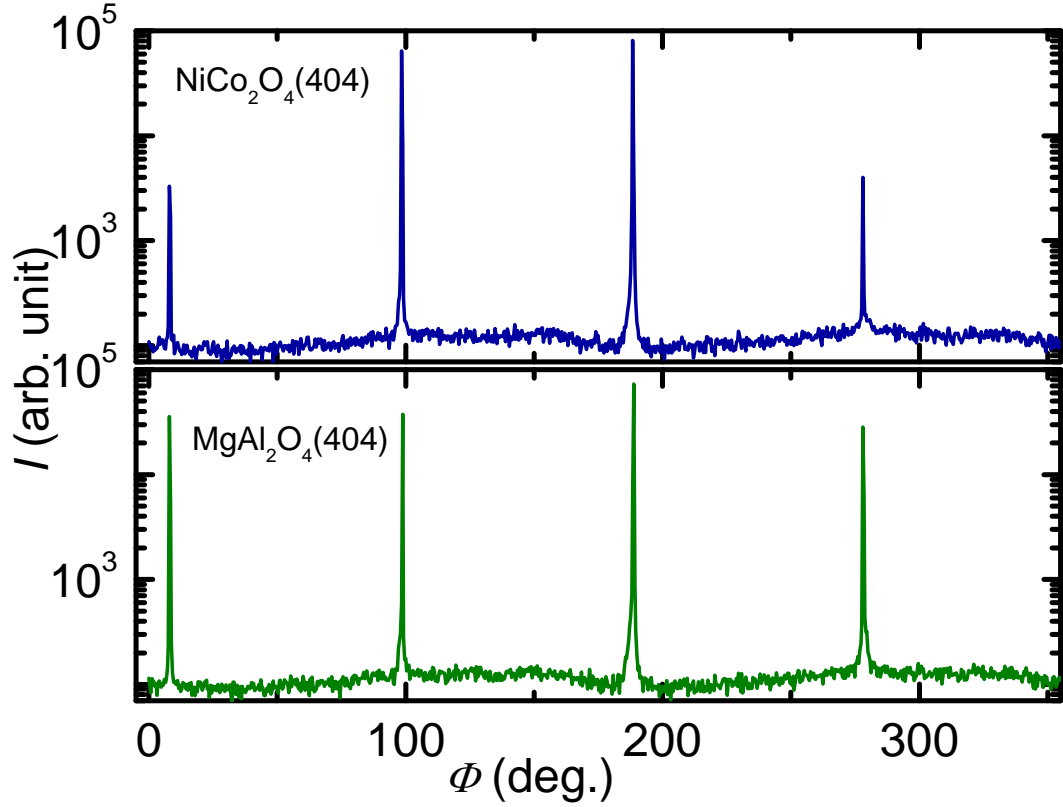


Figure 4.4:  $\phi$  scans of the  $\text{NiCo}_2\text{O}_4$  (404) and  $\text{MgAl}_2\text{O}_4$  (404) reflections, respectively.

The change in the out-of-plane lattices with a fixed in-plane lattice indicates a variation in the unit cell volume with different  $T_{\text{sub}}$ 's. One of the possible origins for such a variation is formations of oxygen or cation vacancies. However, the low  $T_{\text{sub}}$  with fixed oxygen pressure and the non-monotonic change in  $c$  make these explanations unlikely. Also film grown at different oxygen pressure did not show change in lattice. The reason for the change in the unit cell volume can be found in the inverse spinel structure of  $\text{NiCo}_2\text{O}_4$ . When a Ni cation moves into a tetrahedral site, the unit cell volume changes due to the difference in ionic sizes between Ni and Co.[17] The change in thermodynamics at different  $T_{\text{sub}}$ 's may induce changes in occupations of Ni and Co into tetrahedral and octahedral sites leading to the change in the lattice constants.



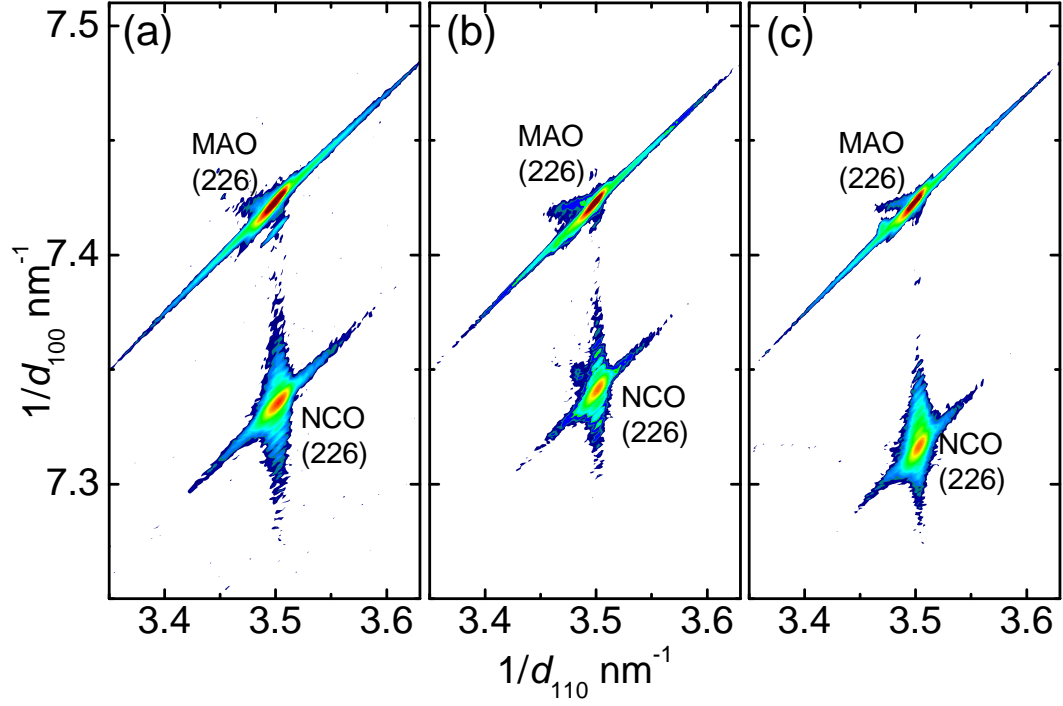


Figure 4.5: HR-XRD RSMs around the (226) reflections of the  $\text{NiCo}_2\text{O}_4$  films on  $\text{MgAl}_2\text{O}_4$  substrates grown at (a) 250, (b) 350, and (c) 450°C.

### 4.3 Magnetic Results

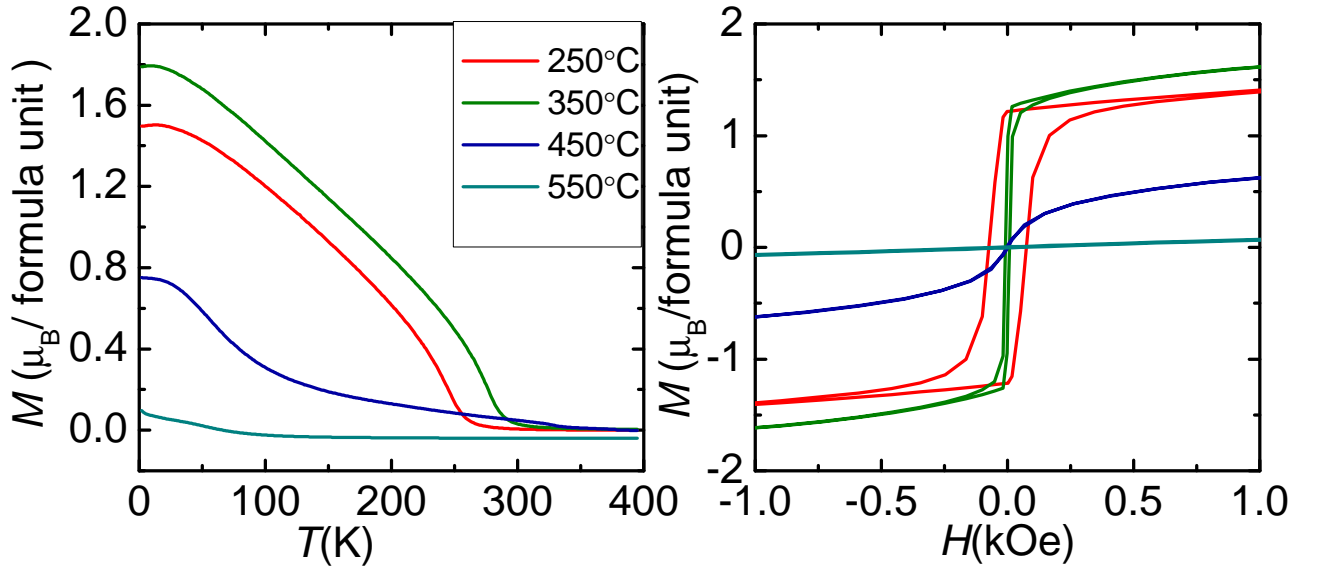


Figure 4.6: Magnetization  $M$  vs. temperature  $T$  for the  $\text{NiCo}_2\text{O}_4$  films on  $\text{MgAl}_2\text{O}_4$  (001) substrates grown at 250, 350, 450, and 550°C. (b)  $M$  vs. magnetic field  $H$  for the same set of films.

Results of temperature-dependent magnetization measured at 0.2 T [Fig. 4.6)] show strong magnetic order below 265 K and 289 K for the  $\text{NiCo}_2\text{O}_4$  film grown at 250 (red solid line) and 350°C (green solid line), respectively. The diamagnetic contribution from the substrate to the total magnetization has been subtracted out with a separate measurement. Figure 4.6(b) shows the  $M$  vs. magnetic field  $H$  curves at 10 K of the films grown at different  $T_{\text{sub}}$ 's. The hysteresis loops with non-zero remnant magnetization are consistent with the ferrimagnetic order previously confirmed with neutron diffraction.[2] The film grown at 350°C shows the stronger magnetization with a coercive field of 8.58 Oe, and a saturation magnetization  $M_s$  of  $1.87 \mu_B$ /formula unit, which is larger than the previously reported values of  $1.71 \mu_B$  at 10 T,[2]  $1.25 \mu_B$  at 0.8 T,[66] and  $1.51 \mu_B$  at 0.8 T.[80] The Neel temperature ( $T_N$ ) and  $M_s$  shows a modest increase as  $T_{\text{sub}}$  increases from 250 to 350°C. A further increase in  $T_{\text{sub}}$  to 450, then 550°C, however, results in rapid decrease in  $T_N$  and  $M_s$ . These changes can be explained by the distribution of Ni and Co cations in the tetrahedral and octahedral sites as well as their valences.[2, 19] With ferrimagnetic order, the moments from uncompensated spins from the tetrahedral sites mostly occupied by Co, order antiparallel with uncompensated spins from the octahedral sites evenly occupied by Co as well as Ni. The magnetic contribution from the octahedral Co is considered to be minimal. The difference between antiparallel magnetic moments from tetrahedral Co and octahedral Ni makes up the total magnetization of  $\text{NiCo}_2\text{O}_4$ . For accurate analysis to match the observed magnetization to exact valences of Ni and Co, site and element specific x-ray absorption measurements, such as x-ray absorption spectroscopy, x-ray magnetic circular dichroism, and electron energy loss spectroscopy are necessary.

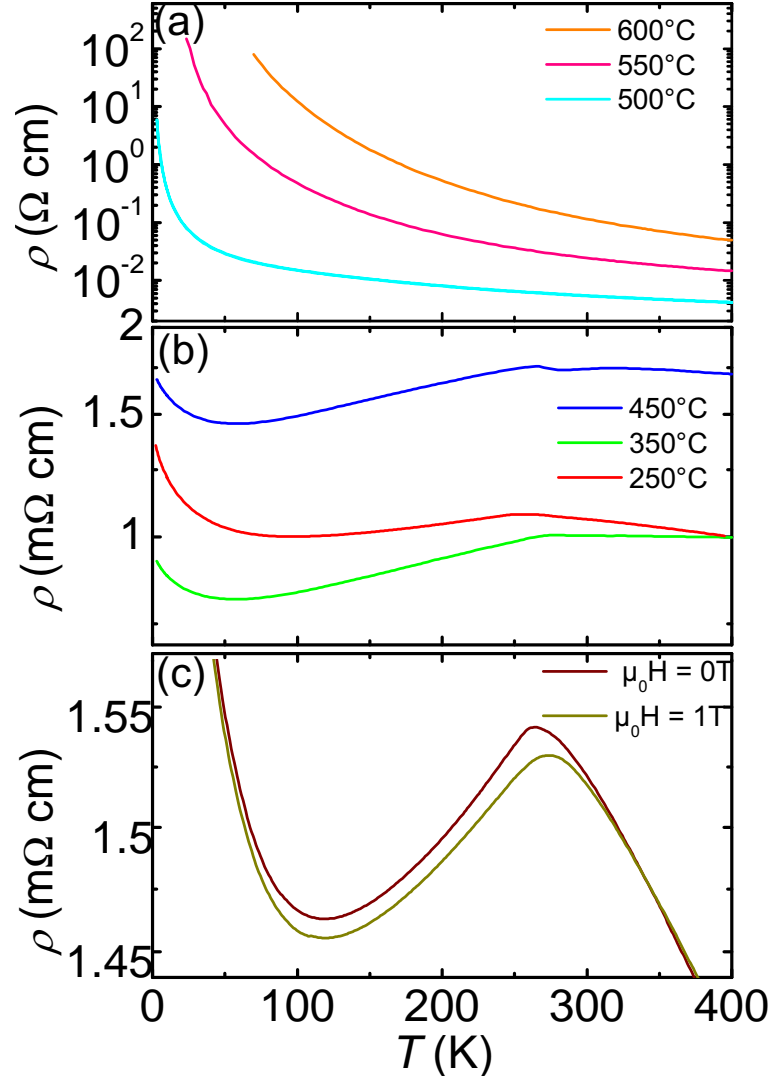


Figure 4.7: (a) In-plane resistivity  $\rho$  vs. temperature  $T$  for the  $\text{NiCo}_2\text{O}_4$  films on  $\text{MgAl}_2\text{O}_4$  (001) substrates grown at 500, 550, and 600°C, showing insulating behavior. (b)  $\rho$  vs.  $T$  for the  $\text{NiCo}_2\text{O}_4$  films on  $\text{MgAl}_2\text{O}_4$  (001) substrates grown at 250, 350, and 450°C, showing metallic behavior. (c)  $\rho$  vs.  $T$  for the 450 °C film measured under magnetic field of 0 and 1 T exhibiting a negative magnetoresistance of 2% with the application of magnetic field 1 T.

## 4.4 Transport Properties

The change in  $T_{\text{sub}}$  plays a significant role on the electrical transport of the epitaxial  $\text{NiCo}_2\text{O}_4$  films. The films grown at  $T_{\text{sub}}$ 's above 500°C show insulating behavior as shown in Fig. 4.7(a). The resistivity value of the film with  $T_{\text{sub}} = 500^\circ\text{C}$

at the room temperature is very similar to the previously reported values.[102] Surprisingly, the films grown at  $T_{\text{sub}}$ 's lower than 450°C show metal-insulator transitions around  $T_N$  with metallic electrical transport down to about 50 K as shown in Fig. 4.7(b). The slight upturn at lower temperatures are likely due to a localization of charge carriers. Especially, the film grown at 350°C exhibits the lowest resistivity of 0.8 m $\Omega$  cm around 50 K which is much smaller than the lowest reported value of 3 m $\Omega$  cm for the sputtered deposited polycrystalline films.[17] The epitaxial films of NiCo<sub>2</sub>O<sub>4</sub> exhibit a remarkable coexistence of metallic transport and ferrimagnetism. The concomitant magnetic and metal-insulator transitions is similar to mixed-valence perovskite manganites that exhibit large negative magnetoresistance.[103] Indeed, the resistivity of NiCo<sub>2</sub>O<sub>4</sub> decreases under strong magnetic field as seen in Fig 4.7(c) for the 450°C grown film. The film exhibits about -2% magnetoresistance under magnetic field of 1 T with slight increase in  $T_N$ .

## 4.5 Discussion

An insight into the origin of the metallic transport as well as the very wide change of the resistivity with varying  $T_{\text{sub}}$  can be obtained by comparing the changes in the conduction and the magnetization. As shown in Fig. 4.8(a), the saturation magnetization,  $M_s$  maintains a more or less constant value up to  $T_{\text{sub}}$  400°C, then quickly decreases with further increase in  $T_{\text{sub}}$ . A significant similarity can be found in the  $T_{\text{sub}}$  dependency of the room temperature resistivity ( $\rho_{300K}$ ) and the out-of-plane lattice constant ( $c$ ).  $\rho_{300K}$  and  $c$  exhibit little change up to  $T_{\text{sub}} = 400^\circ\text{C}$ , then increase with further increase in  $T_{\text{sub}}$  as seen in Fig. 4.8(b) and 4.8(c), respectively. The common set temperature of the rapid variation in  $M_s$ ,  $\rho_{300K}$ , and  $c$  suggests a very close relation between the magnetic order, electrical transport, and structure of NiCo<sub>2</sub>O<sub>4</sub>. Furthermore, the intriguing coexistence of the metallic transport and the

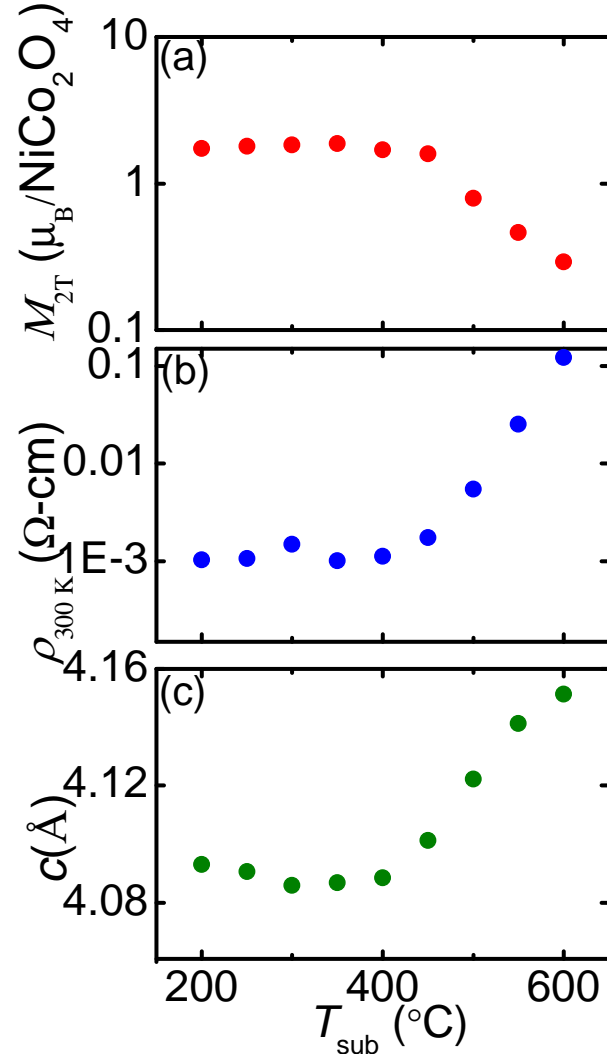


Figure 4.8: (a) Magnetization at 2 T vs. growth temperature  $T_{\text{sub}}$ , (b) resistivity at the room-temperature  $\rho_{300\text{ K}}$  vs.  $T_{\text{sub}}$ , and (c) out of plane lattice constants  $c$  vs.  $T_{\text{sub}}$  for all the  $\text{NiCo}_2\text{O}_4$  films on  $\text{MgAl}_2\text{O}_4$  (001) substrates.

ferrimagnetic order provides a good possibility of a strong spin polarization depending on the exact electronic structure of Co and Ni cations at tetrahedral and octahedral sites. The detailed description of the valences and distribution of the cations in the lattice sites is a matter of controversy.[28, 2, 104] For comprehensive understanding of the Ni and Co distribution in octahedral and tetrahedral sites, detailed spectroscopic measurements are necessary.

## 4.6 Summary and Conclusion

In summary, we have grown epitaxial spinel  $\text{NiCo}_2\text{O}_4$  on  $\text{MgAl}_2\text{O}_4$  (001) substrates at different growth temperature and studied their structural, electrical and magnetic properties. Metallic behavior has not been observed in  $\text{NiCo}_2\text{O}_4$  but in other spinels. For the first time, we have observed metallic conduction with a robust ferrimagnetic order in epitaxial thin films of spinel  $\text{NiCo}_2\text{O}_4$  on  $\text{MgAl}_2\text{O}_4$  substrates. A metal-insulator transition is also observed near the Neel temperature. The film grown at  $350^\circ\text{C}$  shows smaller lattice constant, lower resistivity and stronger magnetization indicating the most structurally ordered distribution of Ni and Co ions. Varying the growth temperature resulted in systematic change in lattice constant, resistivity, and magnetization. A systematic investigation of films grown at various temperatures suggests a strong correlation between the structural, magnetic, and electrical transport properties as shown in Fig. 4.8. The large spontaneous magnetization from the ferrimagnetic spinel  $\text{NiCo}_2\text{O}_4$  with very low resistivity will be very useful for spintronic applications.

## Chapter 5

# Effect of Thickness on the Physical Properties

### 5.1 Introduction

Magnetic spinel films, such as  $\text{NiFe}_2\text{O}_4$  and  $\text{CoFe}_2\text{O}_4$  ferrites, have been widely investigated due to their robust magnetic properties with the potential for spin injection and/or filtering applications in spintronics.[105, 10, 11, 12, 13, 106, 107, 108] The attraction of the ferrites is that they retain and even enhance[105, 106, 108] their magnetism in ultrathin few-unit-cell films; their disadvantage is that they are semiconductors and need to be doped[108] to conduct electric current. The spinel  $\text{NiCo}_2\text{O}_4$  has long been known to possess ferrimagnetic order and the possibility of band-like p-type conduction has been suggested for the material.[2, 19, 109] Here, we show that ultrathin epitaxial  $\text{NiCo}_2\text{O}_4$  films remain magnetic and metallic down to the thickness of 3 unit cells (uc). These newly observed excellent properties may open the door for the use of  $\text{NiCo}_2\text{O}_4$  in spintronics devices as storage or a spin-injection/filtering medium.

Historically, the spinel  $\text{NiCo}_2\text{O}_4$  has been studied for its remarkable optical, electrical, and catalytic properties for various technological purposes including fuel

cell electrodes, oxygen catalysis, reduction in alkaline media, water electrolysis, and for sensors and flat panel displays as a transparent conducting oxide.[109, 110, 15, 111] The material is prepared most often in the form of polycrystalline particulate samples with a rather low packing density or in the form of polycrystalline thin films[5], which makes it difficult to characterize its intrinsic properties.[109, 5] In the previous section, we discussed the synthesis of high-quality epitaxial  $\text{NiCo}_2\text{O}_4$  films using pulsed laser deposition (PLD) method. The films grown at temperatures of 300 - 400°C show metallic behavior accompanied with ferrimagnetic order with the Curie temperature  $T_c \sim 300$  K, while increasing the growth temperature above 500°C tunes the conductivity of the films from metallic to insulating and renders the films non-magnetic[82] The magnetic properties of  $\text{NiCo}_2\text{O}_4$  have not been used in applications but have been investigated in the context of the mixed valencies of the Ni and Co cations in this inverse spinel, where the Ni cations occupy almost exclusively the octahedral sites and the Co cations are distributed evenly between the tetrahedral and octahedral sites.[19, 2] Various models have been proposed that put the cation oxidation states in the (2.5-3)+ and (2.5-3.5)+ range for the octahedral Co and Ni, respectively.[19, 2] In applied magnetic field, the mixed-valence cationic character leads to a redistribution of charge and a modification of the oxidation states and of the spontaneous magnetic moment. In our  $\text{NiCo}_2\text{O}_4$  films grown at 350°C, we reported a field-dependent spontaneous magnetization of  $1.87 \mu_B$  per formula unit in the field 2 T, consistent with previous reports.[19, 2] The transport and magnetic properties of thin films depend strongly on their thickness at the ultrathin level. As the thickness becomes smaller, such observables as the resistivity, saturation magnetization, and coercive field can be influenced to a high degree by the films geometrical boundaries, interfacial scattering and pinning, and the crossover from three-dimensional to two-dimensional physics.[68, 69, 70] A thorough understanding of a materials behavior



as the function of film thickness is indispensable before it can be integrated in technological applications. We have investigated the evolution of the resistivity and the magnetic properties of  $\text{NiCo}_2\text{O}_4$  in films down to 1 uc in thickness and found enhanced coercivity in films below 30 uc. The films of 2 uc and less become highly resistive and lose the long-range magnetic order, and we regard 2 uc as the thickness of the electric and magnetic dead layers. All films thicker than the dead layer displayed metallic behavior below room temperature with a low-temperature resistivity minimum at  $T_{\min} \sim 50\text{-}60$  K. The analysis of the temperature dependence of the resistivity below  $T_{\min}$  points to the dominant role of quantum interference effects in the transport in  $\text{NiCo}_2\text{O}_4$  at low temperatures and in the ultrathin regime.

## 5.2 Experimental Methods

$\text{NiCo}_2\text{O}_4$  films of thickness ranging from 1 uc to 228 uc (1 uc = 0.8114 nm) were grown epitaxially on  $\text{MgAl}_2\text{O}_4$  (001) substrates by PLD at the constant substrate temperature of 350°C and the 50 mTorr  $\text{O}_2$  pressure inside the chamber. The structural properties were analyzed using four circle high resolution X-ray diffraction (HR-XRD) while the thicknesses of the films were determined by the x-ray reflectivity (XRR) measurement. The magnetic properties of the films were measured using a superconducting quantum interference device (SQUID) magnetometer. The resistivity was measured using the standard 4-probe method and the Hall resistivity was measured with magnetic field applied perpendicular to the film surface. Using the conventional photolithography and Ar ion milling, appropriate current and voltage leads were patterned on the films for the measurements of longitudinal and transverse resistivity.

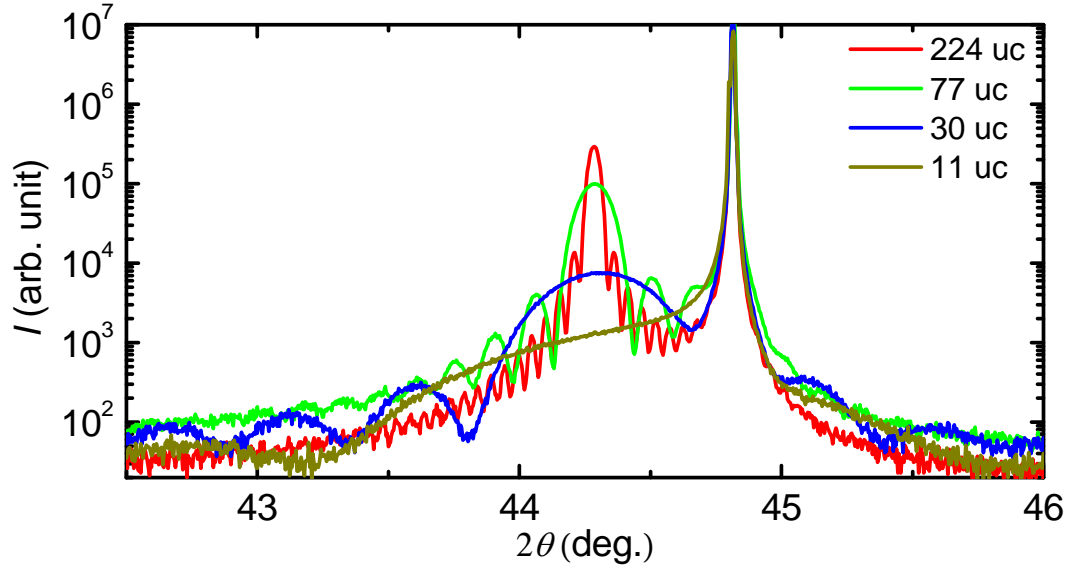


Figure 5.1: HR-XRD  $2\theta$ - $\theta$  scans of  $\text{NiCo}_2\text{O}_4$  films on  $\text{MgAl}_2\text{O}_4$  (001) substrate with the thicknesses of 11, 30, 77, and 224 unit cells. The film peak position remains at the same value of  $2\theta$ , indicating constant out-of-plane lattice value changing the film's thickness.

### 5.3 Structural Properties

Figure 5.1 shows XRD  $2\theta$ - $\theta$  scans through the (004) symmetric reflections of the film and substrate for the 11, 30, 77, and 224 uc thick films, respectively. The intensity of the film peaks increases significantly as the thickness increases, but the peak position remains at the same value of  $2\theta$ , indicating constant out-of-plane lattice value. Figures 5.2(a), (b), and (c) show the reciprocal space mapping (RSM) scans around the (226) reflection of the films with thickness 11, 225, and 875 uc. The horizontal and vertical peak positions for all the films are the same, indicating identical lattice parameters and the strain state independent of the films thickness. The vertical position of the film peak is also identical to that of the substrate, showing that the films are fully strained up to the highest thickness (875 uc, 700 nm). The in- and out-of-plane lattice constants calculated from the x and y positions of the film peak are 8.076 Å and 8.173 Å respectively. The smaller in-plane and the larger out-

of-plane lattice constant that of the bulk, indicates compressive in-plane strain. We observed that films up to 875 uc (700 nm) are still fully strained, which is due to the smaller lattice mismatch between the film and the substrate and the high crystalline quality of the films.

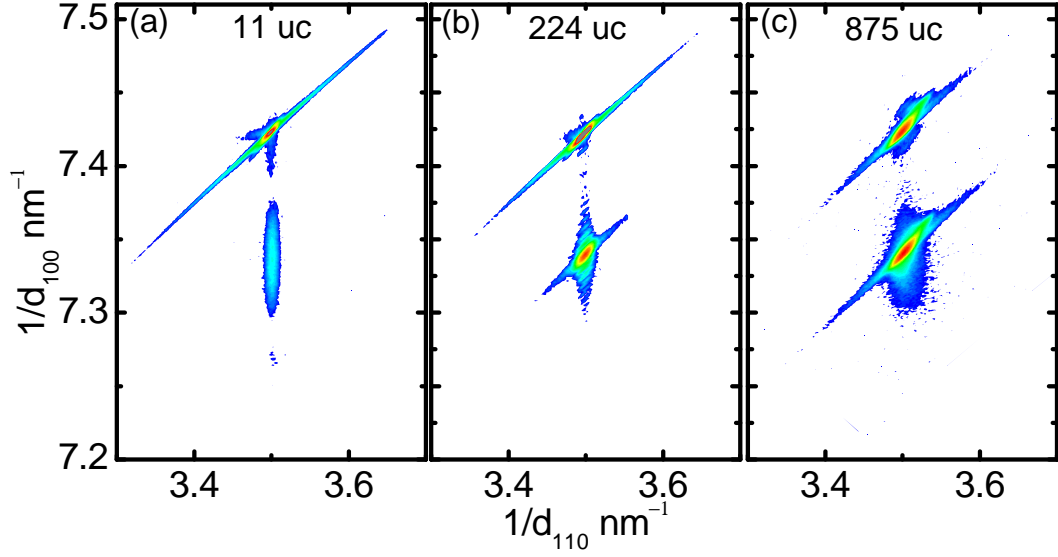


Figure 5.2: (a), (b), and (c) HR-XRD reciprocal space maps around the (226) reflections of the  $\text{NiCo}_2\text{O}_4$  films on  $\text{MgAl}_2\text{O}_4$  substrate with the thickness 11, 224, and 875 unit cells, respectively. The horizontal and vertical peak positions for all the films are the same, indicating identical lattice parameters and the strain state independent of the films thickness.

## 5.4 Transport Properties

Figure 5.3 shows the temperature dependent resistivity,  $\rho(T)$ , for the films with thicknesses 3, 11, 30, 77, and 224 uc. Even though we find a slow increase in resistivity as the film thickness decreases from 224 to 3 uc, the films maintain their metallic behavior below room temperature from 224 uc to 3 uc, with the lowest room temperature resistivity of  $\sim 1.4 \text{ m}\Omega \text{ cm}$  for the 224 uc thick films. The observation of the metallic resistivity in the 3 uc film is possible due to its high crystalline quality. The room temperature Hall Effect measurements (not shown here) revealed p-type

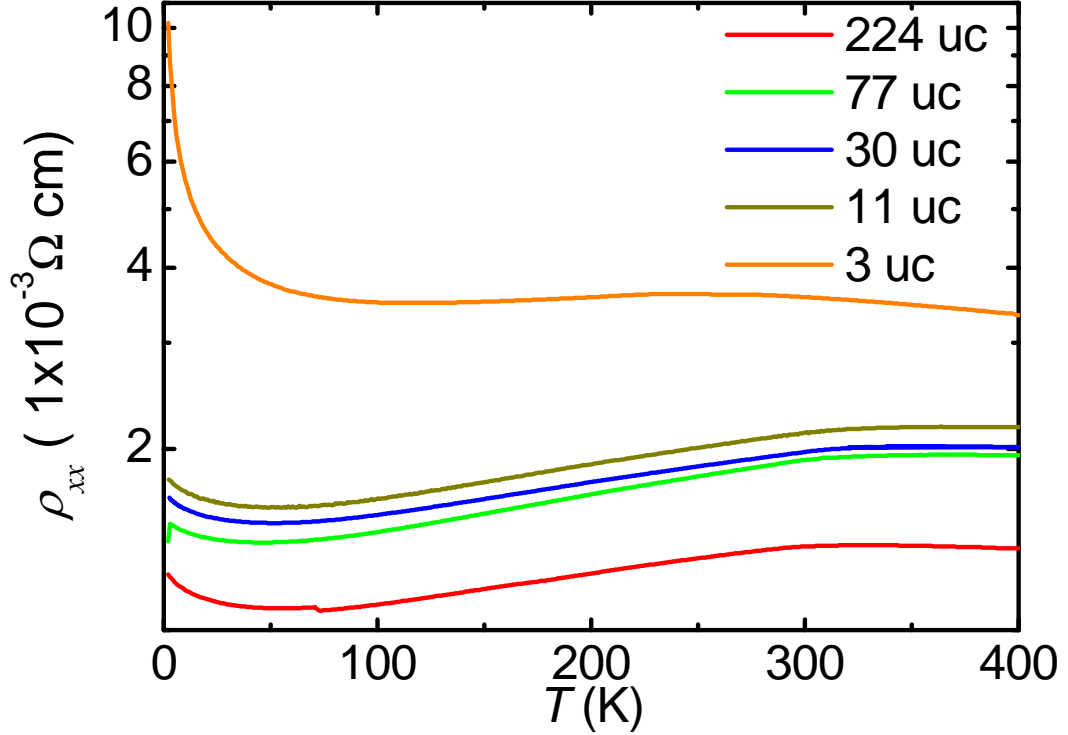


Figure 5.3: In-plane resistivity  $\rho$  vs. temperature  $T$  for the  $\text{NiCo}_2\text{O}_4$  with the thicknesses of 3, 11, 30, 77, and 224 unit cells. The films maintain their metallic behavior below room temperature from 224 uc to 3 uc, with the lowest room temperature resistivity of  $\sim 1.4 \text{ m}\Omega \text{ cm}$  for the 224 uc thick films.

conduction. A region with dominant anomalous Hall effect was found in low magnetic fields (below 0.8 kOe).

## 5.5 Observation of QIE

The insight of the nature of electronic conduction in  $\text{NiCo}_2\text{O}_4$  at low temperatures and few-unit-cell thicknesses can be gained by examining the temperature dependence of resistivity below  $T_{\min}$  (Fig. 5.4). Similar-looking resistivity minima are found in a wide range of magnetic materials and have been attributed to the Kondo effect[112], magnetic cluster scattering[113], spin-polarized tunneling through grain boundaries[114], and quantum interference effects (QIE) via the Coulomb interaction between electrons enhanced by disorder or the weak localization.[115, 116, 92, 117]

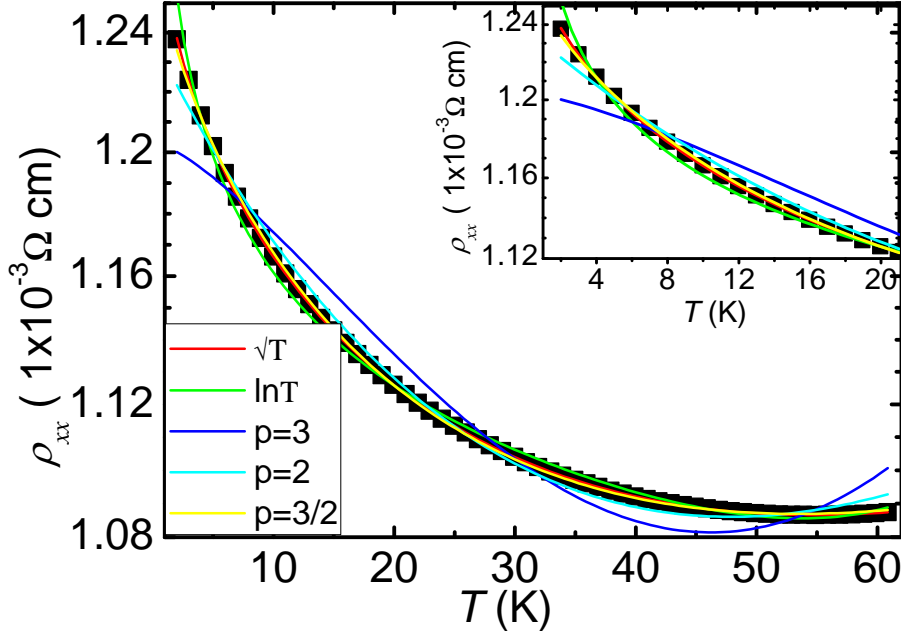


Figure 5.4: Resistivity  $\rho(T)$  for the 224 uc film and the fitted lines for Eqs. (5.1) to (5.3). The inset shows the magnified scale. The best fits of the measured data are achieved with Eq. (5.2) and Eq. (5.3) with  $p=3/2$ , indicating the disorder-induced QIE in the 3D limit are responsible for the resistivity minimum in  $\text{NiCo}_2\text{O}_4$

Spin-polarized tunneling through grain boundaries is significant only in polycrystalline samples and we exclude it from consideration here. To consider the possibility of Kondo-like spin-dependent scattering as the source of the resistivity minimum in our  $\text{NiCo}_2\text{O}_4$  films, we fit the temperature dependence of  $\rho(T)$  in the 2-60 K range with the functional form

$$\rho(T) = \frac{1}{\sigma_0 + C \ln T} + AT^n \quad (5.1)$$

where all scattering processes, such as electron-phonon, electron-magnon, and electron-electron, are described by the single power law ( $AT^n$ ) term, and  $\sigma_0$ ,  $C$ ,  $A$ , and  $n$  are fitting parameters. The fitting was carried out for all metallic films and as an illustration, the best fit for the 224 uc film is shown in Fig. 5.4. As discussed below, the logarithmic temperature dependence of the low-temperature resistivity in Eq. (5.1) does not provide the best fit of the data. Therefore, we do not consider Kondo-

like scattering as the cause of the resistivity upturn below  $T_{\min}$ . Such conclusion is consistent with our earlier observation that the low-temperature upturn is more pronounced in high-temperature-grown non-magnetic  $\text{NiCo}_2\text{O}_4$  films[82], and also speaks against the magnetic cluster scattering as the dominant physics behind the minimum resistivity. The logarithmic temperature dependence of Eq. (5.1) could also describe the residual conductivity governed by the disorder-enhanced electron-electron (e-e) interactions or the weak localization in the 2D limit. The unsatisfactory fit to Eq. (5.1) allows us to exclude such 2D QIE as well.  $\text{NiCo}_2\text{O}_4$  is an intrinsically disordered material, as Ni and Co cations are randomly distributed over the occupied octahedral sites. The disorder-induced localization tendencies in the 3D limit are described by the following equations:

$$\rho(T) = \frac{1}{\sigma_0 + B\sqrt{T}} + AT^n \quad (5.2)$$

$$\rho(T) = \frac{1}{\sigma_0 + BT^{p/2}} + AT^n \quad (5.3)$$

where  $\sigma_0$ , B, A and n are fitting parameters. Equation (5.2) describes the correction to resistivity due to disorder-enhanced e-e interaction, while Eq. (5.3) describes the weak localization with the parameter p dependent on the dominant scattering mechanism[92, 117, 118, 119] : p=3/2 for the e-e scattering in the dirty limit, p=2 for the e-e scattering in the clean limit, and p=3 for the electron-phonon scattering. As Fig. 5.4 shows, the best fits of the measured data are achieved with Eq. (5.2) and Eq. (5.3) with p=3/2. The fits using Eq. (5.3) with p=2 and p=3 are not adequate. Therefore, we propose that disorder-induced QIE in the 3D limit are responsible for the resistivity minimum in  $\text{NiCo}_2\text{O}_4$ , although the present data do not allow us to distinguish between the contributions of the Coulomb interaction and the weak localization. The Coulomb interaction should result in a positive magnetoresistance, while we expect negative magnetoresistance from the weak localization. In the  $\text{NiCo}_2\text{O}_4$

films, we reported negative magnetoresistance of 2% in the field of 1 T.[82] However, this magnetoresistance also includes the effects of the double-exchange, which was proposed as the mechanism of the metal-insulator transition in  $\text{NiCo}_2\text{O}_4$ [109] and which may mask the contributions of the QIE to the magnetoresistance. Since the two contributions to the QIE generally produce effects of the same magnitude, we believe that they both are present in the studied  $\text{NiCo}_2\text{O}_4$  films, even though the weak localization is likely to become stronger in the ultrathin films.[120]

## 5.6 Magnetic Properties

The magnetic measurements on the  $\text{NiCo}_2\text{O}_4$  films of various thicknesses are summarized in Figs. 5.5 (a) and (b). We have subtracted the diamagnetic contribution from the substrate by a separate measurement. Figure 5.5 (a) shows the magnetization as a function of temperature  $m(T)$  measured in the 2 kOe field for the 3, 11, 30, 77, and 224 uc films with no significant change in the Curie temperature  $T_c$  with decreasing thickness[121] down to 11 uc. Figure 5.5 (b) displays the  $m(H)$  hysteresis curves of these films measured at 10 K. For the films thinner than 30 uc,  $H_c$  increases significantly (the inset of Fig. 5.5(a)) and reaches the maximum of  $\sim 1500$  Oe in the 3 uc film. The coercivity is likely promoted by the decreasing film thickness as the relative strength of the surface and/or interfacial domain wall pinning increases compared to the bulk magnetic energy. The dependence of the saturation magnetization on the film thickness is shown in the inset of Fig. 5.5(d); the magnetization begins to degrade below the thickness of 7 uc. The sheet conductance ( $G$ ) at  $T_{\min}$  shows a linear dependence with thickness with a finite intercept of the x axis at 2 uc (Fig. 5.5 (c)). Similarly, the magnetic moment  $M_s = mV$  ( $V$  = film volume) decreases linearly with thickness and intersects the x axis at  $\sim 2$  uc (Fig. 5.5(d)). Based on the two intercepts, we estimate the thickness of the electrical and magnetic

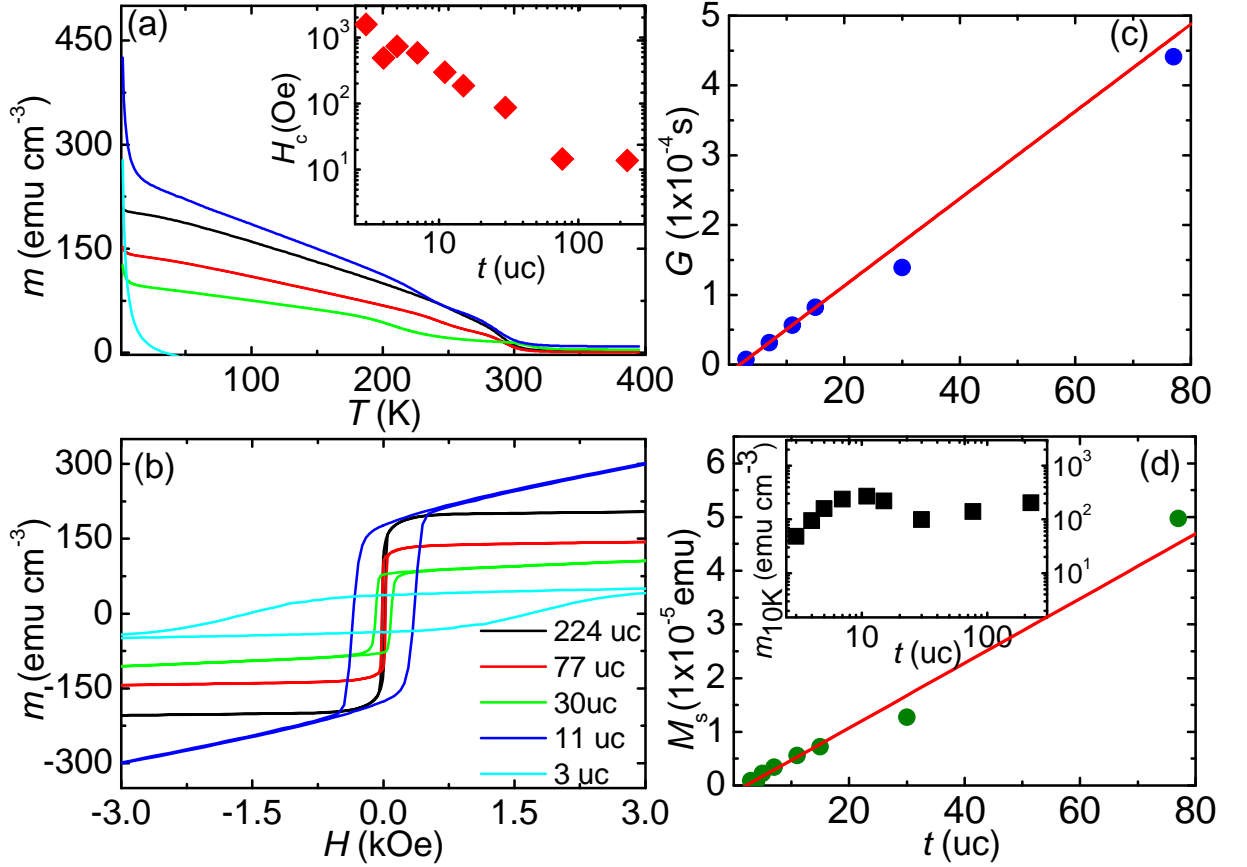


Figure 5.5: (a) Magnetization  $m$  vs. temperature  $T$  for the NiCo<sub>2</sub>O<sub>4</sub> films with the thicknesses of 3, 11, 30, 77, and 224 unit cells. The inset is the coercive field  $H_c$  vs. thickness  $t$ . (b)  $m$  vs. magnetic field  $H$  for the same set of films. (c) Sheet conductance  $G$  vs. thickness  $t$ . (d) Saturation magnetic moment ( $M_s$ ) at 5 kOe vs. thickness  $t$ . The inset shows saturation magnetization  $m$  at 5 kOe vs. thickness  $t$  (closed circles) and  $(mt/(t-t_{dead}))$  vs. thickness  $t$  (open triangles).  $t_{dead} = 2$  uc is the thickness of the magnetic dead layer.

dead layers to be 2 uc (1.62 nm). For comparison, the electrical dead layer thickness in ultrathin La<sub>0.7</sub>Sr<sub>0.3</sub>MnO<sub>3</sub> films was reported as 3.2 nm and 4 nm and the magnetic dead layer thickness as 1.2 nm and 10 nm.[122, 123]

## 5.7 Conclusion

In summary, we presented the thickness-dependent structural, electronic, and magnetic properties of epitaxial NiCo<sub>2</sub>O<sub>4</sub> films. The structural analysis revealed that



the epitaxial strain in the  $\text{NiCo}_2\text{O}_4/\text{MgAl}_2\text{O}_4$  (001) films is independent of the films thickness up to 700 nm. We found that the films remain metallic and magnetic down to 2 uc in thickness. The resistivity minimum with  $T_{\text{min}} \sim 50\text{-}60$  K is explained as the consequence of the disorder-induced quantum interference effects. We also observed the enhanced coercivity in thinner films, which could plausibly result from the domain wall pinning at the surface/interface. The enhanced magnetic properties and the metallicity make the ultrathin epitaxial  $\text{NiCo}_2\text{O}_4$  films a good candidate material for spintronics, e.g., as a spin injection or magnetic tunnel junction electrode material.

# Chapter 6

## Terahertz Spectroscopy

### 6.1 Introduction

The THz frequency range covers the spectral range from about  $3\text{ cm}^{-1}$  to  $350\text{ cm}^{-1}$ , which is known as Far-infrared (FIR) region of the spectrum. This range covers the frequencies on the order of about 0.1 to 10 THz, wavelengths from 3 mm to  $30\text{ }\mu\text{m}$ , or energies from 0.41 meV to 41 meV as 1 THz is equivalent to  $33.33\text{ cm}^{-1}$ ,  $300\text{ }\mu\text{m}$ , or 4.1 meV. The generation and detection of short pulses of terahertz (THz) frequency radiation are attracting great interest because of its increasing applications in many fields; such as THz imaging and THz spectroscopy.[124, 125, 126]. This frequency range offers many interesting phenomena and effects. In condensed matter physics, a number of excitations such as phonons, plasmons, excitons, polarons, and cyclotron resonance occur in this range.

#### 6.1.1 General Principle of Terahertz Time-Domain Spectroscopy

The basic principle of Terahertz Time-Domain spectroscopy (THz TDS) can be described in the following way; radiation from a light source is sent through a sample, which can be of various kinds. According to the classical laws of optics, the beam propagates through the sample being reflected, transmitted, refracted, diffracted or scattered. The most important phenomena observed in spectroscopy are absorption

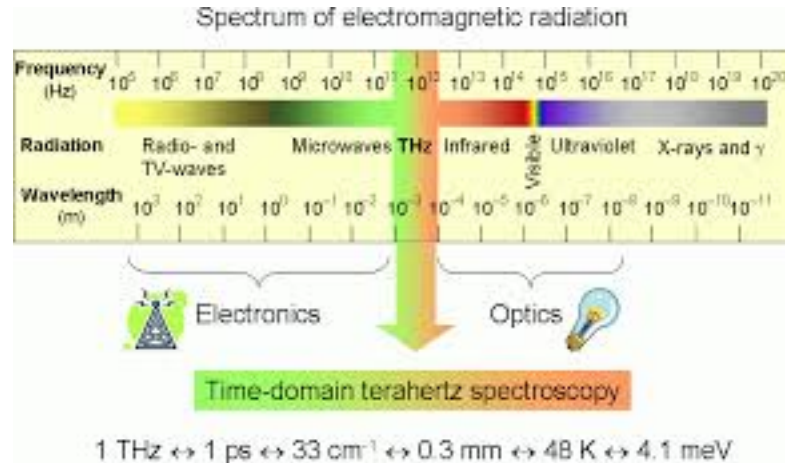


Figure 6.1: Spectrum of electromagnetic radiation. Using time-domain terahertz spectroscopy, we are able to access the terahertz (THz) gap.[127]

and dispersion as the beam propagates through the sample but also other effect such as non-linearity or polarization dependent phenomena are studied. Finally, the beam leaving the sample is altered by the sample properties. From here on, the beam contains the spectroscopic information that we are interested in.

The final step of a spectroscopic setup is the detection, in which the spectroscopic information is extracted from the beam by a photo-sensitive device, transformed into a signal and finally analogously or digitally stored. In order to guide the beam from the light source through the sample and finally to the detector, there are many optical devices involved such as mirrors, waveplates, lenses, polarizers, beam splitters, prisms, delay stage etc. Each optical devices has an important function in setups.

### 6.1.2 Optical rectification and second harmonic generation

Optical rectification is a non-linear process which occurs when an intense optical beam passes through a medium and generation of DC polarization occurs. It is a second order phenomenon, known as difference frequency generation (DFG). A material with strong non-linear coefficient interacts with femtosecond laser pulses and

causes different frequency mixing between various frequencies contained in the bandwidth of the laser pulse.[128] A polarization is produced by mixing different frequency components which result emission of electromagnetic waves in the THz region. The generation of THz radiation can be understood as a phase-matched non-linear  $\chi^2$  process.[129]

The electric polarization  $\vec{P}$  of a material is proportional to the applied electric field  $\vec{E}$ .

$$\vec{P} = \chi(E)\vec{E} \quad (6.1)$$

where  $(E)$  is the electric susceptibility. In the intense electric field, the electric  $\vec{P}$  is no longer linearly proportional to  $\vec{E}$ . The linear electrooptic effect describes a change of polarization of a crystal from an applied electric field. The nonlinear optical properties of the material are described by expanding  $\chi(E)$  in powers of the field  $E$ .

$$\vec{P} = (\chi_1 + \chi_2\vec{E} + \chi_3\vec{E}^2 + \chi_3\vec{E}^3 + \dots)\vec{E} \quad (6.2)$$

Optical rectification(OR) and second harmonic generation (SHG) both are second order non-linear optical effect ( $P_2^{nl}$ ) and described by

$$P_2^{nl} = \chi_2 E^2 \quad (6.3)$$

term in the expansion. Consider an electric field is described by  $E = E_0 \cos \omega t$ , then the  $2^{nd}$  order nonlinear polarization  $P_2^{nl}$  is,

$$P_2^{nl} = \chi_2 \frac{E_0^2}{2} (1 + \cos 2\omega t) \quad (6.4)$$

The dc polarization term  $\chi_2 \frac{E_0^2}{2}$  results from the rectification of the incident optical electric field by the second-order nonlinear electric susceptibility of the material. The

polarization with the  $\cos 2\omega t$  dependence is the second harmonic generation. Optical Rectification is a special case of difference frequency generation where two fields at frequency  $\omega$  yield one field at 'zero' frequency, whereas second harmonic generation is a sum frequency generation where two fields at frequency  $\omega$  yield one field at twice the frequency  $2\omega$ . [130] THz generation by OR may be thought of as a process where different frequencies within the bandwidth of optical generation pulse mix, forming light at the difference frequency. Hence the bandwidths of ultrashort THz pulses generated by OR are limited by the generation pulse bandwidth. However, the strong lattice phonon absorption of the generating crystal limit the bandwidth less than the transform-limited bandwidth.

The optical rectification is the  $2^{nd}$  order nonlinear effect which appears in anti-centrosymmetric crystals. [131, 132, 133, 134, 135, 136, 137, 138, 139] Typical crystals are (110) zinc telluride (ZnTe) or gallium phosphide (GaP). A detailed mathematical expression for the electro optic coefficient of zinc blende non linear crystal was derived by Namba. [140] The generation of THz from a non-linear crystal has been possible after the development of ultrafast lasers. Shen and coworkers [141] successfully generated THz radiation by illuminating LiNbO<sub>3</sub> and Auston and Cheung [142] demonstrated optical rectification on lithium tantalate (LiTaO<sub>3</sub>) non linear crystal to produce THz radiation. Zhang and co-workers reported THz radiation from various non-lonear crystals such as GaAs, LiTaO<sub>3</sub>, InP, [143, 137, 136, 144] and other materials such as ZnSe, GaSe, ZnGeP<sub>2</sub>, CdTe, has been used for THz generation via OR. In our lab, we employ non linear crystal zinc telluride (ZnTe) and lithium niobate (LiNbO<sub>3</sub>, LN) for THz generation via OR, will be discussed in detail in following section.

### Phase-matching condition

As we can see in equation 6.4, the input wave generates a set of dipoles inside the crystal that all radiate weakly twice the frequency of the input wave. As the input beam has a well defined phase and amplitude at each point inside the crystal at a given time, the relative phase of the induced dipole is fixed. To obtain the second harmonic output at the end of the crystal, it is important for the induced dipoles to radiate in phase. This is called phase the matching condition.

At every position in the crystal, the non-linear polarization creates a dipole emitter which radiates at twice the fundamental frequency. The emitted wave has phase in the form  $\exp(-ik_{2\omega}z)$ . The overall efficiency of this process in forward direction is obtained by adding all contributions from different positions.[145]

$$\eta = \frac{1}{L^2} \left| \int_0^L e^{i2k_\omega z} e^{i2k_{2\omega} z} dz \right|^2 = \frac{1}{L^2} \left| \int_0^L e^{i\Delta k z} dz \right|^2 = \left( \frac{\sin \Delta k L / 2}{\Delta k L / 2} \right)^2 \quad (6.5)$$

where  $\Delta k = 2k_\omega - k_{2\omega}$  is wave vector mismatch of the process and  $L$  is crystal thickness. The sine function is maximum when  $\Delta k = 0$  [145, 130] and the efficiency  $\eta$  is 1.

$$\Delta k = \frac{2\omega n(\omega)}{C} - \frac{2\omega n(2\omega)}{C} \quad (6.6)$$

$\Delta k = 0$  requires,

$$n(2\omega) = n(\omega) \quad (6.7)$$

But most of the materials that are transparent in the visible, have refractive index decreased with increasing the wavelength. Hence it is impossible to achieve efficient SHG in these materials. Birefringent materials have different refractive indices for different polarizations; the ordinary and extraordinary refractive index ( $n_o$  and  $n_e$ ). Using birefringent crystals we can satisfy the phase matching condition.

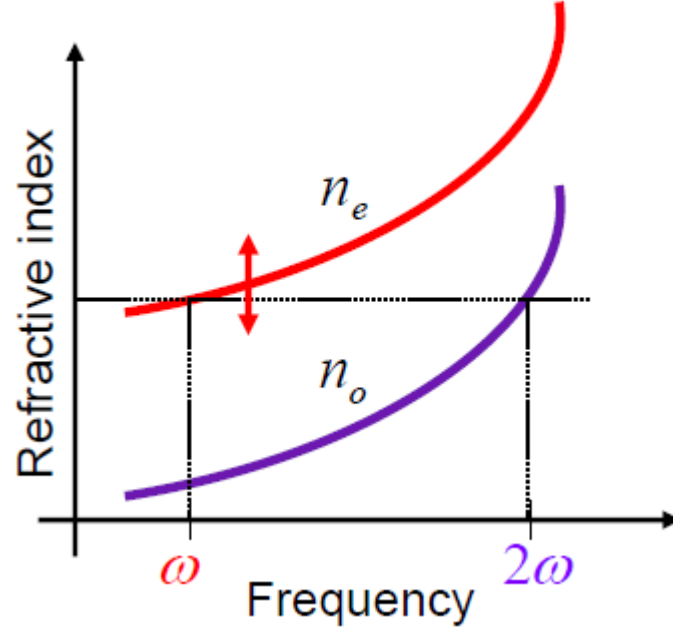


Figure 6.2: Ordinary refractive index  $n_o$  and extra-ordinary refractive index  $n_e$  of a birefringent material as a function of  $\omega$ . [146]

For example, as shown in figure 6.2, we can use extraordinary polarization for  $\omega$  and ordinary polarization for  $2\omega$ . Then,

$$n_o(2\omega) = n_e(\omega) \quad (6.8)$$

Here,  $n_e$  depends on propagation angle, so by rotating the birefringent crystal, we can tune the condition precisely by moving the red curve up and down relative to the blue curve.

### 6.1.3 Electro-Optic Effect or Pockel's Effect

The electric displacement field  $\vec{D}$  is related to the electric field  $\vec{E}$  through the polarization field  $\vec{P}$  in a medium

$$\vec{D} = \vec{E} + 4\pi\vec{P} \quad (6.9)$$

Most often, the polarization field is considered to be linearly related to the incident electric field

$$\vec{P} = \chi \vec{E} \quad (6.10)$$

For the case of linear medium with  $P = \chi_1 \vec{E}$ , from the above equation a displacement field is

$$\vec{D} = \vec{E} + 4\pi\chi_1 \vec{E} = (1 + 4\pi\chi_1) \vec{E} \quad (6.11)$$

Also,

$$\vec{D} = \epsilon \vec{E} \quad (6.12)$$

and refractive index,  $n_0 = \sqrt{\epsilon}$

Hence,

$$n_0 = \sqrt{1 + 4\pi\chi_1} \quad (6.13)$$

The refractive index in this case is independent of the applied electric field. But when a low frequency,  $\Omega$ , or a dc electric field  $E_0(\omega = 0)$  is applied to a medium, the optical dielectric constant of the medium  $\epsilon(\omega, E_0)$  may depend on the amplitude of applied electric field  $E_0$ . When the applied field has small amplitude,  $\epsilon(\omega, E_0)$  can be expressed as a power series of  $E_0$  as,[147]

$$\epsilon(\omega, E_0) = \epsilon^{(1)} + \epsilon^{(2)}(\omega + \Omega)E_0 + \epsilon^{(3)}(\omega + 2\Omega)E_0^2 + \dots \quad (6.14)$$

Since

$$\vec{D} = \epsilon_0 \vec{E} + \vec{P} \quad (6.15)$$

and

$$\vec{P} = (\chi_1 + \chi_2 \vec{E} + \chi_3 \vec{E}^2 + \chi_3 \vec{E}^3 + \dots) \vec{E} \quad (6.16)$$



, the non-linear terms of optical dielectric constant will be,

$$\epsilon^{(2)}(\omega + \Omega) = \frac{1}{\epsilon_0} \chi_2(\omega + \Omega) \quad (6.17)$$

$$\epsilon^{(3)}(\omega + 2\Omega) = \frac{1}{\epsilon_0} \chi_3(\omega + 2\Omega) \quad (6.18)$$

A medium with no inversion symmetry will have an electrooptic effect dominated by the linear term  $\epsilon^{(2)}E_0$ . This effect is known as the linear electrooptic effect or the Pockel's effect. The refractive index becomes a function of the electric field which results in the change in the change of the orientation of the of the index ellipse. The quadratic term  $\epsilon^{(3)}E_0^2$  is called the Kerr effect.

## 6.2 THz Generation

The most common mechanisms for broadband pulsed THz emission from a semiconductor material using ultra-short excitation pulses are optical rectification, photo-conductivity, and the transient current effect. We have used optical rectification method using ZnTe(110) crystal, tilted wavefront and photoconduction THz generation in our spectrometer, which will be discussed in following section.

### 6.2.1 Optical Rectification in ZnTe Crystal

We use a ZnTe (110) crystal emitter of 0.5 mm thickness at normal incidence to generate THz pulses by the optical rectification process. Femtosecond laser pulses are used to generate THz from EO crystals via optical rectification. The optical excitation causes a change in the polarization of the crystal due to the non-linearity of the material to produce sum-frequency and difference polarization component. The polarization components with the different frequencies are in THz range and the sum frequency components correspond to second-harmonic generation are in the visible or ultraviolet range. The THz radiation generated by optical rectification is

strongly dependent on the orientation of the visible exciting field with respect to the crystal.[148] The nonlinear polarization induced in the material can be written as;

$$P^2(\omega = \omega_1 + \omega_2) = \chi^2 E_1(t)E_2(t)\cos(\omega_1 t)\cos(\omega_2 t) \quad (6.19)$$

$$= \frac{1}{2}\chi^2 E_1(t)E_2(t)[\cos(\omega_1 - \omega_2)t + \cos(\omega_1 + \omega_2)t] \quad (6.20)$$

$$= P_{OR}^2 + P_{SHG}^2 \quad (6.21)$$

where  $P$  is the polarization,  $\chi$  is the nonlinear susceptibility,  $E$  is the electric amplitude of incident beam. The subscripts OR and SHG correspond to the optical rectification and second harmonic generation terms. The above equation shows that optical rectification is directly proportional to the incident wave intensity, and is in general time-dependent. Second harmonic generation is inevitable, but since the beam probes different refractive indices, the phase matching condition is different. Phase matching and the coherence length are also of critical importance to efficient OR. The perfect phase matching condition is given by [149]

$$\Delta k = k(\omega_{opt} + \omega_{THz}) - k(\omega_{opt}) - k(\omega_{THz}) = 0 \quad (6.22)$$

The efficiency of the nonlinear optical THz generation and detection decreases if the mismatch between the velocities becomes too large. The distance over which the slight velocity mismatch can be tolerated is called the coherence length and is given by,[149]

$$l_c(THz) = \frac{\pi C}{\omega_{THz}|\eta_{opt}(\omega_0) - \eta_{THz}(\omega_T Hz)|} \quad (6.23)$$

The THz emission from optical rectification is described diagrammatically in Fig.(6.3).

Although ZnTe is probably the most chosen material for material for optical rectification, it has several limitations.[150, 151] ZnTe has a relatively low band gap,

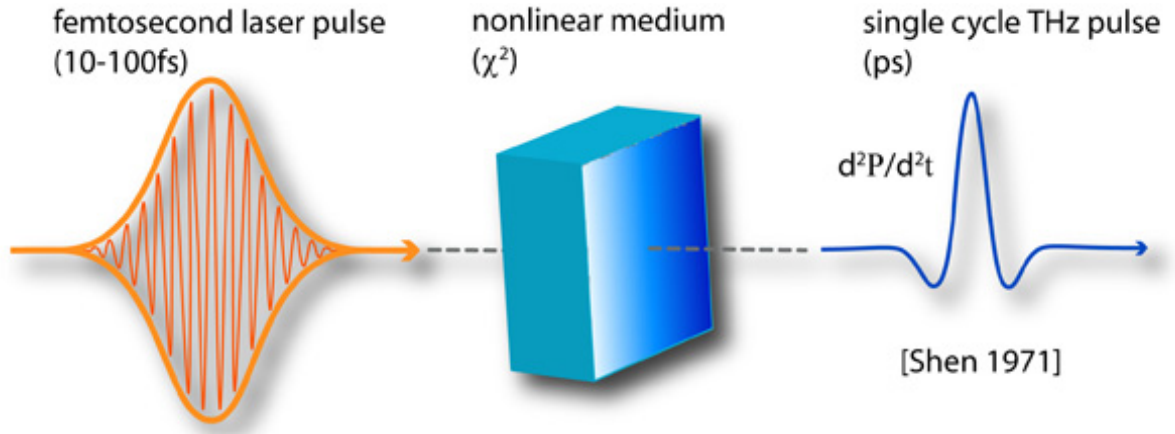


Figure 6.3: A schematic diagram of THz generation in ZnTe(110) crystal by optical rectification.

and two photons absorption of the pump beam occurs at low powers relative to the damage threshold of the material.[152, 153, 154, 155, 156] The two-photon absorption generates free charge carriers, which strongly absorb THz radiation.[151] This limits the excitation pulse energy to below what is commonly available in amplified Ti:Sapphire systems. Secondly, ZnTe has its lowest optical phonon mode at 5.3 THz, significantly limiting the frequency coverage of a THz-TDS instrument. This complication can be partially avoided by switching crystals for higher frequency emission, to GaP for example, which has its lowest phonon mode at 11 THz.[157, 158] Lastly, the non-linear coefficient of ZnTe is 68.5 pm/V, lower than that of other nonlinear crystals such as lithium niobate LiNbO<sub>3</sub> has 168 pm/V.

### 6.2.2 Tilted Pulse Front

Due to the above mentioned limitations in ZnTe, researchers have been investigating alternative ways of establishing phase matching in other crystals. One of the most successful way is to create an angle between the directions of propagation of the optical pump and THz pulse. This technique is called tilted pulse front. Tilted wavefront THz generation is a technique used to achieve extremely high fields in the THz pulse. For example, a peak electric field of 1.2 MV/cm has been reported by

Hirori et al.[159] In conventional optical rectification, the emitted THz beam and the optical beam propagate collinearly and with different velocities, as the refractive indices for THz and optical wavelengths are generally different. This results in the dephasing of the two beams, which is detrimental to THz emission. The tilt angle may be established by tilting the front of the optical pump pulse by using a frequency separating element such as a grating or prism and a focusing element such as a lens. The THz wave is generated in a crystal with a second order optical nonlinearity (typically LiNbO<sub>3</sub>) through optical rectification. The wavefront tilting provides a way to match the phases of the propagating optical beam and the emitted THz beam, which ensures that each newly emitted THz photon is in phase with THz photons emitted earlier in the THz beam path.

When the wavefront of the optical beam is tilted, the generated THz wave propagates perpendicular to the wave-front and at an angle to the optical beam. This allows efficient phase matching if an appropriate wave-front tilt angle is selected for the optical beam. The phase matching condition requires that the velocities of the optical and the THz beams satisfy the relation[161],

$$V_{opt}\cos\gamma = V_{THz} \quad (6.24)$$

where  $\gamma$  is the wavefront tilt angle inside LN. Since the beam velocities are inversely proportional to the corresponding refractive index, we find

$$\cos\gamma = \frac{n_{opt}}{n_{THz}} \quad (6.25)$$

and  $\gamma \sim 63^\circ$  using the refractive indices  $n_{opt} = 2.25$  and  $n_{THz} = 4.96$  [162, 161].

Figure (6.5) shows the schematic of the implemented tilted wavefront setup. A femtosecond optical pulse impinges on a diffraction grating that tilts the phase

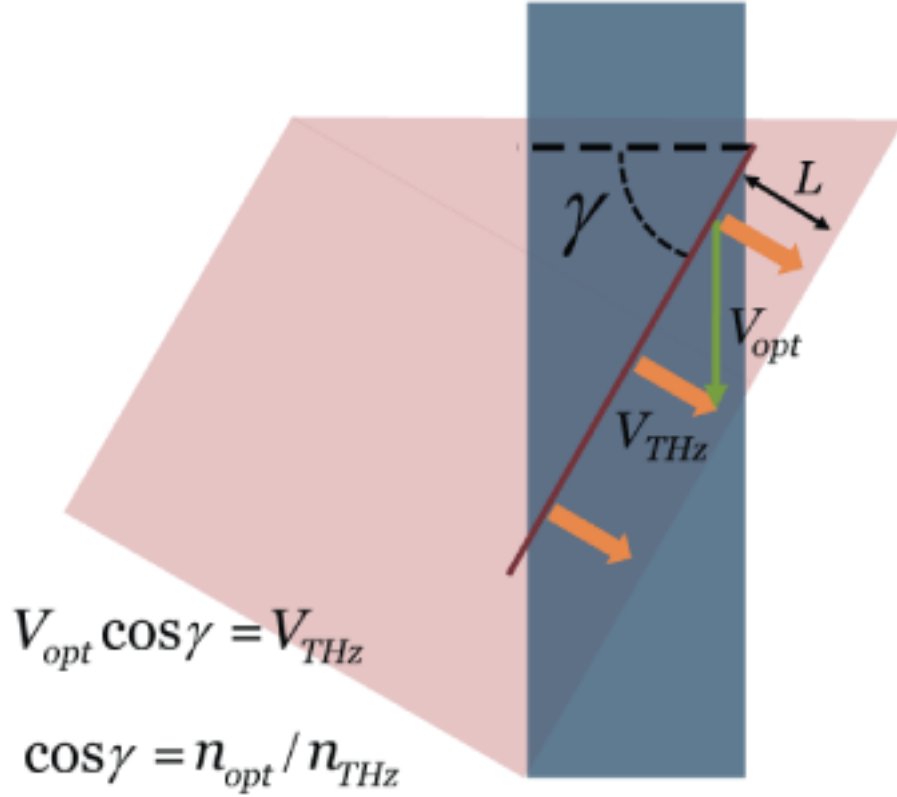


Figure 6.4: THz emission generated by an optical beam with a tilted wavefront in LiNbO<sub>3</sub>. THz beam (red arrows) is emitted perpendicular to the wavefront (green line). Phase matching condition is satisfied when the velocities of the THz and optical beam (red and blue arrows) and the wavefront form a right-angle triangle, which also determines the tilt angle  $\gamma$ . [160]

front (wavefront) of the optical pulse. The polarization of the optical pulse at the grating is horizontal (in the plane of Fig. 6.4) and is rotated to vertical by a wave plate positioned between the grating and the LiNbO<sub>3</sub> prism. The lens images the optical beam spot on the grating onto the face of the LiNbO<sub>3</sub> prism. The THz beam is generated by optical rectification and is polarized vertically. The emitted THz beam was then collimated and focused by con-focal off-axis parabolic reflectors onto

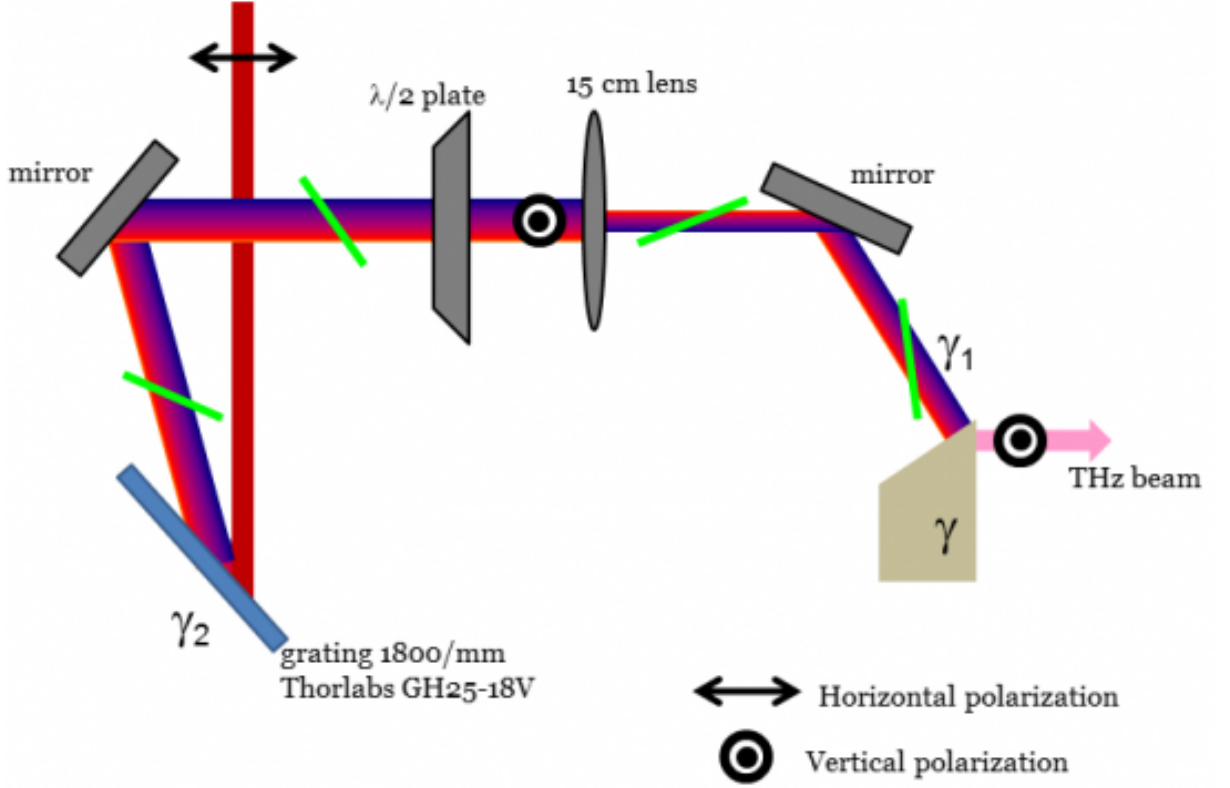


Figure 6.5: The layout of the tilted-wavefront THz emission setup. The diffraction grating tilts the wavefront of the optical excitation pulse. The green lines represent the wavefront tilt at different point along the beam path. The  $\frac{\lambda}{2}$  waveplate rotates the polarization of the excitation beam from horizontal to vertical.[160]

a receiver ZnTe crystal.

### 6.2.3 Photo conductive THz Generation

Photoconductive antennas are very popular means of generating and detecting THz pulses.[163, 164] In this mechanism, electrode structures with a micron scale antenna gap are fabricated on a semiconductor substrate typically low temperature grown GaAs (LT GaAs). The femto second laser pulses with photon energy larger than the band gap of the semiconductor material, is focused at the antenna gap to create electron-hole pairs.[164, 165, 166, 167, 168, 169, 170, 171, 172, 173, 174, 175,

176, 177] Then, those free carriers can be accelerated by the DC bias applied across the gap, which creates a transient current gradient and radiates THz pulses.

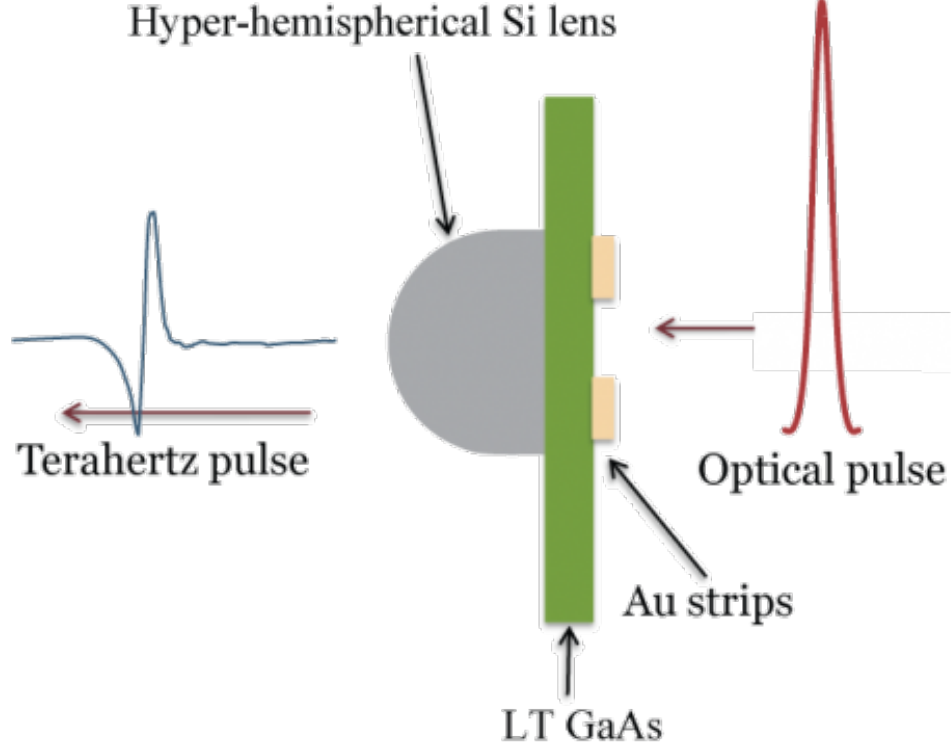


Figure 6.6: Schematic for the terahertz emitter. The incoming optical pulse excites electrons in the gold strips and creates a vertically polarized terahertz pulse that propagates out the other side of the LT GaAs wafer. The hyper-hemispherical lens helps collimate the terahertz pulse.[178]

In the far field approximation, the THz electric field  $E_{THz}(r, t)$  emitted from a photoconductive antenna at the observation point  $r$  and observation time  $t$  can be represented as[179, 180, 181],

$$E_{THz}(r, t) = -\frac{1}{4\pi\epsilon C^2} \int \left[ \frac{\partial j(r', t')}{\partial t'} \right]_{t'=t_r} \frac{\sin\theta}{|r - r'|} d^3x', \quad (6.26)$$

where,  $\epsilon$  and  $C$  are the dielectric constant of the medium and the speed of light respectively. The time derivative is taken at the retarded time,  $t_r = t - \frac{r-r'}{C}$ .  $\theta$  is the angle between the generated photo current and the direction of the detection.

$j(r', t')$  is the current density on the photo conductive antenna, which is related to the applied bias voltage  $E_{bias}$  as,

$$j(r', t') = \frac{\sigma(t)E_{bias}}{\sigma(t)Z_0/(1 + n_d) + 1} \quad (6.27)$$

where  $\sigma(t)$  is the conductivity,  $Z_0$  is the vacuum impedance, and  $n_d$  is the refractive index of the substrate.

Interference of field components generated from different points on the antenna produce the overall pattern of THz radiation. Generation of THz radiation through photoconductive mechanism depends on various factors such as antenna geometry, optical pulse duration, applied bias voltage, along with the properties of the photoconductive substrate such as band gap, carrier lifetime, and carrier mobility.[182]

## 6.3 THz Detection

We have used ZnTe (110) crystal based Electro-optic sampling technique and photoconductive receiving antennas for THz detection, which will be explained in detail in the following section.

### 6.3.1 Electro-optic Sampling

Electro-optic sampling (EOS) has developed into a powerful method for the detection of THz pulses.[173, 144] A variety of dielectric materials like LiTaO<sub>3</sub>[183, 184] and ZnTe[184] or polymers polarized by externally applied field[183, 185] are used for this purpose. In our lab, THz is measured by EOS technique on ZnTe crystal. In this technique, the THz beam and the probe beam are focused onto the ZnTe crystal. The THz electric field causes change in the refractive index of ZnTe, and this birefringence is proportional to the THz electric field (the Pockels effect). Therefore, different polarization components of the probe beam experience different



refractive index, which results in a change in the polarization direction of the probe beam. Then, this polarization direction change of the probe beam can be detected by a differential detector. By changing the delay time between the THz pulse and the optical pulse, the THz electric field is determined as a function of time.

For a zincblende crystal, such as ZnTe, when an electric field is applied, its ellipsoid of the refractive index is [186, 187]

$$\frac{x^2 + y^2 + z^2}{n_0^2} + 2\gamma_{41}E_xyz + 2\gamma_{41}E_yxz + 2\gamma_{41}E_zxy = 1 \quad (6.28)$$

where  $n_0$  is the refractive index of the crystal without electric field, X, Y, Z are coordinate units of the ellipsoid, and  $E_x$ ,  $E_y$ ,  $E_z$  are applied electric field along corresponding axes respectively.  $\gamma_{41}$  is the Electro-optic coefficient of the crystal. Passing through the electrooptic crystal, the horizontal and vertical components of the electric field of the incident optical wave acquire a phase shift as a function of refractive change. The phase delay  $\Gamma$  is the function of the change in refractive index and is given by following equation,

$$\Gamma = \frac{2\pi d}{\lambda} \Delta n \quad (6.29)$$

where  $d$  is the thickness of the EO crystal, and  $\Delta n$  is difference in the refractive index. The phase delay for a  $\langle 110 \rangle$  oriented ZnTe crystal is given by the equation, [187]

$$\Gamma = \frac{\pi d n_0^3 \gamma_{41} E}{\lambda} \sqrt{1 + 3 \sin^2 \phi} [for(110)crystal] \quad (6.30)$$

$$\Gamma = 0 [for(100)crystal] \quad (6.31)$$

where  $\gamma_{41}$  is the electrooptic coefficient of ZnTe crystal. The phase difference is proportional not only to the magnitude of the applied field but also to its sign which makes the whole detection process phase sensitive.

Zinc blende crystals are better suited for THz generation and detection because of improved phase matching compared to other crystals. Figure (6.7) shows the basic working technique of electro optical sampling detection. The THz pulse induces a birefringence in the ZnTe(110) crystal which alters the ellipticity of the linearly-polarized optical pulse. A quarter wave plate is placed behind the electrooptic crystal to make the initially linear polarization of the probe beam (at  $E_{THz} = 0$ ) circular. A Wollaston prism is placed after the quarter wave plate. After passing through the Wallaston prism, the probe beam is split into two beams with polarization directions along X axis and Y axis respectively and passes to a differential detector which is connected to a lock-in-amplifier. Changes in ellipticity are detected as differences in signal measured between the two balanced photo-diodes.

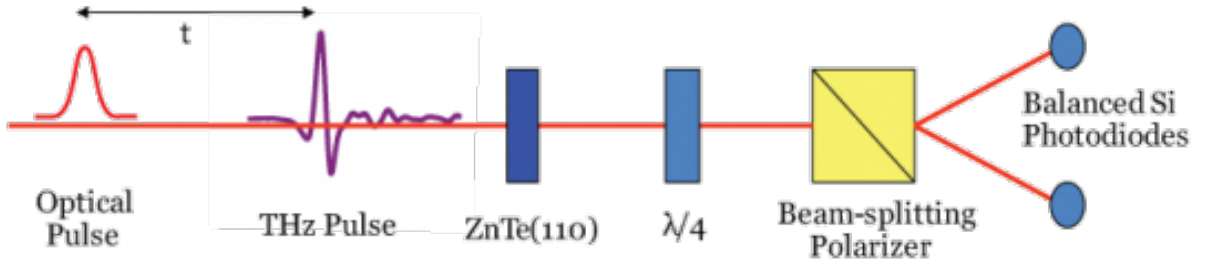


Figure 6.7: The setup for free-space electro-optic sampling and deconstructed into right- and left-handed components by the beam-splitting polarizer. This difference signal is proportional to the THz electric field.[178]

### 6.3.2 Photo Conductive receiving antennas

The use of photoconductive (PC) antenna as the terahertz detector is similar to the use of the PC antenna as an emitter. The electrodes are connected to a current sensor and the optical probe beam creates photocarriers. The photocarriers are generated in the substrate material. When the THz radiation is incident on the deceptor PC antenna, the photoexcited carriers are accelerated by the THz field giving rise to a signal current in the detector PC antenna. For a time delay  $\tau$ , the induced

photocurrent is given by the following expression[179],

$$i_{THz}(\tau) \propto \int G(t - \tau) E_{THz}(t) dt \quad (6.32)$$

where  $G(t)$  is the transient photoconductance of the antenna. For a substrate with extremely short carrier lifetime  $G(t)$  can be approximated as a delta function, and the current is proportional to  $E_{THz}(t)$ . For a substrate with long carrier lifetime,  $G(t)$  can be approximated as a step function and the current  $i_{THz}(\tau)$  is proportional to the time-integrated waveform of  $E_{THz}(t)$ . [179] The equation illustrates that the detection bandwidth is limited by the carrier dynamics of the material. Earlier PC antennas suffered from lower bandwidths.[188] However with the development of ultrashort lasers and better antenna structures, the detection bandwidth has been improved to be comparable to electro-optic detection.[189, 190] LT GaAs and ion-implanted silicon on sapphire[187] are the most commonly used materials for photoconductive THz generation.

## 6.4 Development of Terahertz Time-Domain Spectrometer

### 6.4.1 Laser

Optical rectification, photoconductive antennas and free-space electro-optic sampling are driven by femtosecond pulse laser excitation. We use a Spectra-Physics Spitfire ACE Ti:sapphire laser amplifier seeded by a mode-locked Spectra-Physics MaiTai laser. The output wavelength is 800 nm, the repetition rate is 1 KHz, and the pulse width is 35 fs and the average power is 4 watt.

### 6.4.2 THz Optics

THz optics are used for the collection of the THz from the source, to guide through air (and, eventually, a sample) and to focus onto a detector. The optical path of the THz radiation in an arrangement in our spectrometer has 3 focal points: for a THz emitter, a sample, and a detector. For this purpose we have used 2 sets of off-axis parabolic mirrors. The off-axis parabolic mirrors are designed to take rays parallel to the optical axis and focus them to a focus. Simultaneously, it takes rays from the point source at the focus and sends these rays out parallel to the optical axis.[191] In addition to the parabolic mirrors, our spectrometer uses beam splitters, mirrors, filters, polarizers, filters, diffraction gratings, focusing lenses etc.

### 6.4.3 Delay Stage

For delaying the excitation pulse with respect to the detection pulse, we have used a delay stage in our spectrometer. It uses two back-reflecting mirrors on a motorized stage which can achieve delay upto several nanoseconds. A delay of 0.3 mm corresponds to a time delay of 1 ps in the time-domain. The total delay time determines the frequency resolution of the spectrometer, and the delay step determines the maximum frequency, which is also limited by the pulse length of the sampling pulse.

### Cryostat

To enable low- and high-temperature measurement, we have installed a continuous flow cryogenic system and a closed-cycle cryogenic system. Our continuous flow cryogenic system uses liquid nitrogen continuously over a distance and the temperature range is 78 to 425 K. Our closed-cycle cryogenic system's temperature range is 9 to 325 K. The vacuum chamber is first evacuated by a turbo pump down to  $10^{-5}$  mbar. Then the cooling system is turned on.

In both the cryostats, the sample holder is attached to the heat station (or

cold finger) of the Coolstar unit. The sample holder consists of two circular apertures of 6 mm diameter. To provide thermal contact, samples are glued on the sample holder with a thin layer of silver paste. The cryostat is mounted on the computer controlled motorized XY stage to move the sample in the horizontal and vertical directions transverse to the THz beam. The Coolstar runs constantly at the same cooling power and the temperature of the samples is changed and stabilized by a heater integrated in the basement of the sample holder.

### Experimental Setup and Data Acquisition

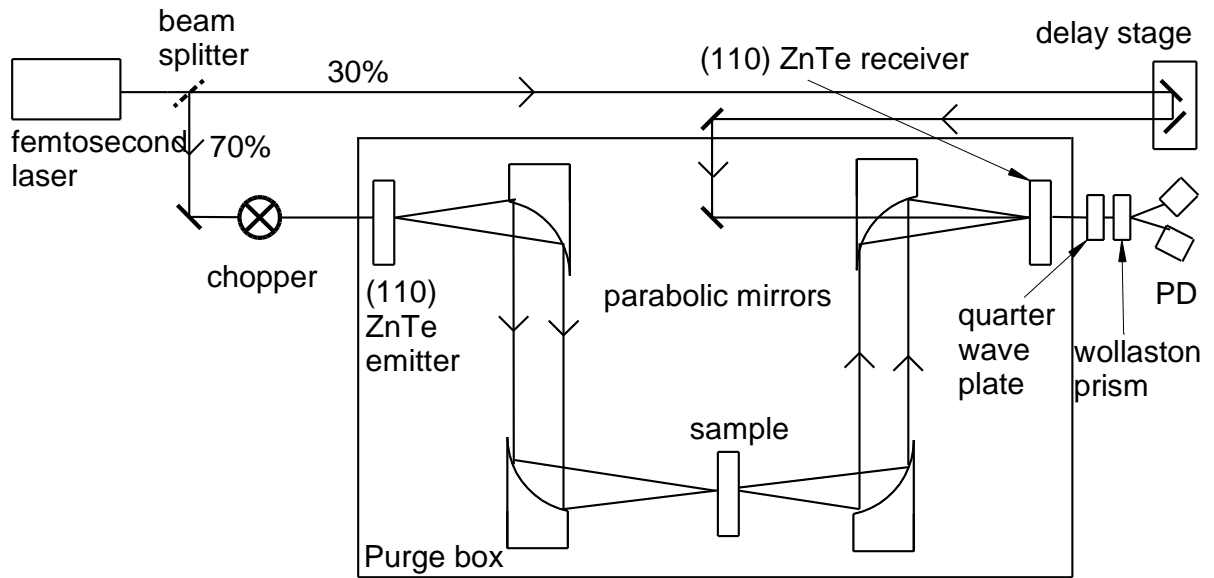


Figure 6.8: The schematic representation of our home-built terahertz time domain spectroscopy (THz TDS) system

The schematic diagram of our home-built terahertz time-domain spectroscopy (THz TDS) system is shown in Fig. 1. It uses a Spectra-Physics Spitfire ACE Ti:sapphire laser amplifier seeded by a mode-locked Spectra-Physics MaiTai laser. The output wavelength is 800 nm, the repetition rate is 1 KHz, and the pulse width is 35 fs. The maximum average power output is 4 Watts. The laser beam is divided into two arms by a beam splitter: a stronger generating beam (70%) for THz pulse emission

and a weaker gating beam (30%) for THz detection. The generating beam is then modulated by a mechanical chopper. A ZnTe (110) crystal emitter of 0.5 mm thickness is used at normal incidence to generate THz pulses by the optical rectification process. The released sub-picosecond pulse of THz radiation is then collimated and focused by two off-axis parabolic mirrors in a helium-flow cryostat. The transmitted THz pulse is collected and focused onto a 0.5 mm (110) ZnTe detector crystal by two other parabolic mirrors. The phase-sensitive detection is accomplished by a lock-in-amplifier and the data are recorded onto a computer. The detected signal results from the polarization rotation of the gating pulse due to the birefringence induced in the detector ZnTe by the THz electric field. By varying the time delay between the generating and the gating pulses, the amplitude of the THz pulses transmitted through sample and reference is recorded in time domain.

Ambient humidity can be problematic as water has absorption lines in the THz regime. Hence all the optical components and samples are enclosed in a purge box and purged with dry air to avoid water absorption. To enable low and high temperature measurement we have installed a continuous flow cryogenic system. The sample holder consists of two circular apertures of 6 mm diameter. To provide thermal contact, samples are glued on the sample holder with a thin layer of silver paste. The cryostat is mounted on the computer controlled motorized XY stage to move the sample in the horizontal and vertical directions transverse to the THz beam. Transmission measurements through sample and reference apertures are measured one after the other by moving the cryostat the appropriate distance to place the right aperture in the path of the THz pulses. We then compared the transmission through  $\text{NiCo}_2\text{O}_4$  film on  $\text{MgAl}_2\text{O}_4$  substrate sample to the bare  $\text{MgAl}_2\text{O}_4$  substrate reference to isolate the response of the  $\text{NiCo}_2\text{O}_4$  films. The measured THz amplitude for  $\text{NiCo}_2\text{O}_4$  300°C film (sample) and  $\text{MgAl}_2\text{O}_4$  (reference) at 300K is shown below

in Fig. 6.9 and the ratio of the amplitudes after Fourier transform is in Fig. 6.10. The inset is the difference between phases of the sample and reference.

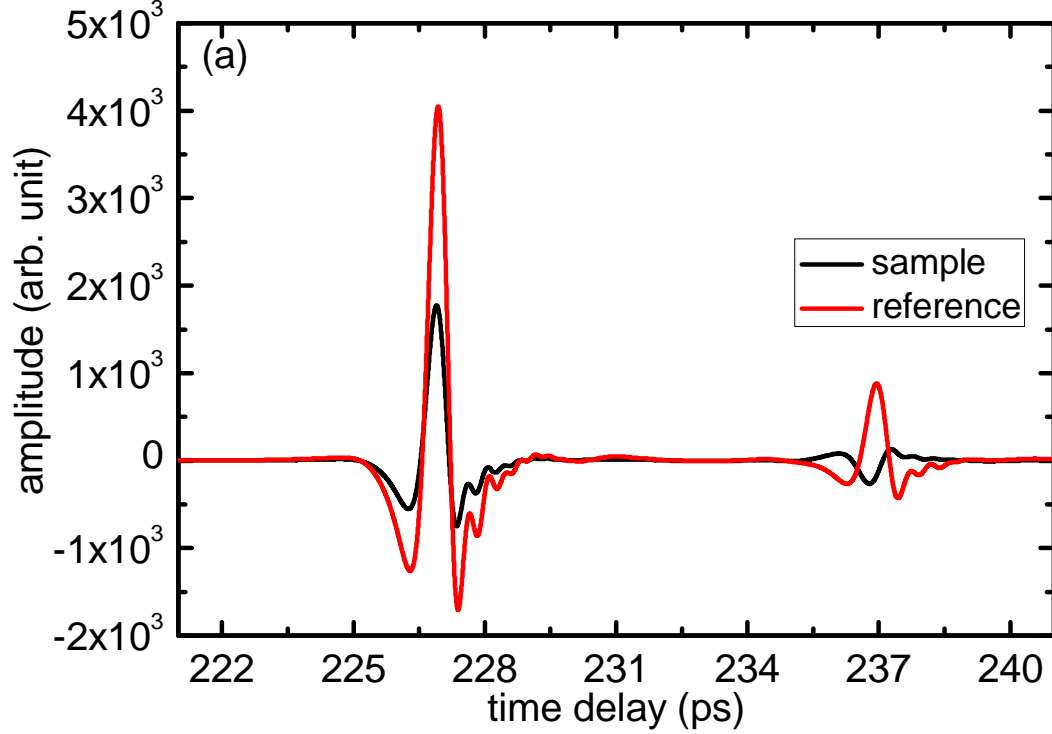


Figure 6.9: The measured amplitude of the transmitted terahertz pulse through sample and reference for  $\text{NiCo}_2\text{O}_4$  300°C at 300K. In the time-domain spectra, the first transient is the primary pulse passed directly through the medium. The second transient is due to the reflections of the primary pulse from the back and the front surfaces of the sample. Since the main transmitted pulse is well separated from the first reflected pulse, for the analysis, the data were windowed around the main transmitted pulse.

The basic idea of the transmission time-domain THz spectroscopy can be described in the following way, a sub-picosecond pulse of electromagnetic radiation passes through a sample. Its time profile is changed compared to the one of the reference pulse. The reference pulse can be either a freely propagating pulse or a pulse transmitted through a medium with known properties. Through the analysis of the change in complex Fourier spectrum introduced by the sample, the spectrum of the refractive index of the sample is obtained.

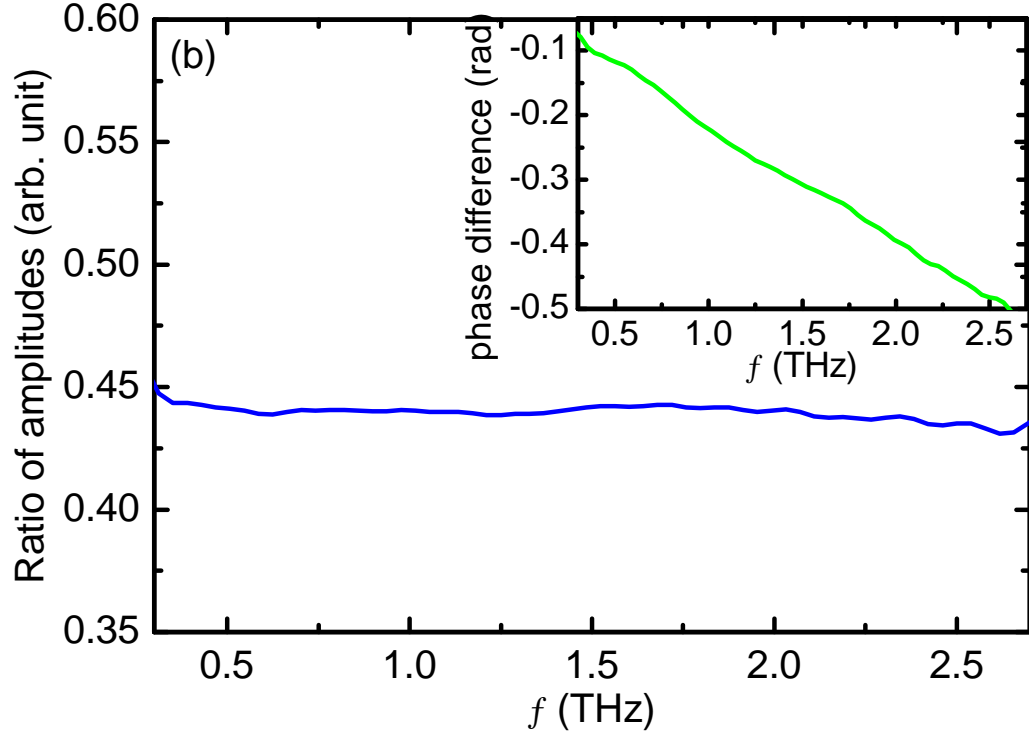


Figure 6.10: The amplitude of the ratio of the sample and reference Fourier transforms of the time-domain data. The inset is the difference between the phases of the sample and reference Fourier transforms.

The Fourier transformation of a THz pulse in the time domain yields a frequency distribution with amplitude and phase. The shorter the pulse length of the time-domain pulse, the broader is the frequency distribution. The width of the frequency distribution is called the frequency bandwidth or span. The accessible frequency span obtained from a discrete Fourier transformation depends on the temporal resolution  $\Delta t$  of the time-domain data. The maximum frequency  $f_{max}$  that can be sampled by Fourier transformation is given by Nyquist's theory,[192, 193]

$$f_{max} = \frac{1}{2\Delta t} \quad (6.33)$$

The frequency resolution  $\Delta f$  is inversely proportional to the window length  $T$ . Therefore, the longer the window length is, the higher the frequency resolution we can



achieve.[192]

$$f \propto \frac{1}{T} \quad (6.34)$$

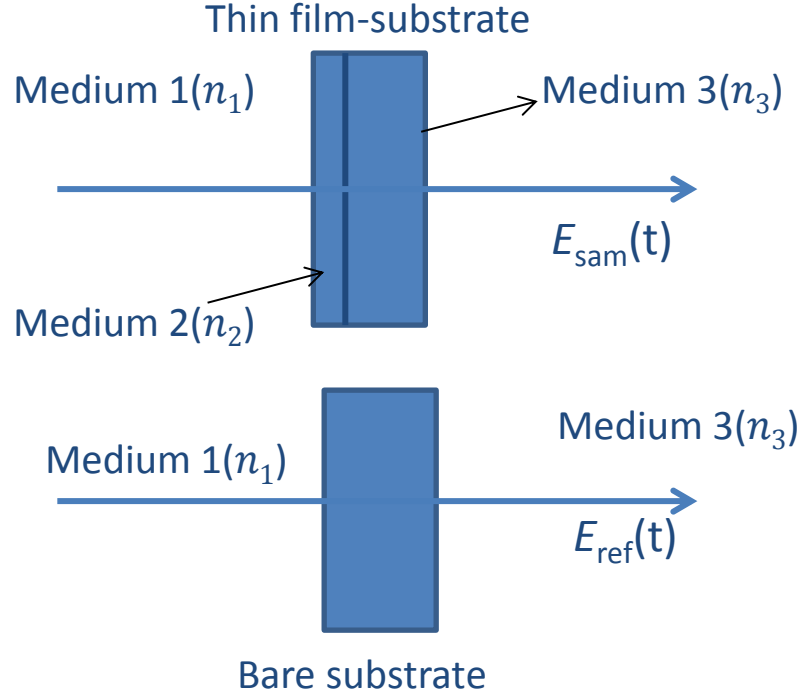


Figure 6.11: Schematic diagram of sample-reference measurement. Here film on substrate represents sample and bare substrate represents reference.

Figure 6.11 is the schematic representation of propagation of a THz pulse through sample and reference. The extraction of dielectric properties of the sample such as refractive index, power absorption coefficient, are performed in frequency-domain, which is done using Fourier transformation. We have denoted the Fourier transforms of the measured time profiles of the pulse transmitted through the sample and the reference pulse as  $E_{sam}^*(\omega)$  and  $E_{ref}^*(\omega)$  respectively. The detected signal propagated through sample and reference have complex form. Then the complex transmittance of the sample is,[194, 195, 196]

$$T^*(\omega) = |T(\omega)|e^{i\phi(\omega)} = \frac{E_{sam}^*(\omega)}{E_{ref}^*(\omega)} \quad (6.35)$$

The Fresnel transmission coefficient ( $t_{ij}$ ) and reflection coefficient ( $r_{ij}$ ) at normal incidence are given by,

$$t_{ij} = \frac{2\tilde{n}_i}{\tilde{n}_i + \tilde{n}_j} \quad (6.36)$$

$$r_{ij} = \frac{\tilde{n}_i - \tilde{n}_j}{\tilde{n}_i + \tilde{n}_j} \quad (6.37)$$

where the subscripts  $i$  and  $j$  represent the respective medium. The propagation factor  $P(\omega, d)$  is,

$$P(\omega, d) = \exp(i \frac{\tilde{n}(\omega)}{c} d) \quad (6.38)$$

, and a Fabry-Perot term  $F_{iji}$  describing the reflections within the slab is,

$$F_{iji}(\omega) = \sum_{p=0}^P [r_{ji}^2 \exp(i \frac{2\tilde{n}(\omega)}{c} d)]^p \quad (6.39)$$

where the upper limit  $P$  of the Fabry-Perot series is set by the number of total internal reflections recorded in the time-domain data. For an optically thin film, ( $P = \infty$ ), the Fabry-Perot term becomes

$$FP_{iji} = \sum_{p=0}^{\infty} [r_{ij}^2 e^{2i\tilde{n}\omega\delta/c}]^p = \frac{1}{1 - r_{ij}^2 e^{2i\tilde{n}\omega\delta/c}} \quad (6.40)$$

Then,

$$E_{sam}(\omega) = \eta(\omega).T_{12}(\omega).P_2(\omega, d).T_{23}(\omega).FP(\omega).E(\omega) \quad (6.41)$$

$$E_{ref}(\omega) = \eta(\omega).T_{13}(\omega).P_3(\omega, d_r).T_{31}(\omega).FP(\omega).E(\omega) \quad (6.42)$$

where,  $E(\omega)$  is the incident THz wave and all the reflection, transmission and propagation coefficients in these media are included in the  $\eta(\omega)$ .

The refractive index of the sample is given by the phase of the complex trans-

mission,

$$n(\omega) = 1 + \frac{c}{\omega d} \phi(\omega), \quad (6.43)$$

and the absorption coefficient is

$$\alpha(\omega) = -\frac{2}{d} \ln \left| \frac{T(\omega)}{t_{ij} t_{ji}} \right| \quad (6.44)$$

Solving these equations, we get the transmission coefficient of the film as,

$$T(\omega) = \frac{\tilde{n}_3 + 1}{\tilde{n}_3 + 1 - i\omega d(\tilde{n}_3 + \tilde{\epsilon})/c} \exp\left(i \frac{\omega(d_s - d_r)(\tilde{n}_3 - 1)}{c}\right) \quad (6.45)$$

# Chapter 7

## THz time-domain spectroscopy (THz-TDS) study of $\text{NiCo}_2\text{O}_4$

### 7.1 Introduction

We use terahertz time-domain spectroscopy (THz-TDS) to determine the character of electronic transport in two  $\text{NiCo}_2\text{O}_4$  films grown at 300°C and 500°C, which we label NCO300 and NCO500. The NCO300 film undergoes a metal-insulator transition (MIT,  $T_{\text{MIT}} = 300\text{K}$ ) and ferrimagnetic ordering at the same temperature ( $T_c = 300\text{K}$ ). The NCO500 film possesses a much higher resistivity than NCO300 at room temperature and shows neither a metallic behavior in DC transport nor any appreciable magnetism.[82] In spite of the significant differences in resistivity and magnetic properties between the two films, we find a remarkable similarity in the character of transport in the two films - both films show band-like coherent transport at intermediate temperatures(70-300 K). By contrast, previous studies of NCO reported p-type thermally-activated hopping conductivity, most likely due to the polycrystallinity of the samples they used.[15, 16, 17] The present spectroscopic confirmation of the band-like transport is significant for the prospective applications of  $\text{NiCo}_2\text{O}_4$  as a transparent conducting oxide and further optimization of its functionality. The

bandlike conduction in NCO500 happens with a much lower carrier density, which we attribute to the different cation distributions in the two films: the more perfect inverse spinel structure in the NCO500 film provides a much lower level of carrier doping. In both NCO300 and NCO500 films, we find a crossover from coherent to incoherent transport below  $\sim 70$  K, which indicates the tendency of carriers toward localization. We suggest that this tendency results from disorder-induced localization effects,[92] reminiscent of the localization tendencies found in magnetoresistive manganites[197, 198, 119, 117, 199] and in Zn-doped cuprates.[200]

## 7.2 Experimental Methods

The NCO samples used in this study are 300 nm epitaxial thin films on spinel  $\text{MgAl}_2\text{O}_4(001)$  substrates grown by pulsed laser deposition at substrate temperatures of  $300^\circ\text{C}$  and  $500^\circ\text{C}$  and 50 mT  $\text{O}_2$  pressure inside the chamber. The thicknesses of the films were estimated from the thickness calculated from X-ray reflectivity scans on a set of thinner NCO films. The structural properties were analyzed using four-circle high resolution X-ray diffraction. The lattice constant along the  $c$  axis calculated from the vertical position of the (226) peak in reciprocal space mapping (RSM) scans for the NCO500 films is  $8.50 \text{ \AA}$ , which is larger than  $8.17 \text{ \AA}$  of the NCO300 film and than the bulk value ( $8.116 \text{ \AA}$ ). Both films are fully strained and have same in-plane lattice constant (calculated from the horizontal (226) RSM peak position) as the  $\text{MgAl}_2\text{O}_4$  substrate ( $8.083 \text{ \AA}$ ). The full width at half maxima of the (004) peaks are  $0.008^\circ$  (NCO300) and  $0.02^\circ$  (NCO500), indicating the good crystalline quality of the films. The measurement of magnetic properties using a superconducting quantum interference device magnetometer and the resistivity measurement using a standard 4-probe method reported earlier showed ferrimagnetic behavior accompanied by metallicity for NCO300, while the NCO500 film showed insulating behavior with reduced magnetic

moment.[82] Hall resistivity measured with the magnetic field applied in a direction perpendicular to the film surface showed p-type conductivity.[201]

THz-TDS was performed using a home-built spectrometer based on a 1-kHz repetition rate regenerative Ti:Sapphire laser amplifier shown in fig.6.8 and a commercial spectrometer made by Teraview.[202] Both spectrometers are equipped with He flow cryostats that allow sample temperature control in the 4-320 K range. The two instruments produced identical spectroscopic data on the studied  $\text{NiCo}_2\text{O}_4$  films.

THz-TDS allows the measurement of the complex frequency-dependent dielectric function  $\epsilon(\omega)$  (or equivalently, the optical conductivity  $\sigma(\omega)$ ) of a thin film on a substrate, which is accomplished by measuring the electric field of coherent THz pulses transmitted through the sample,  $E_{sam}(t)$ , and through the reference,  $E_{ref}(t)$ . In thin film studies, we take the reference to be a bare wafer of the same material as the film substrate and of similar thickness. Then, we compute the amplitude transmission coefficient as

$$\tilde{t} = \frac{\tilde{E}_{sam}(\omega)}{\tilde{E}_{ref}(\omega)} \quad (7.1)$$

, where  $\tilde{E}_{sam}(\omega)$  and  $\tilde{E}_{ref}(\omega)$  are Fourier transforms of the time-dependent quantities  $E_{sam}(t)$  and  $E_{ref}(t)$ . The transmission coefficient of the film is determined by its dielectric function  $\tilde{\epsilon}(\omega)$  and the refractive index  $\tilde{n}_3(\omega)$  of the substrate via the relation

$$\tilde{t} = \frac{\tilde{n}_3 + 1}{\tilde{n}_3 + 1 - i\omega d(\tilde{n}_3 + \tilde{\epsilon})/c} \exp(i\frac{\omega(d_s - d_r)(\tilde{n}_3 - 1)}{c}) \quad (7.2)$$

, where  $d$  is the thickness of the film, and  $d_s$  and  $d_r$  are the thicknesses of the film substrate and of the bare reference wafer. Equation (4) accounts for multiple reflections of the THz pulse inside the film but assumes that the first and all subsequent reflections in both sample and reference substrates have been windowed out.[195] The substrate thicknesses are typically measured by a precision micrometer with 1

$\mu m$  accuracy. The refractive index  $n_3(\omega)$  of the substrate is measured in a separate THz-TDS measurement with free space as the reference. Fig. 7.1 shows the temperature dependence of the dielectric function of the NCO300 film calculated from the transmission  $t(\omega)$  using Eq. (7.2). We interpret the measured dielectric function using the free-electron model of Paul Drude[194], which is written as

$$\epsilon(\omega) = \epsilon_\infty - \frac{\omega_P^2}{\omega^2 + i\omega\gamma_D} \quad (7.3)$$

, where  $\epsilon_\infty$  is the high frequency dielectric constant contributed by bound electrons and by high-frequency phonons. The second term in Eq. (7.3) is the contribution of free electrons for which  $\gamma_D$  is the relaxation rate. The plasma frequency is determined by the free carrier density  $N$  via the relation  $\omega_P^2 = \frac{Ne^2}{m^*\epsilon_0}$ , where  $\epsilon_0$  is the free space permittivity and  $m^*$  is the effective mass. The Drude conductivity is then calculated as

$$\sigma(\omega) = \frac{\sigma_0}{1 - i\frac{\omega}{\gamma_D}} \quad (7.4)$$

, where  $\sigma_0 = \frac{\omega_P^2\epsilon_0}{\gamma_D}$  is the DC conductivity of the film.

### 7.3 Spectroscopy of low-temperature-grown NiCo<sub>2</sub>O<sub>4</sub>

The NCO300 film studied here displays a MIT at  $T_{MIT} = 270$  K and undergoes ferrimagnetic ordering at the same temperature.[82] The film shows metallic behavior in the 70-300 K range where its resistivity decreases with lowering temperature. Upon further cooling, the film shows an upturn in resistivity around 50-70 K that was attributed to charge carrier localization. The present spectroscopic work was performed on a NCO300 film prepared under the same conditions as in reference.[82]

Figure 7.1 shows the measured real and imaginary parts of the dielectric function  $\epsilon(\omega)$  at various temperatures and Fig. 7.2 displays the temperature de-

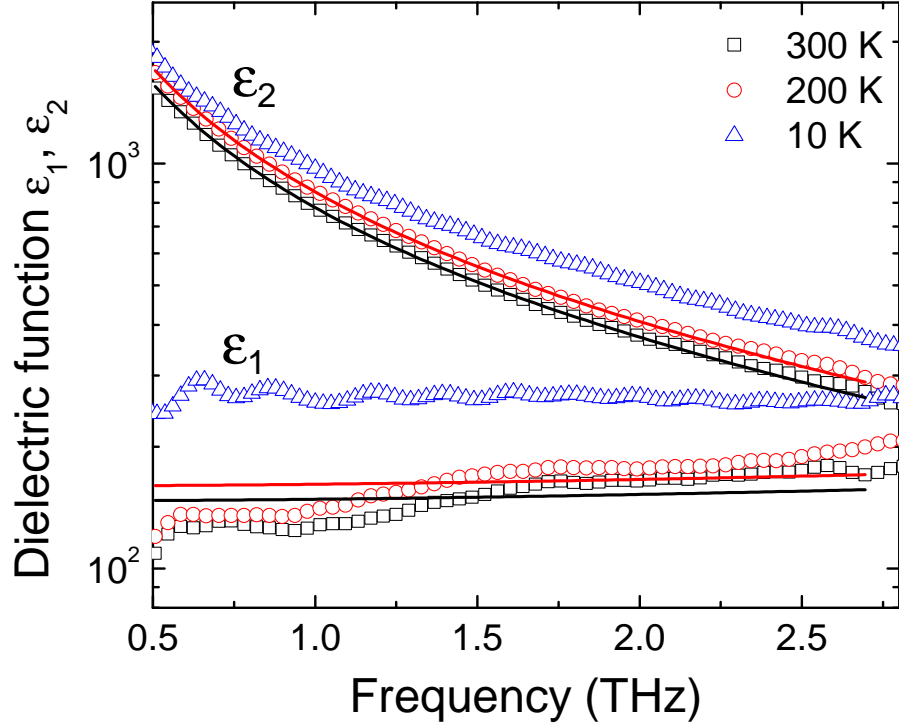


Figure 7.1: The real ( $\epsilon_1$ ) and imaginary ( $\epsilon_2$ ) parts of the measured dielectric function of the NCO300 film. Solid lines represent Drude model fits using Eq. (7.3).

pendence of the Drude model parameters (Eqs. (7.3) and (7.4)) determined from the least-square fits of  $\epsilon(\omega)$ . The temperature dependence of  $\sigma_0$  follows that of the DC transport conductivity[82], displaying the MIT at 270 K and carrier localization below 70 K. To the best of our knowledge, the metallic behavior in the intermediate 70-300 K range has only been reported in the epitaxial NCO films.[82] In other  $\text{NiCo}_2\text{O}_4$  specimens, e.g., sputtered polycrystalline films, the observed conduction showed resistive temperature-activated behavior that was attributed to small polaron hopping.[16, 17, 203]

We gain further insight into the nature of the metallic state in the intermediate temperature range from the observed frequency dependence of optical conductivity (Fig. 7.3), which follows well the Drude model dependence. At low temperatures below 50 K and at high temperatures above 300 K, we find a transfer of spectral weight



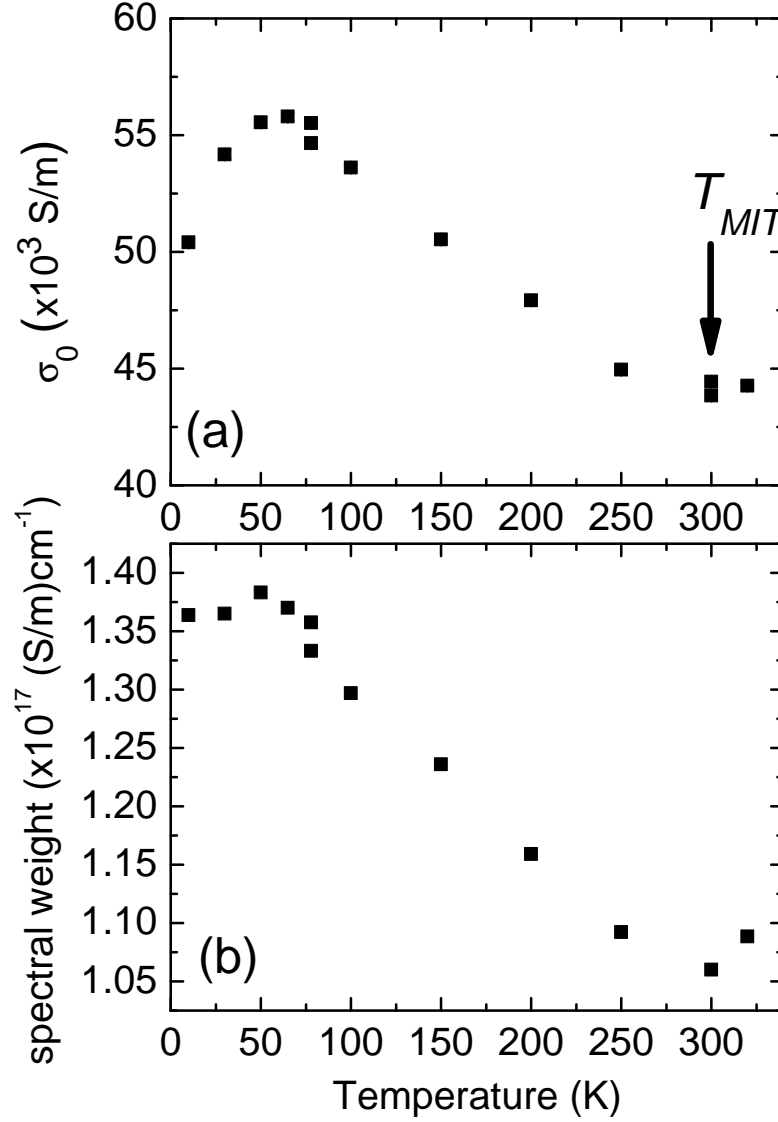


Figure 7.2: NCO300: (a) The temperature dependence of the DC conductivity  $\sigma_0$ . (b) The temperature dependence of the THz spectral weight.

from the zero-frequency Drude peak to higher frequencies, which leads to suppressed DC conductivity. The coherent Drude transport at intermediate temperatures is consistent with band-like conduction as opposed to the incoherent hopping of small polarons.[16, 17, 204] This band-like Drude conductivity and the positive sign of Hall resistivity in the NCO300 film[201] favor the cation valency models that allow the formation of p-type conduction bands, i.e., our observations are consistent with the

mixed-valence descriptions proposed by Battle[19] and Marco[2] (Fig.2.2 shown in chapter 2).

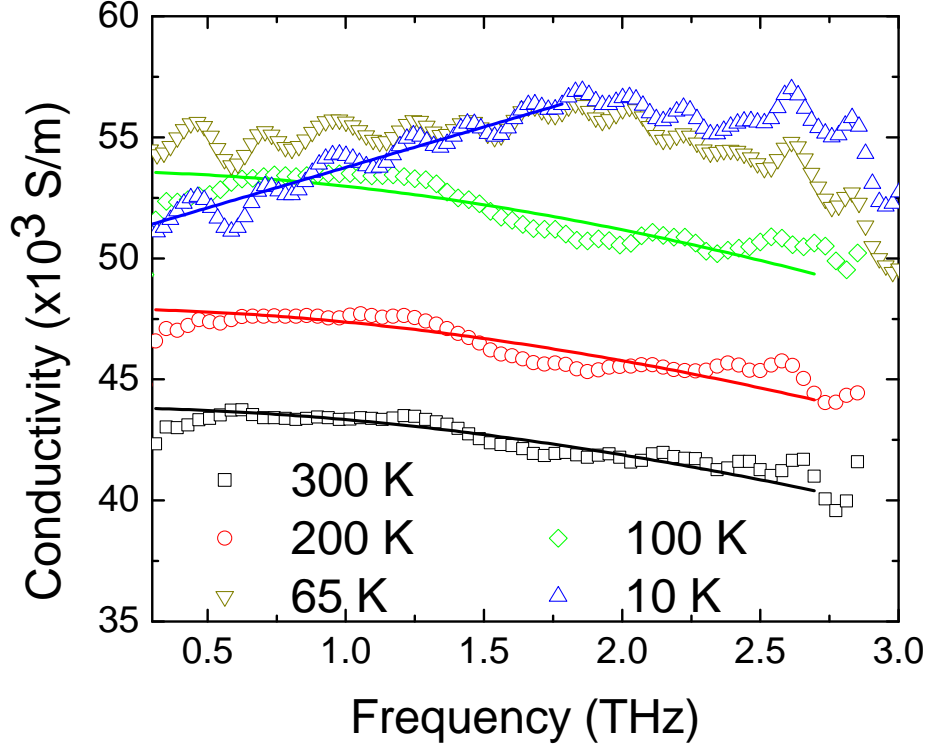


Figure 7.3: The real part of the THz optical conductivity of the NCO300 film. The solid lines illustrate the extrapolation to find the DC conductivity  $\sigma_0$ . The solid lines at 100-300 K follow the Drude model of Eq. (7.4).

In the intermediate temperature range, we observe a temperature-independent scattering rate (Figs. 7.2(c) and 7.3). This peculiar observation provides further clues about the nature of transport in NCO300. Since phonon scattering rates are strongly temperature dependent[86], we infer that phonon collisions do not play the dominant role in scattering. We can also rule out spin fluctuations as a significant source of scattering: in NCO300, ferrimagnetic ordering sets in at  $T_c = 270$  K, which means that the spin fluctuations change in strength significantly in this temperature region. The temperature-independent scattering rate must result from a static disorder, i.e., defects and/or impurities.

The MIT (Fig. 7.2) is accompanied by the magnetic phase transition into

ferrimagnetically ordered state, which signifies a close relationship between magnetic and transport properties in the material. A comparison of the room-temperature resistivity of  $\text{NiCo}_2\text{O}_4$  films grown at different temperatures with the measured low-temperature saturation magnetization showed that with increasing synthesis temperature the films become both highly resistive and nonmagnetic.[82] The application of magnetic field of 1 T resulted in a small negative magnetoresistance -2% [82] in NCO300 and a slight increase in  $T_c$ . This phenomenology resembles the MIT transition and ferromagnetic ordering in colossal magnetoresistance manganites[205], where the double-exchange physics is responsible for the phase transitions. Another similarity is found by comparing the temperature dependence of the Drude parameters  $\omega_p^2$  and  $\gamma_D$  in manganites[206, 207] and in NCO300. The scattering rate  $\gamma_D$  in the manganites is weakly temperature dependent near the phase transition temperature ( $T_c \approx 300\text{K}$ ) and is independent of temperature below  $\sim 100\text{K}$ , while  $\omega_p^2$  strongly increases with lowering temperature from  $T_c$  down to the lowest temperatures.[206, 207] It is this drastic rise in the carrier density and in  $\omega_p^2$  that governs the metallic state and its temperature evolution in the manganites. We see a similar behavior in NCO300 (Figs. 7.2(b),(c)), where the scattering rate stays constant and the metallicity is determined by the rising  $\omega_p^2$  as the temperature is lowered. We suggest that the similarity results from the double-exchange physics being important for the MIT in NCO300. In the manganites, the double exchange and ferromagnetism facilitate the hopping and make the materials metallic. Unlike the manganites, NCO300 experiences ferrimagnetic ordering between the A- and B-site sublattices. The models of Battle and Marco both require a flip of the carrier spin for the hopping between overlapping bands of Co and Ni cations (Fig. 2.2). The double-exchange and ferrimagnetic ordering hinder the hopping between the cations. And yet, the NCO300 becomes metallic upon the ferrimagnetic ordering. This observation leads us to suggest that the transport in

NCO300 may be dominated by the hopping between the cations of the same species and the same spin direction in the ferrimagnetic state, for example, the hopping only between the A-site Co cations or only between the B-site Ni cations in the Battle model. Such transport would result in spin-polarized currents, making  $\text{NiCo}_2\text{O}_4$  a candidate for a spin injection material.

## 7.4 Spectroscopy of high-temperature-grown $\text{NiCo}_2\text{O}_4$

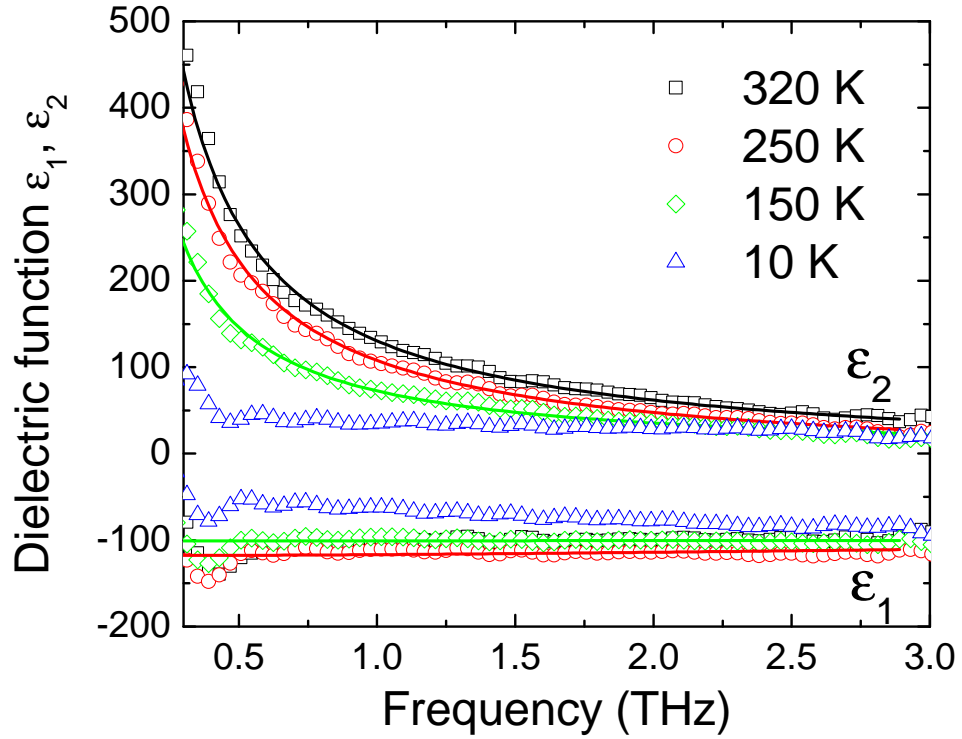


Figure 7.4: The real ( $\epsilon_1$ ) and imaginary ( $\epsilon_2$ ) parts of the measured dielectric function of the NCO500 film. Solid lines represent Drude model fits using Eq. (7.3).

The high-temperature grown NCO500 film shows monotonic increase in resistivity during cooling from 400 to 2 K with no MIT and no magnetic order[82], with its room-temperature resistivity being six times higher than that of the NC300 film (Figs. 7.3 and 7.6). The absence of MIT is not surprising given its double-exchange nature in NCO300 and the absence of magnetic order in NCO500. Figure 7.4 shows

the measured dielectric function of NCO500 at several temperatures. At all temperatures, the dielectric function and its frequency dependence are reminiscent of a metal, with a large imaginary part that is responsible for the absorption at THz frequencies. At the same time, the imaginary part is strongly suppressed compared to NCO300 (Fig. 7.1), as expected from a more resistive film. At temperatures above 150 K, the dielectric function is well described by the Drude model (Figs. 7.4 and 7.6) with the parameters shown in Fig. 7.5. This behavior points to coherent transport that is very similar to that of the NCO300 film (Fig. 7.3) with almost identical scattering rates in the 150-300 K temperature range. The band-like coherent transport is then a shared feature of the two materials and the similar scattering rates must result from similar scattering mechanisms, i.e., the scattering in NCO500 is also dominated by defects.

The difference in the measured conductivity between the films is governed by the differing carrier densities in the bands formed by the cation level overlap in the Battle and Marco models. In both models, the carrier density and the saturation magnetization depend on the valency of the Ni and Co cations (Fig. 2.2). The low carrier density in NCO500 is accompanied by the strongly suppressed low-temperature magnetization.[82] In the Battle model, Eq. (2.1), the magnetization is suppressed when the parameter  $\delta$  is equal or close to 0. In this case, the A-site Co cations acquire the 3+ valency and the  $d^6$  configuration and the B-site Ni cations acquire the 2+ valency ( $d^8$ ). The saturation magnetization in the Battle model can also be lowered by reducing the presence of the A-site Ni, i.e., by reducing the parameter  $z$  in Eq. (2.1). The modification of the Ni and Co valencies with  $\delta = 0$  and the reduced A-site Ni density correspond to a more perfect inverse spinel with the structural formula  $\text{Co}^{3+}[\text{Co}^{3+}\text{Ni}^{2+}]\text{O}_4^{2-}$ . The higher growth temperature of NCO500 may be promoting the more perfect inverse spinel, in which one hole occupies the A-site  $\text{Co}^{3+}$  and no holes reside on the B sites. The reduced conductivity then happens only if

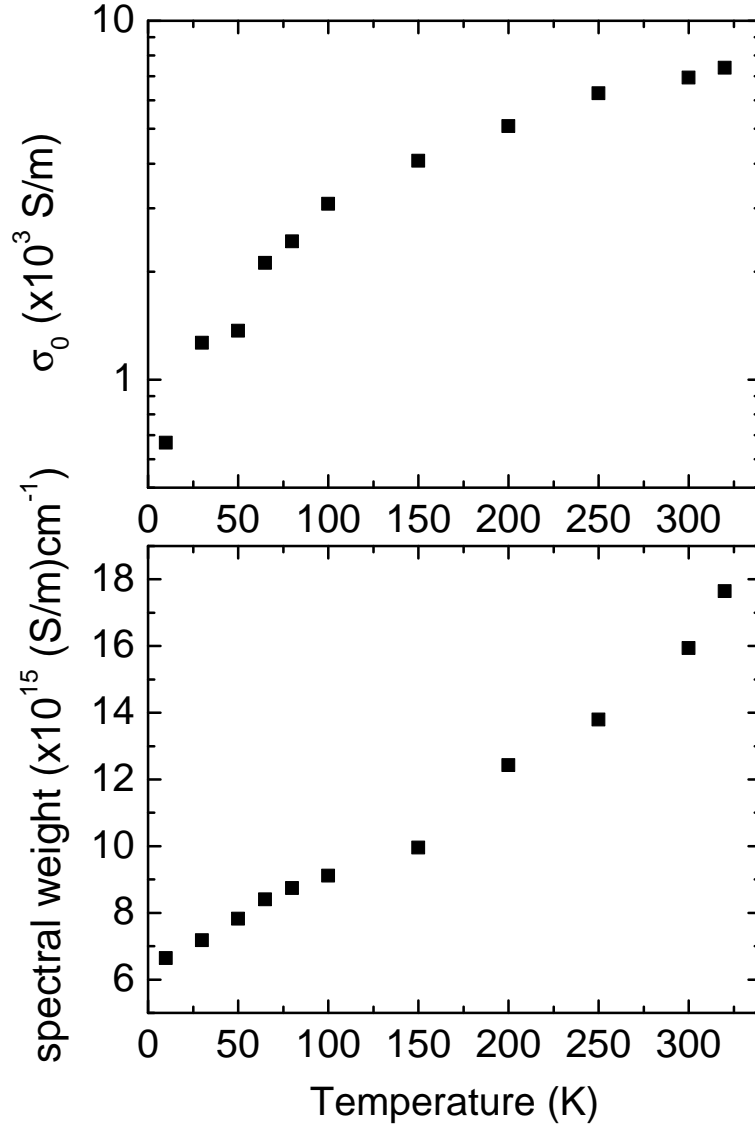


Figure 7.5: NCO500: (a) The temperature dependence of the DC conductivity  $\sigma_0$ . (b) The temperature dependence of the THz spectral weight.

the transport is dominated by the hopping through B-site Ni cations, which would be consistent with our conclusion from the previous section that transport in  $\text{NiCo}_2\text{O}_4$  happens via the cations of the same species on either A- or B- sites. The present observation allows us to be more specific and assign the transport to the B site Ni cations. We note that in this picture the absence of holes on B sites would not allow any conduction at all, so in NCO500  $\delta$  must be close to but not exactly zero to allow

some residual hole density in the overlapping bands of Fig. 2.2 and account for our observations (Figs. 7.4-7.6).

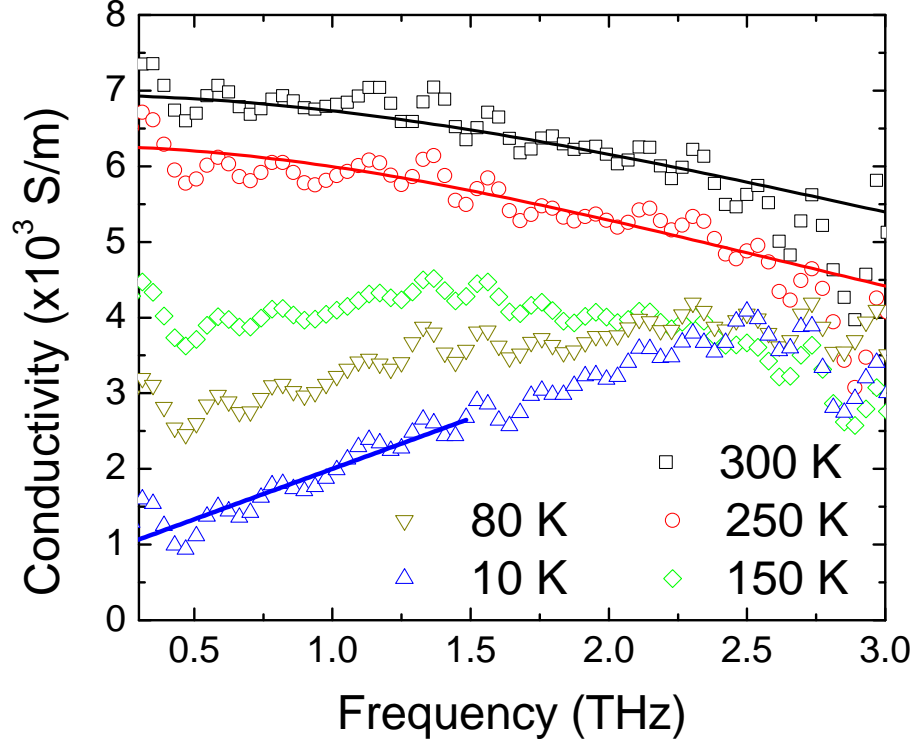


Figure 7.6: The real part of the THz optical conductivity of the NCO500 film. The solid lines illustrate the extrapolation to find the DC conductivity  $\sigma_0$ . The solid lines at 250 and 300 K follow the Drude model of Eq. (7.4).

In the Marco model of Eq. (2.2), the suppressed saturation magnetization is achieved by setting the valencies of B-site Co and Ni to 2+ and 4+ ( $d^7$  and  $d^6$  configurations), respectively. The B-site  $\text{Co}^{2+}$  cations accommodate one hole at the Fermi level (Fig. 2.2) and the  $\text{Ni}^{4+}$  cations possess a completely full hole band that does not allow conduction. As in the Battle model, we have to assign transport to a single species of B-site cations, namely the  $\text{Ni}^{4+}$ , to account for the reduced carrier density in NCO500, which again would be consistent with the observation of the double-exchange-driven metal-insulator transition (MIT) in NCO300.

At low temperatures, the NCO300 and NCO500 films share a similarity - they

both display a tendency toward localization. The conductivity of NCO300 is reduced with temperature below 70 K (Fig. 7.2(a)), while the conductivity of NCO500 exhibits a much sharper decrease below 100 K (Fig.1.5(a)), a behavior that agrees with the earlier DC transport study.[82] More significantly, both materials undergo a drastic transition from coherent band-like to incoherent transport. This is illustrated by the spectra of the real part of optical conductivity, where the zero-frequency Drude peak slowly shifts to a higher frequency (Figs. 7.3 and 7.6). This results in optical conductivity that increases with frequency, which signifies an activated hole mobility with holes needing to overcome a potential barrier for hopping.[208] At first glance, the observed low-temperature activated mobility is consistent with the reports of small polaron hopping conductivity in the spinels NCO and  $\text{Co}_3\text{O}_4$ [15, 16, 17, 209] and with the optical signature of polaronic hopping transport, which includes a high-frequency absorption band.[204, 210] This absorption band corresponds to the transfer of the small polaron from one localized site to an adjacent localized site. However, we believe that a crossover to the polaronic hopping transport in our films would be accompanied by a drastic change of the band filling (or carrier density) and of the cation valency. The change of cation valency would alter the saturation magnetization in NCO300, which does not take place, as we observe no low-temperature change in magnetization apart from the expected meanfield-like saturation.[82] Any large change in the carrier density would modify the strength of the Drude peak - the integral under the Drude curve. Such modification is not found in our low-temperature spectra (Figs. 7.3 and 7.6), where instead of diminishing in strength, the Drude peak slowly shifts to higher frequencies. Therefore, we propose that the localization tendency in our  $\text{NiCo}_2\text{O}_4$  films is different from the polaronic transport picture reported in earlier work on spinels.[15, 16, 17, 209, 210] Our study does not provide enough information to determine the exact nature of the observed localization.



## 7.5 Summary

We presented a THz spectroscopic study of epitaxial films of the mixed-valence inverse spinel NCO. The oxidation states of Ni and Co cations in this material have long been the subject of inquiry. The models proposed in late 1970s ([19] and more recently([2]) predicted metallic band-like transport in  $\text{NiCo}_2\text{O}_4$  that has not been reported in the material until the epitaxial films were synthesized.[82] The measurement of real and imaginary parts of the dielectric function (optical conductivity) allowed us to elucidate the details of electronic conduction in  $\text{NiCo}_2\text{O}_4$ . We examined two kinds of films: low-temperature grown metallic NCO300 and high-temperature grown insulating NCO500. The NCO300 film also undergoes a MIT at  $T_{\text{MIT}} = 270$  K with concomitant ferrimagnetic ordering, while the NCO500 film is insulating at all temperatures with no magnetic order. Based on spectroscopic similarities with colossal magneto-resistance manganites, we propose that the MIT in NCO300 is governed by the double-exchange interaction. No MIT is found in NCO500. Both films exhibit coherent Drude-type conduction at intermediate temperatures, according to the measured conductivity spectra, which is consistent with the models of Battle and Marco. We also find that both films undergo a crossover to incoherent transport at low temperatures, which indicates a strong tendency toward localization. We rule out a crossover to small polaron hopping reported in earlier works on  $\text{NiCo}_2\text{O}_4$ [15, 16, 17] as the cause of the localization tendencies and suggest that another mechanism must be at work in the studied  $\text{NiCo}_2\text{O}_4$  films.

## References

- [1] Kodama, T., et al., “Co<sub>2</sub> decomposition to carbon with ferrite-derived metallic phase at 300°C”, *Carbon* **33** (1995), no. 10, 1443–1447.
- [2] Marco, J. F., et al., “Cation distribution and magnetic structure of the ferromagnetic spinel nico<sub>2</sub>o<sub>4</sub>”, *Journal of Materials Chemistry* **11** (2001), no. 12, 3087–3093.
- [3] Anderson, R. M., et al., “Faraday rotation in co<sub>0.85</sub>zn<sub>0.15</sub>fe<sub>2</sub>o<sub>4</sub> spinel ferrite nanoparticulate films under low applied fields”, *Applied physics letters* **84** (2004), no. 16, 3115–3117.
- [4] Van der Zaag, P., J. Ruigrok, and M. Gillies, “New options in thin film recording heads through ferrite layers”, *Philips journal of research* **51** (1998), no. 1, 173–195.
- [5] Kim, J.-G., et al., “Analysis of the nico<sub>2</sub>o<sub>4</sub> spinel surface with auger and x-ray photoelectron spectroscopy”, *Applied surface science* **165** (2000), no. 1, 70–84.
- [6] Bakuzis, A., et al., “Magneto-optical properties of a highly transparent cadmium ferrite-based magnetic fluid”, *Applied physics letters* **84** (2004), no. 13, 2355–2357.
- [7] Zheng, H., et al., “Multiferroic batio<sub>3</sub>-cofe<sub>2</sub>o<sub>4</sub> nanostructures”, *Science* **303** (2004), no. 5658, 661.
- [8] Bichurin, M., et al., “Resonance magnetoelectric effects in layered magnetostrictive-piezoelectric composites”, *Physical Review B* **68** (2003), no. 13, 132408.
- [9] Suzuki, Y., et al., “Biological application of fast-scanning atomic force microscopy”, *Scanning Probe Microscopy in Nanoscience and Nanotechnology 2*, Springer, 2011, p. 217.

- [10] Sun, Q.-C., et al., “Optical band gap hierarchy in a magnetic oxide: Electronic structure of  $\text{NiFe}_2\text{O}_4$ ”, *Phys. Rev. B* **86** (2012), 205106.
- [11] Foerster, M., et al., “Tunnel transport through  $\text{CoFe}_2\text{O}_4$  barriers investigated by conducting atomic force microscopy”, *Journal of Physics D: Applied Physics* **43** (2010), no. 29, 295001.
- [12] Luders, U., et al., “Spin filtering through ferrimagnetic  $\text{NiFe}_2\text{O}_4$  tunnel barriers”, *Applied physics letters* **88** (2006), no. 8, 082505–082505.
- [13] Ramos, A. V., et al., “Room temperature spin filtering in epitaxial cobalt-ferrite tunnel barriers”, *Applied Physics Letters* **91** (2007), no. 12, –.
- [14] Haenen, J., W. Visscher, and E. Barendrecht, “Characterization of  $\text{NiCo}_2\text{O}_4$  electrodes for  $\text{O}_2$  evolution: Part i. electrochemical characterization of freshly prepared  $\text{NiCo}_2\text{O}_4$  electrodes”, *Journal of electroanalytical chemistry and interfacial electrochemistry* **208** (1986), no. 2, 273–296.
- [15] Windisch Jr, C., et al., “Infrared transparent spinel films with p-type conductivity”, *Thin Solid Films* **398** (2001), 45–52.
- [16] Exarhos, G. J., et al., “Cation defects and conductivity in transparent oxides”, *Applied Physics A* **89** (2007), no. 1, 9–18.
- [17] Windisch Jr, C. F., et al., “Conducting spinel oxide films with infrared transparency”, *Thin Solid Films* **420** (2002), 89–99.
- [18] Holgersson, S. and A. Karlsson, “Über einige neue kobaltite vom spinelltypus”, *Zeitschrift für anorganische und allgemeine Chemie* **183** (1929), no. 1, 384.
- [19] Battle, P., A. Cheetham, and J. Goodenough, “A neutron diffraction study of the ferrimagnetic spinel  $\text{NiCo}_2\text{O}_4$ ”, *Materials Research Bulletin* **14** (1979), no. 8, 1013–1024.
- [20] Serebrennikova, I. and V. Birss, “Structural and compositional properties of sol-gel formed  $\text{Ni}$ ,  $\text{Co}$  and  $\text{Ni-Co}$  oxide films”, *Journal of materials science* **36** (2001), no. 18, 4331–4343.
- [21] El Baydi, M., et al., “High specific surface area nickel mixed oxide powders  $\text{LaNiO}_3$  (perovskite) and  $\text{NiCo}_2\text{O}_4$  (spinel) via sol-gel type routes for oxygen electrocatalysis in alkaline media”, *Journal of Solid State Chemistry* **116** (1995), no. 1, 157–169.

- [22] Singh, N., J. Singh, and R. Singh, “Sol–gel-derived spinel  $\text{Co}_3\text{O}_4$  films and oxygen evolution: Part ii. optimization of preparation conditions and influence of the nature of the metal salt precursor”, *International journal of hydrogen energy* **27** (2002), no. 9, 895–903.
- [23] Švegl, F., et al., “Characterization of spinel  $\text{Co}_3\text{O}_4$  and li-doped  $\text{Co}_3\text{O}_4$  thin film electrocatalysts prepared by the sol–gel route”, *Electrochimica acta* **45** (2000), no. 25, 4359–4371.
- [24] Guan, H., et al., “Fabrication of  $\text{NiCo}_2\text{O}_4$  nanofibers by electrospinning”, *Solid state communications* **131** (2004), no. 2, 107–109.
- [25] Fazle Kibria, A. and S. Tarafdar, “Electrochemical studies of a nickel–copper electrode for the oxygen evolution reaction (oer)”, *International journal of hydrogen energy* **27** (2002), no. 9, 879–884.
- [26] Jiang, Y., et al., “Moderate temperature synthesis of nanocrystalline  $\text{Co}_3\text{O}_4$  via gel hydrothermal oxidation”, *Materials chemistry and physics* **74** (2002), no. 2, 234–237.
- [27] Wu, G., et al., “Anodically electrodeposited  $\text{Co}+\text{Ni}$  mixed oxide electrode: preparation and electrocatalytic activity for oxygen evolution in alkaline media”, *Journal of Solid State Chemistry* **177** (2004), no. 10, 3682–3692.
- [28] Castro, E., S. Real, and L. Pinheiro Dick, “Electrochemical characterization of porous nickel–cobalt oxide electrodes”, *International journal of hydrogen energy* **29** (2004), no. 3, 255–261.
- [29] Chi, B., et al., “Effect of precipitant on preparation of  $\text{Ni-Co}$  spinel oxide by coprecipitation method”, *Materials Letters* **58** (2004), no. 9, 1415–1418.
- [30] Bocca, C., et al., “Nickel–cobalt oxide-coated electrodes: influence of the preparation technique on oxygen evolution reaction (oer) in an alkaline solution”, *International journal of hydrogen energy* **24** (1999), no. 1, 21–26.
- [31] Bocca, C., et al., “Oxygen evolution on  $\text{Co}_3\text{O}_4$  and li-doped  $\text{Co}_3\text{O}_4$  coated electrodes in an alkaline solution”, *International journal of hydrogen energy* **24** (1999), no. 8, 699–707.
- [32] Patil, P. S., “Versatility of chemical spray pyrolysis technique”, *Materials Chemistry and physics* **59** (1999), no. 3, 185–198.
- [33] Hamdani, M., et al., “Physicochemical and electrocatalytic properties of  $\text{Li-Co}_3\text{O}_4$  anodes prepared by chemical spray pyrolysis for application in alkaline water electrolysis”, *Electrochimica acta* **49** (2004), no. 9, 1555–1563.

- [34] Boggio, R., A. Carugati, and S. Trasatti, "Electrochemical surface properties of  $\text{Co}_3\text{O}_4$  electrodes", *Journal of applied electrochemistry* **17** (1987), no. 4, 828–840.
- [35] Da Silva, L., L. De Faria, and J. Boodts, "Electrochemical impedance spectroscopic investigation of the deactivation mechanism, surface and electrocatalytic properties of  $\text{Ti}/\text{RuO}_2(x) + \text{Co}_3\text{O}_4(1-x)$  electrodes", *Journal of Electroanalytical Chemistry* **532** (2002), no. 1, 141–150.
- [36] Tavares, A., et al., "Electrochemical study of spinel oxide systems with nominal compositions  $\text{Ni}_{1-x}\text{Cu}_x\text{Co}_2\text{O}_4$  and  $\text{NiCo}_{2-y}\text{Cu}_y\text{O}_4$ ", *Journal of Solid State Electrochemistry* **5** (2001), no. 1, 57–67.
- [37] Hamdani, M., R. Singh, and P. Chartier, "Co<sub>3</sub>O<sub>4</sub> and Co-based spinel oxides bifunctional oxygen electrodes", *Int. J. Electrochem. Sci* **5** (2010), 556–577.
- [38] Kitao, M., et al., "Preparation and electrochromic properties of rf-sputtered  $\text{NiO}_x$  films prepared in  $\text{Ar}/\text{O}_2/\text{H}_2$  atmosphere", *Japanese journal of applied physics* **33** (1994), 6656–6656.
- [39] Sato, H., et al., "Transparent conducting p-type  $\text{NiO}$  thin films prepared by magnetron sputtering", *Thin solid films* **236** (1993), no. 1, 27–31.
- [40] Fujii, E., et al., "Preferred orientations of  $\text{NiO}$  films prepared by plasma-enhanced metalorganic chemical vapor deposition", *Japanese journal of applied physics* **35** (1996), 328.
- [41] Kumagai, H., et al., "Preparation and characteristics of nickel oxide thin film by controlled growth with sequential surface chemical reactions", *Journal of materials science letters* **15** (1996), no. 12, 1081–1083.
- [42] He, J., et al., "Dye-sensitized nanostructured p-type nickel oxide film as a photocathode for a solar cell", *The Journal of Physical Chemistry B* **103** (1999), no. 42, 8940–8943.
- [43] Morin, F., "Electrical properties of  $\text{NiO}$ ", *Physical Review* **93** (1954), no. 6, 1199.
- [44] Biju, V. and M. Abdul Khadar, "Dc conductivity of consolidated nanoparticles of  $\text{NiO}$ ", *Materials research bulletin* **36** (2001), no. 1, 21–33.
- [45] Parravano, G., "Thermoelectric behavior of nickel oxide", *The Journal of Chemical Physics* **23** (2004), no. 1, 5–10.
- [46] Sanz, J., et al., "Electronic structure and chemical characterization of ultrathin insulating films", *Thin Solid Films* **332** (1998), no. 1, 209–214.

- [47] Snowden, D. and H. Saltsburg, “Hopping conduction in nio”, *Physical Review Letters* **14** (1965), no. 13, 497.
- [48] Belova, I., et al., “Co (iii) ions high-spin configuration in nonstoichiometric  $\text{Co}_3\text{O}_4$  films”, *Solid State Communications* **47** (1983), no. 8, 577 – 584.
- [49] Yamamoto, H., S. Tanaka, and K. Hirao, “Effects of substrate temperature on nanostructure and band structure of sputtered  $\text{Co}_3\text{O}_4$  thin films”, *Journal of applied physics* **93** (2003), no. 7, 4158–4162.
- [50] Tareen, J., et al., “Growth and electrical properties of pure and ni-doped  $\text{Co}_3\text{O}_4$  single crystals”, *Materials research bulletin* **19** (1984), no. 8, 989–997.
- [51] Monk, P. and S. Ayub, “Solid-state properties of thin film electrochromic cobalt–nickel oxide”, *Solid State Ionics* **99** (1997), no. 1, 115–124.
- [52] Liu, Z., A. Yu, and J. Y. Lee, “Synthesis and characterization of  $\text{LiNi}_{1-x-y}\text{Co}_x\text{Mn}_y\text{O}_2$  as the cathode materials of secondary lithium batteries”, *Journal of Power Sources* **81** (1999), 416–419.
- [53] Polo da Fonseca, C., et al., “Studies of  $\text{LiCoO}_x$  thin film cathodes produced by rf sputtering”, *Journal of power sources* **81** (1999), 575–580.
- [54] Yoshimura, M., K.-S. Han, and S. Tsurimoto, “Direct fabrication of thin-film  $\text{LiNiO}_2$  electrodes in lioh solution by electrochemical–hydrothermal method”, *Solid State Ionics* **106** (1998), no. 1, 39–44.
- [55] Park, S., et al., “Transparent p-type conducting  $\text{BaCu}_2\text{S}_2$  films”, *Applied physics letters* **80** (2002), no. 23, 4393–4394.
- [56] Kuk, S. T., et al., “The formation of  $\text{LiCoO}_2$  on a nio cathode for a molten carbonate fuel cell using electroplating”, *Journal of Materials Chemistry* **11** (2001), no. 2, 630–635.
- [57] Iida, A. and R. Nishikawa, “A thin film of an ni-nio heterogeneous system for an optical recording medium”, *Japanese journal of applied physics* **33** (1994), no. part 1, 3952–3959.
- [58] Carey, M., et al., “Preparation and structural characterization of sputtered  $\text{CoO}$ ,  $\text{NiO}$ , and  $\text{Ni}_{0.5}\text{Co}_{0.5}\text{O}$  thin epitaxial films”, *Journal of materials research* **6** (1991), no. 12, 2680–2687.
- [59] Roginskaya, Y. E., et al., “Characterization of bulk and surface composition of  $\text{CoNi}_{1-x}\text{O}$  mixed oxides for electrocatalysis”, *Langmuir* **13** (1997), no. 17, 4621–4627.

- [60] Hu, C.-C. and C.-Y. Cheng, “Ideally pseudocapacitive behavior of amorphous hydrous cobalt-nickel oxide prepared by anodic deposition”, *Electrochemical and solid-state letters* **5** (2002), no. 3, A43–A46.
- [61] Goodwin-Johansson, S. H., et al., “Artificial eyelid for protection of optical sensors”, SPIE’s 7th Annual International Symposium on Smart Structures and Materials, International Society for Optics and Photonics, 2000, pp. 225–231.
- [62] Windisch, C. F., K. F. Ferris, and G. J. Exarhos, “Synthesis and characterization of transparent conducting oxide cobalt–nickel spinel films”, *Journal of Vacuum Science & Technology A: Vacuum, Surfaces, and Films* **19** (2001), no. 4, 1647–1651.
- [63] Galtayries, A. and J. Grimblot, “Formation and electronic properties of oxide and sulphide films of co, ni and mo studied by xps”, *Journal of electron spectroscopy and related phenomena* **98** (1999), 267–275.
- [64] Marco, J., et al., “Characterization of the nickel cobaltite,  $\text{nico}_2\text{o}_4$ , prepared by several methods: An xrd, xanes, exafs, and xps study”, *Journal of Solid State Chemistry* **153** (2000), no. 1, 74–81.
- [65] Verwey, E., “Electronic conduction of magnetite ( $\text{fe}_3\text{o}_4$ ) and its transition point at low temperatures”, *Nature* **144** (1939), 327.
- [66] Knop, O., et al., “Chalkogenides of the transition elements. vi. x-ray, neutron, and magnetic investigation of the spinels  $\text{co}_3\text{o}_4$ ,  $\text{nico}_2\text{o}_4$ ,  $\text{co}_3\text{s}_4$ , and  $\text{nico}_2\text{s}_4$ ”, *Canadian Journal of Chemistry* **46** (1968), no. 22, 3463–3476.
- [67] Rashkova, V., et al., “Vacuum evaporated thin films of mixed cobalt and nickel oxides as electrocatalyst for oxygen evolution and reduction”, *Electrochimica acta* **47** (2002), no. 10, 1555–1560.
- [68] Das, R., et al., “Finite size effects with variable range exchange coupling in thin-film pd/fe/pd trilayers”, *Journal of Magnetism and Magnetic Materials* **322** (2010), no. 17, 2618–2621.
- [69] Das, V. D. and D. Karunakaran, “Thermoelectric studies on semiconducting  $\text{ag}_2\text{te}$  thin films: temperature and dimensional effects”, *Physical Review B* **30** (1984), no. 4, 2036.
- [70] Samal, D., D. Venkateswarlu, and P. Anil Kumar, “Influence of finite size effect on magnetic and magnetotransport properties of thin films”, *Solid State Communications* **150** (2010), no. 13, 576–580.
- [71] Fairweather, A., F. F. Roberts, and A. J. E. Welch, “Ferrites”, *Reports on Progress in Physics* **15** (1952), no. 1, 142.

- [72] [http://en.wikibooks.org/wiki/Introduction to InorganicChemistry/Ionic and C. Solids](http://en.wikibooks.org/wiki/Introduction_to_InorganicChemistry/Ionic_and_C_Solids), “Introduction to organic chemistry”.
- [73] Carta, D., et al., “A structural and magnetic investigation of the inversion degree in ferrite nanocrystals  $m\text{Fe}_2\text{O}_4$  ( $m = \text{mn, co, ni}$ )”, *The Journal of Physical Chemistry C* **113** (2009), no. 20, 8606–8615.
- [74] Tang, J., et al., “Magnetite  $\text{Fe}_3\text{O}_4$  nanocrystals: spectroscopic observation of aqueous oxidation kinetics”, *The Journal of Physical Chemistry B* **107** (2003), no. 30, 7501–7506.
- [75] Atkins, P., *Shriver and atkins’ inorganic chemistry*, Oxford University Press, 2010.
- [76] Kim, H., et al., “Multicomponent effects on the crystal structures and electrochemical properties of spinel-structured  $\text{m}_3\text{O}_4$  ( $m = \text{fe, mn, co}$ ) anodes in lithium rechargeable batteries”, *Chemistry of Materials* **24** (2012), no. 4, 720–725.
- [77] McClure, D. S., “The distribution of transition metal cations in spinels”, *Journal of Physics and Chemistry of Solids* **3** (1957), no. 3, 311–317.
- [78] Lenglet, M., et al., “Electronic structure of  $\text{NiCo}_2\text{O}_4$  by xanes, exafs and 61 ni mössbauer studies”, *Solid State Communications* **74** (1990), no. 10, 1035–1039.
- [79] Willard, M. A., et al., “Magnetic properties of ordered and disordered spinel-phase ferrimagnets”, *Journal of the American Ceramic Society* **82** (1999), no. 12, 3342–3346.
- [80] Lotgering, F., “Ferromagnetism in spinels:  $\text{CuCr}_2\text{S}_4$  and  $\text{CuCr}_2\text{Se}_4$ ”, *Solid State Communications* **2** (1964), no. 2, 55–56.
- [81] Blasse, G., “Ferromagnetism and ferrimagnetism of oxygen spinels containing tetravalent manganese”, *Journal of Physics and Chemistry of Solids* **27** (1966), no. 2, 383–389.
- [82] Silwal, P., et al., “Metal insulator transition with ferrimagnetic order in epitaxial thin films of spinel  $\text{NiCo}_2\text{O}_4$ ”, *Applied Physics Letters* **100** (2012), no. 3, 032102.
- [83] Emin, D., “Small polarons”, *Physics today* **35** (1982), 34–40.
- [84] Austin, I. and N. F. Mott, “Polarons in crystalline and non-crystalline materials”, *Advances in Physics* **18** (1969), no. 71, 41–102.
- [85] Kittel, C., *Introduction to solid state physics*, vol. 7, John Wiley Sons, New York, 1996.
- [86] Ashcroft, N. and N. Mermin, *Solid state physics*, Saunders College, 1976.
- [87] Khmelnitskii, D., “Quantum hall effect and additional oscillations of conductivity in weak magnetic fields”, *Physics Letters A* **106** (1984), no. 4, 182–183.



- [88] Abrahams, E., et al., “Quasiparticle lifetime in disordered two-dimensional metals”, *Phys. Rev. B* **24** (1981), 6783–6789.
- [89] Altshuler, B. and A. Aronov, “Electron density of states and energy relaxation time in magnetic field”, *Solid State Communications* **38** (1981), no. 1, 11–15.
- [90] Bergmann, G., “Weak localization in thin films: a time-of-flight experiment with conduction electrons”, *Physics Reports* **107** (1984), no. 1, 1–58.
- [91] Stone, A. D., “Magnetoresistance fluctuations in mesoscopic wires and rings”, *Phys. Rev. Lett.* **54** (1985), 2692–2695.
- [92] Lee, P. A. and T. Ramakrishnan, “Disordered electronic systems”, *Reviews of Modern Physics* **57** (1985), no. 2, 287.
- [93] Kondo, J., “Resistance minimum in dilute magnetic alloys”, *Progress of theoretical physics* **32** (1964), no. 1, 37–49.
- [94] Hewson, A. C., *The kondo problem to heavy fermions*, no. 2, Cambridge university press, 1997.
- [95] Kondo, J., “sd scattering at low temperatures”, *Progress of Theoretical Physics* **34** (1965), no. 2, 204–209.
- [96] Tanner, D. B., “Optical effects in solids”.
- [97] Christen, H. M. and G. Eres, “Recent advances in pulsed-laser deposition of complex oxides”, *Journal of Physics: Condensed Matter* **20** (2008), no. 26, 264005.
- [98] Dijkkamp, D., et al., “Preparation of y-ba-cu oxide superconductor thin films using pulsed laser evaporation from high  $t_c$  bulk material”, *Applied Physics Letters* **51** (1987), no. 8, 619–621.
- [99] Stern, I., et al., “Role of spinel substrate in the morphology of bifeo<sub>3</sub>-cofe<sub>2</sub> o<sub>4</sub> epitaxial nanocomposite films”, *Applied Physics Letters* **99** (2011), no. 8, 082908–082908.
- [100] Martin, L., Y.-H. Chu, and R. Ramesh, “Advances in the growth and characterization of magnetic, ferroelectric, and multiferroic oxide thin films”, *Materials Science and Engineering: R: Reports* **68** (2010), no. 4, 89–133.
- [101] Biegalski, M., et al., “Critical thickness of high structural quality srtio<sub>3</sub> films grown on orthorhombic (101) dysco<sub>3</sub>”, *Journal of Applied Physics* **104** (2008), no. 11, 114109.
- [102] King, W. and A. Tseung, “The reduction of oxygen on nickel-cobalt oxidesii: Correlation between crystal structure and activity of co<sub>2</sub>nio<sub>4</sub> and related oxides”, *Electrochimica Acta* **19** (1974), no. 8, 493–498.

- [103] Kusters, R., et al., “Magnetoresistance measurements on the magnetic semiconductor  $\text{Nd}_{0.5}\text{Pb}_{0.5}\text{MnO}_3$ ”, *Physica B: Condensed Matter* **155** (1989), no. 1, 362–365.
- [104] Zhu, J. and Q. Gao, “Mesoporous  $\text{MCO}_2\text{O}_4$  ( $\text{M} = \text{Cu}, \text{Mn}$  and  $\text{Ni}$ ) spinels: Structural replication, characterization and catalytic application in  $\text{CO}$  oxidation”, *Microporous and Mesoporous Materials* **124** (2009), no. 1, 144–152.
- [105] Venzke, S., et al., “Epitaxial growth and magnetic behavior of  $\text{NiFe}_2\text{O}_4$  thin films”, *Journal of materials research* **11** (1996), no. 05, 1187–1198.
- [106] Lüders, U., et al., “Enhanced magnetic moment and conductive behavior in  $\text{NiFe}_2\text{O}_4$  spinel ultrathin films”, *Phys. Rev. B* **71** (2005), 134419.
- [107] Moyer, J., et al., “Epitaxial strain-induced changes in the cation distribution and resistivity of  $\text{Fe}$ -doped  $\text{CoFe}_2\text{O}_4$ ”, *Applied Physics Letters* **101** (2012), no. 2, 021907.
- [108] Moyer, J., et al., “Enhanced magnetic moment in ultrathin  $\text{Fe}$ -doped  $\text{CoFe}_2\text{O}_4$  films”, *Physical Review B* **86** (2012), no. 17, 174404.
- [109] Silwal, P., et al., “Effect of growth temperature on the terahertz-frequency conductivity of the epitaxial transparent conducting spinel  $\text{NiCo}_2\text{O}_4$  films”, *AIP Advances* **3** (2013), no. 9, 092116.
- [110] Premkumar, P., et al., “Preparation of doped spinel cobalt oxide thin films and evaluation of their thermal stability”, *Chemical Vapor Deposition* **13** (2007), no. 2-3, 118–122.
- [111] Iliev, M., et al., “Raman studies of cation distribution and thermal stability of epitaxial spinel  $\text{NiCo}_2\text{O}_4$  films”, *Journal of Applied Physics* **114** (2013), no. 3, 033514.
- [112] Sarachik, M. P., E. Corenzwit, and L. D. Longinotti, “Resistivity of  $\text{Mo-Nb}$  and  $\text{Mo-Re}$  alloys containing 1A1041–A1045.
- [113] Kuo, T. and K. Wang, “Electrical resistivity of ultrathin, epitaxial  $\text{CoGa}$  on  $\text{GaAs}$ ”, *Applied physics letters* **59** (1991), no. 26, 3399–3401.
- [114] Rozenberg, E. and M. Auslender, “Comment on ‘low-temperature transport properties of non-stoichiometric  $\text{La}_{0.95-x}\text{Sr}_x\text{MnO}_3$ ’”, *Journal of Physics: Condensed Matter* **14** (2002), no. 37, 8755.
- [115] Tiwari, A. and K. Rajeev, “Low-temperature electrical transport in  $\text{La}_{0.7}\text{A}_{0.3}\text{MnO}_3$ , ( $\text{A} = \text{Ca}, \text{Sr}, \text{Ba}$ )”, *Solid state communications* **111** (1999), no. 1, 33–37.
- [116] Jia, R., et al., “Effects of ferroelectric-poling-induced strain on the quantum correction to low-temperature resistivity of manganite thin films”, *Physical Review B* **82** (2010), no. 10, 104418.

- [117] Kumar, D., et al., “Low-temperature resistivity minima in colossal magnetoresistive  $\text{La}_{0.7}\text{Ca}_{0.3}\text{MnO}_3$  thin films”, *Physical Review B* **65** (2002), no. 9, 094407.
- [118] Ziese, M., et al., “Thickness dependent magnetic and magnetotransport properties of strain-relaxed  $\text{La}_{0.7}\text{Ca}_{0.3}\text{MnO}_3$  films”, *Journal of applied physics* **91** (2002), no. 12, 9930–9936.
- [119] Maritato, L., et al., “Low-temperature resistivity of  $\text{La}_{0.7}\text{Sr}_{0.3}\text{MnO}_3$  ultra thin films: Role of quantum interference effects”, *Physical Review B* **73** (2006), no. 9, 094456.
- [120] Kim, D., et al., “Electrical properties of  $\text{SrVO}_3/\text{SrTiO}_3$  superlattices grown by laser molecular beam epitaxy”, *Solid state communications* **114** (2000), no. 9, 473–476.
- [121] Zhang, R. and R. F. Willis, “Thickness-dependent curie temperatures of ultrathin magnetic films: effect of the range of spin-spin interactions”, *Physical review letters* **86** (2001), no. 12, 2665.
- [122] Borges, R., et al., “Magnetic and electric dead layers in  $(\text{La}_{0.7}\text{Sr}_{0.3})\text{MnO}_3$  thin films”, *Journal of Applied Physics* **89** (2001), no. 7, 3868–3873.
- [123] Huijben, M., et al., “Critical thickness and orbital ordering in ultrathin  $\text{La}_{0.7}\text{Sr}_{0.3}\text{MnO}_3$  films”, *Physical Review B* **78** (2008), no. 9, 094413.
- [124] Tonouchi, M., “Cutting-edge terahertz technology”, *Nature photonics* **1** (2007), no. 2, 97–105.
- [125] Schmuttenmaer, C. A., “Exploring dynamics in the far-infrared with terahertz spectroscopy”, *Chemical reviews* **104** (2004), no. 4, 1759–1780.
- [126] Ferguson, B. and X.-C. Zhang, “Materials for terahertz science and technology”, *Nature materials* **1** (2002), no. 1, 26–33.
- [127] <http://lts.fzu.cz/en/intro.htm>, “Spectrum of electromagnetic radiation”.
- [128] Kitaeva, G. K., “Terahertz generation by means of optical lasers”, *Laser Physics Letters* **5** (2008), no. 8, 559.
- [129] Kübler, C., R. Huber, and A. Leitenstorfer, “Ultrabroadband terahertz pulses: generation and field-resolved detection”, *Semiconductor science and technology* **20** (2005), no. 7, S128.
- [130] Boyd, R. W., *Nonlinear optics*, Academic press, 2003.
- [131] Bass, M., et al., “Optical rectification”, *Physical Review Letters* **9** (1962), no. 11, 446.
- [132] Yajima, T. and N. Takeuchi, “Far-infrared difference-frequency generation by picosecond laser pulses”, *Japanese Journal of Applied Physics* **9** (1970), no. 11, 1361–1371.

- [133] Morris, J. and Y. Shen, “Far-infrared generation by picosecond pulses in electro-optical materials”, *Optics Communications* **3** (1971), no. 2, 81–84.
- [134] Yang, K. H., P. L. Richards, and Y. R. Shen, “Generation of farinfrared radiation by picosecond light pulses in  $\text{linbo}_3$ ”, *Applied Physics Letters* **19** (1971), no. 9, 320–323.
- [135] Auston, D. H., A. M. Glass, and P. LeFur, “Tunable farinfrared generation by difference frequency mixing of dye lasers in reduced (black) lithium niobate”, *Applied Physics Letters* **23** (1973), no. 1, 47–48.
- [136] Rice, A., et al., “Terahertz optical rectification from  $110^\circ$  zinc-blende crystals”, *Applied physics letters* **64** (1994), no. 11, 1324–1326.
- [137] Zhang, X.-C., et al., “Resonant nonlinear susceptibility near the gas band gap”, *Physical review letters* **69** (1992), no. 15, 2303.
- [138] Schneider, A., I. Biaggio, and P. Günter, “Optimized generation of thz pulses via optical rectification in the organic salt dast”, *Optics communications* **224** (2003), no. 4, 337–341.
- [139] Nahata, A., et al., “Generation of terahertz radiation from a poled polymer”, *Applied physics letters* **67** (1995), no. 10, 1358–1360.
- [140] Namba, S., “Electro-optical effect of zincblende”, *JOSA* **51** (1961), no. 1, 76–79.
- [141] Shen, Y., “Recent advances in nonlinear optics”, *Reviews of Modern Physics* **48** (1976), no. 1, 1.
- [142] Auston, D. H. and K. Cheung, “Coherent time-domain far-infrared spectroscopy”, *JOSA B* **2** (1985), no. 4, 606–612.
- [143] Ma, X. and X.-C. Zhang, “Determination of ratios between nonlinear-optical coefficients by using subpicosecond optical rectification”, *JOSA B* **10** (1993), no. 7, 1175–1179.
- [144] Wu, Q. and X.-C. Zhang, “Free-space electro-optic sampling of terahertz beams”, *Applied Physics Letters* **67** (1995), no. 24, 3523–3525.
- [145] de Dood, M. J., “Second-harmonic generation”, *Huygens Laboratorium 909a* (2006).
- [146] <http://www.ece.rice.edu/~daniel/569/files/lecture8>, “Nonlinear optics i”.
- [147] Shen, Y.-R., “The principles of nonlinear optics”, *New York, Wiley-Interscience, 1984, 575 p.* **1** (1984).

- [148] A. Corchia, D. D. A. E. H. L. M. S. . M. P., C. M. C., “Crystallographic orientation dependence of bulk optical rectification”, *Journal of Modern Optics* **47** (2000), no. 11, 1837–1845.
- [149] Nahata, A., A. S. Weling, and T. F. Heinz, “A wideband coherent terahertz spectroscopy system using optical rectification and electro-optic sampling”, *Applied Physics Letters* **69** (1996), no. 16, 2321–2323.
- [150] Reimann, K., “Table-top sources of ultrashort thz pulses”, *Reports on Progress in Physics* **70** (2007), no. 10, 1597.
- [151] Vidal, S., et al., “Optimized terahertz generation via optical rectification in znte crystals”, *JOSA B* **31** (2014), no. 1, 149–153.
- [152] Löffler, T., et al., “Large-area electro-optic znte terahertz emitters”, *Optics express* **13** (2005), no. 14, 5353–5362.
- [153] Vidal, S., et al., “Impact of dispersion, free carriers, and two-photon absorption on the generation of intense terahertz pulses in znte crystals”, *Applied Physics Letters* **98** (2011), no. 19, 191103.
- [154] Harrel, S. M., et al., “Influence of free-carrier absorption on terahertz generation from znte (110)”, *Journal of Applied Physics* **107** (2010), no. 3, 033526.
- [155] Zhao, Z., S. Hameau, and J. Tignon, “Thz generation by optical rectification and competition with other nonlinear processes”, *PHYSICS OF SEMICONDUCTORS: 28th International Conference on the Physics of Semiconductors-ICPS 2006*, vol. 893, AIP Publishing, 2007, pp. 503–504.
- [156] Ku, S., et al., “Saturation of the free carrier absorption in znte crystals”, *Optics express* **21** (2013), no. 12, 13930–13937.
- [157] Wu, Q. and X.-C. Zhang, “7 terahertz broadband gap electro-optic sensor”, *Applied physics letters* **70** (1997), no. 14, 1784–1786.
- [158] Casalbuoni, S., et al., “Numerical studies on the electro-optic detection of femtosecond electron bunches”, *Physical Review Special Topics-Accelerators and Beams* **11** (2008), no. 7, 072802.
- [159] Hirori, H., et al., “Single-cycle terahertz pulses with amplitudes exceeding 1 mv/cm generated by optical rectification in linbo<sub>3</sub>”, *Applied Physics Letters* **98** (2011), no. 9, 091106–091106.
- [160] <http://thz.yale.edu/technique/tilted-wavefront-thz-generation>, “Tilted wavefront thz generation”.

- [161] Hebling, J., et al., “High-power thz generation, thz nonlinear optics, and thz nonlinear spectroscopy”, *Selected Topics in Quantum Electronics, IEEE Journal of* **14** (2008), no. 2, 345–353.
- [162] Hebling, J., et al., “Generation of high-power terahertz pulses by tilted-pulse-front excitation and their application possibilities”, *JOSA B* **25** (2008), no. 7, B6–B19.
- [163] Auston, D., K. Cheung, and P. Smith, “Picosecond photoconducting hertzian dipoles”, *Applied Physics Letters* **45** (1984), no. 3, 284–286.
- [164] Auston, D. H. and M. C. Nuss, “Electrooptical generation and detection of femtosecond electrical transients”, *Quantum Electronics, IEEE Journal of* **24** (1988), no. 2, 184–197.
- [165] Smith, P. R., D. H. Auston, and M. C. Nuss, “Subpicosecond photoconducting dipole antennas”, *Quantum Electronics, IEEE Journal of* **24** (1988), no. 2, 255–260.
- [166] Darrow, J., et al., “Subpicosecond electromagnetic pulses from large-aperture photoconducting antennas”, *Optics letters* **15** (1990), no. 6, 323–325.
- [167] Mourou, G., C. V. Stancampiano, and D. Blumenthal, “Picosecond microwave pulse generation”, *Applied Physics Letters* **38** (1981), no. 6, 470–472.
- [168] Xu, L., et al., “Terahertz radiation from large aperture si p-i-n diodes”, *Applied physics letters* **59** (1991), no. 26, 3357–3359.
- [169] You, D., et al., “Generation of high-power sub-single-cycle 500-fs electromagnetic pulses”, *Optics letters* **18** (1993), no. 4, 290–292.
- [170] Hu, B., et al., “Optically steerable photoconducting antennas”, *Applied physics letters* **56** (1990), no. 10, 886–888.
- [171] Greene, B. I., et al., “Far-infrared light generation at semiconductor surfaces and its spectroscopic applications”, *Quantum Electronics, IEEE Journal of* **28** (1992), no. 10, 2302–2312.
- [172] Taylor, A., P. Benicewicz, and S. Young, “Modeling of femtosecond electromagnetic pulses from large-aperture photoconductors”, *Optics letters* **18** (1993), no. 16, 1340–1342.
- [173] Jepsen, P. U., et al., “Detection of thz pulses by phase retardation in lithium tantalate”, *Phys. Rev. E* **53** (1996), no. 4, 3052–3054.
- [174] Froberg, N., et al., “500 ghz electrically steerable photoconducting antenna array”, *Applied physics letters* **58** (1991), no. 5, 446–448.

- [175] Benicewicz, P. and A. Taylor, “Scaling of terahertz radiation from large-aperture biased in photoconductors”, *Optics letters* **18** (1993), no. 16, 1332–1334.
- [176] Kuznetsov, A. and C. Stanton, “Ultrafast optical generation of carriers in a dc electric field: Transient localization and photocurrent”, *Physical Review B* **48** (1993), no. 15, 10828.
- [177] Siders, C., et al., “Generation and characterization of terahertz pulse trains from biased, large-aperture photoconductors”, *Optics letters* **24** (1999), no. 4, 241–243.
- [178] <http://thz.yale.edu/technique/thz-sources-and-detectors>, “Thz sources and detectors”.
- [179] Tani, M., et al., “Novel terahertz photoconductive antennas”, *International journal of infrared and millimeter waves* **27** (2006), no. 4, 531–546.
- [180] Darrow, J. T., et al., “Saturation properties of large-aperture photoconducting antennas”, *Quantum Electronics, IEEE Journal of* **28** (1992), no. 6, 1607–1616.
- [181] Lee, Y.-S., *Principles of terahertz science and technology: Proceedings of the international conference, held in mainz, germany, june 5-9, 1979*, vol. 170, Springer, 2009.
- [182] Mickan, S. P. and X.-C. Zhang, “T-ray sensing and imaging”, *International Journal of High Speed Electronics and Systems* **13** (2003), no. 02, 601–676.
- [183] Nahata, A., A. S. Weling, and T. F. Heinz, “A wideband coherent terahertz spectroscopy system using optical rectification and electro-optic sampling”, *Applied Physics Letters* **69** (1996), no. 16, 2321–2323.
- [184] Nahata, A., et al., “Coherent detection of freely propagating terahertz radiation by electro-optic sampling”, *Applied physics letters* **68** (1996), no. 2, 150–152.
- [185] Teich, M. C. and B. Saleh, “Fundamentals of photonics”, *Canada, Wiley Interscience* (1991), 3.
- [186] Yariv, A. and P. Yeh, *Photonics: Optical electronics in modern communications (the oxford series in electrical and computer engineering)*, Oxford University Press, Inc., 2006.
- [187] Zhang, X.-C. and J. Xu, *Introduction to thz wave photonics*, Springer, 2010.
- [188] Fattinger, C. and D. Grischkowsky, “Terahertz beams”, *Applied Physics Letters* **54** (1989), no. 6, 490–492.
- [189] Kono, S., M. Tani, and K. Sakai, “Ultrabroadband photoconductive detection: Comparison with free-space electro-optic sampling”, *Applied Physics Letters* **79** (2001), no. 7, 898–900.

- [190] Kono, S., et al., “Detection of up to 20 thz with a low-temperature-grown gaas photoconductive antenna gated with 15 fs light pulses”, *Applied Physics Letters* **77** (2000), no. 25, 4104–4106.
- [191] Greenland, P., “Terahertz physics”, *Contemporary Physics* (2013), no. ahead-of-print, 1.
- [192] <http://dl.zthz.com/eBook/zomega>, “The terahertz wave ebook”.
- [193] <http://bernath.uwaterloo.ca/media/Fourier> “Fourier transform techniques”.
- [194] Lloyd-Hughes, J. and T.-I. Jeon, “A review of the terahertz conductivity of bulk and nano-materials”, *Journal of Infrared, Millimeter, and Terahertz Waves* **33** (2012), no. 9, 871–925.
- [195] Averitt, R. and A. Taylor, “Ultrafast optical and far-infrared quasiparticle dynamics in correlated electron materials”, *Journal of Physics: Condensed Matter* **14** (2002), no. 50, R1357.
- [196] Duvillaret, L., F. Garet, and J.-L. Coutaz, “A reliable method for extraction of material parameters in terahertz time-domain spectroscopy”, *Selected Topics in Quantum Electronics, IEEE Journal of* **2** (1996), no. 3, 739–746.
- [197] Okuda, T., T. Kimura, and Y. Tokura, “Low-temperature transport properties in a bilayered manganite  $\text{La}_{1.3}\text{Sr}_{1.7}\text{Mn}_2\text{O}_7$ ”, *Physical Review B* **60** (1999), no. 5, 3370.
- [198] Zhang, C., et al., “Low-temperature electrical transport in bilayer manganite  $\text{La}_{1.2}\text{Sr}_{1.8}\text{Mn}_2\text{O}_7$ ”, *Physical Review B* **65** (2002), no. 13, 134439.
- [199] Ziese, M., “Searching for quantum interference effects in  $\text{La}_{0.7}\text{Ca}_{0.3}\text{MnO}_3$  films on  $\text{SrTiO}_3$ ”, *Physical Review B* **68** (2003), no. 13, 132411.
- [200] Basov, D., B. Dabrowski, and T. Timusk, “Infrared probe of transition from superconductor to nonmetal in  $\text{YBa}_2(\text{Cu}_{1-x}\text{Zn}_x)_4\text{O}_8$ ”, *Physical review letters* **81** (1998), no. 10, 2132.
- [201] Silwal, P., et al., “Thickness dependent structural, magnetic, and electronic properties of the epitaxial films of transparent conducting oxide  $\text{NiCo}_2\text{O}_4$ ”, *Journal of Applied Physics* **114** (2013), no. 10, 103704.
- [202] Zou, X., et al., “Terahertz conductivity of twisted bilayer graphene”, *Physical review letters* **110** (2013), no. 6, 067401.
- [203] Owings, R. R., et al., “Process enhanced polaron conductivity of infrared transparent nickel–cobalt oxide”, *Thin Solid Films* **483** (2005), no. 1, 175–184.
- [204] Emin, D., “Optical properties of large and small polarons and bipolarons”, *Physical Review B* **48** (1993), no. 18, 13691.



- [205] Salamon, M. B. and M. Jaime, “The physics of manganites: Structure and transport”, *Reviews of Modern Physics* **73** (2001), no. 3, 583.
- [206] Kim, K., J. Jung, and T. Noh, “Polaron absorption in a perovskite manganite  $\text{La}_{0.7}\text{Ca}_{0.3}\text{MnO}_3$ ”, *Physical review letters* **81** (1998), no. 7, 1517.
- [207] Quijada, M., et al., “Optical conductivity of manganites: crossover from jahn-teller small polaron to coherent transport in the ferromagnetic state”, *Phys. Rev. B* **58** (1998), 16093–16102.
- [208] Basov, D. N., et al., “Electrodynamics of correlated electron materials”, *Reviews of Modern Physics* **83** (2011), no. 2, 471.
- [209] Cheng, C.-S., et al., “Electrical conductivity of  $\text{Co}_3\text{O}_4$  films prepared by chemical vapour deposition”, *Materials chemistry and physics* **53** (1998), no. 3, 225–230.
- [210] Ihle, D. and B. Lorenz, “Small-polaron conduction and short-range order in  $\text{Fe}_3\text{O}_4$ ”, *Journal of Physics C: Solid State Physics* **19** (1986), no. 26, 5239.

# Publications

1. "Metal insulator transition with ferrimagnetic order in epitaxial thin films of spinel  $\text{NiCo}_2\text{O}_4$ "

**P. Silwal**, L. Miao, I. Stern, X. Zhou, J. Hu, and D. H. Kim, Appl. Phys. Lett. 100, 032102 (2012).

2. "Thickness dependent structural, magnetic, and electronic properties of the epitaxial films of transparent conducting oxide  $\text{NiCo}_2\text{O}_4$ "

**P. Silwal**, L. Miao, J. Hu, L. Spinu, D. H. Kim, and D. Talbayev, J. Appl. Phys. 114, 103704 (2013).

3. "Effect of growth temperature on the terahertz-frequency conductivity of epitaxial transparent conducting spinel  $\text{NiCo}_2\text{O}_4$  films"

**P. Silwal**, Chan La-o-vorakiat, Elbert E. M. Chia, D. H. Kim, and D. Talbayev, AIP Advances. Vol. 3, pp 092116 (2013).

4. "Raman studies of cation distribution and thermal stability of epitaxial spinel  $\text{NiCo}_2\text{O}_4$  films"

M. N. Iliev, **P. Silwal**, B. Loukya, R. Datta, D. H. Kim, N. D. Todorov, N. Pachauri, and A. Gupta, J. Appl. Phys. Vol. 114, pp 033514 (2013).

5. "Epitaxial strain effect on transport properties in  $\text{Ca}_{2-x}\text{Sr}_x\text{RuO}_4$  thin films"

L. Miao, W. Zhang, **P. Silwal**, X. Zhou, I. Stern, T. J. Liu, J. Peng, J. Hu, D. H. Kim and Z. Q. Mao, Phys. Rev. B 88, 115102 (2013).

6. "Modulations in structural and ferroelectric properties due to tensile strain in  $\text{BiFeO}_3$  films on  $\text{MgAl}_2\text{O}_4$  substrates induced by thermal-expansion"

X. Zhou, L. Miao, I. Stern, **P. Silwal**, and D. H. Kim, Mater. Sci. Eng. B, 177, 685 (2012).

7. "Itinerant ferromagnetism and geometrically suppressed metal-insulator transition in epitaxial thin film of  $\text{Ca}_2\text{RuO}_4$  "

L. Miao, **P. Silwal**, X. Zhou, I. Stern, J. Peng, W. Zhang, L. Spinu, Z. Q. Mao and D. H. Kim, Appl. Phys. Lett. 100, 052401 (2012).

8. "Coherent in-plane tensile strain in perovskite  $\text{Ba}_{0.8}\text{Sr}_{0.2}\text{TiO}_3$  films on spinel  $\text{MgAl}_2\text{O}_4$  substrates" X. Zhou, I. Stern, **P. Silwal**, L. Miao, D. H. Kim, Appl. Phys. Lett. 100, 032902 (2012).

9. "Role of spinel substrate in the morphology of  $\text{BiFeO}_3$ - $\text{CoFe}_2\text{O}_4$  epitaxial nanocomposite films"

I. Stern, J. He, X. Zhou, **P. Silwal**, L. Miao, J. M. Vargas, L. Spinu, and D. H. Kim, Appl. Phys. Lett. 99, 082908 (2011).